NORTHWESTERN UNIVERSITY

Development and Characterization of PEG-*b*-PPS Nanocarriers for

Magnetic Resonance Imaging and Drug Delivery

A DISSERTATION

SUBMITTED TO THE GRADUATE SCHOOL

IN PARTIAL FULFILLMENT OF THE REQUIREMENTS

for the degree

DOCTOR OF PHILOSOPHY

Field of Biomedical Engineering

By

Mallika Modak

EVANSTON, ILLINOIS

September 2021

ABSTRACT

Development and Characterization of PEG-*b*-PPS Nanocarriers for

Magnetic Resonance Imaging and Drug Delivery

Like many diseases, atherosclerotic cardiovascular disease is driven by the activity of inflammatory cells. Using molecular imaging to target and analyze populations of inflammatory cells is one promising strategy to non-invasively assess atherosclerosis progression. However, current molecular imaging contrast agents are not suited for such targeted imaging applications. Nanomaterial-based strategies have great promise for targeted delivery of contrast agents due to their ability to accumulate within target cells, specifically in immune cell subsets. In particular, the diblock co-polymer poly(ethylene glycol)-*block*-poly(propylene sulfide) (PEG-*b*-PPS) is a versatile nanomaterial system capable of self-assembling into nanocarriers of different shapes and has great utility for the targeted delivery of encapsulated cargo to immune cells. This work describes the development of PEG-*b*-PPS nanocarriers for the delivery of magnetic resonance imaging (MRI) contrast agents in the context of targeted imaging of atherosclerotic cardiovascular disease. First, I have demonstrated the utility of multiple PEG-*b*-PPS nanocarrier morphologies for encapsulation and controlled delivery of metal ferrite magnetic nanostructures (MNS), which are nanoscale MRI contrast agents for T2-weighted imaging. I focused on developing MNS-encapsulated bicontinuous nanospheres (MBCNs), and characterizing their MRI contrast enhancement, ability to deliver therapeutic payloads *in vitro* and *in vivo*, and response to oxidative stimuli. Notably, I found that MBCNs undergo a transition in morphology into MNS-loaded micelles under oxidative conditions, which makes these nanocarriers promising for sustained delivery applications. Second, I engineered PEG-*b*-PPS polymersomes (PS) to simultaneously (i)

deliver Gd-DOTA for T1 MRI contrast enhancement and (ii) display the P-D2 peptide sequence for targeting dendritic cells (DCs) in atherosclerotic plaques. My work demonstrated that DOTA-displaying PS (DOTA-PS) are promising nanocarriers for T1 MRI, demonstrating effective T1 enhancement *in vitro*. I further characterized the use of the P-D2 peptide for mediating effective nanocarrier uptake in DCs, both *in vitro* and *in vivo* in a mouse model of heart disease. Overall, my work expands on the current applications of PEG-*b*-PPS nanocarriers, and demonstrates that these nanocarriers can be engineered for diagnostic applications and molecular imaging via stable encapsulation of MRI contrast agents.

ACKNOWLEDGEMENTS

There are several people who I have to thank for helping me, teaching me, and guiding me to get to this point. To start, I would like to acknowledge and thank my mom and dad, <u>Ashwini and Vivek Modak</u>, for their unwavering support of me and my goals. You both raised me to work hard and keep persevering, and I hope to keep doing that and making you proud every day. Aai, I owe everything to you and all of your hard work. Seeing how much you love your job sparked my interest in healthcare and set me on the path I am on today. Baba, thank you for always encouraging me to strive for the very best and for teaching me the importance of paying attention to detail.

I next want to thank my fiancé, <u>Mit Patel</u>, who has supported me tremendously through the past several years. As we both pursue our goals in medical/graduate school, you have always been there to support me, reassure me, and care for me through all of the ups and downs of science.

I'd also like to acknowledge my friends from medical school, college, and back home, all of whom helped me keep things in perspective and enjoy life outside of the lab. To a few friends in particular: <u>Divya</u> – thank you for paving the way through the PhD. Your advice and seeing you navigate graduate school has been so helpful and inspiring. <u>Mahati</u> – I am so glad I got to be roommates with you. Your friendship helped me stay sane and be productive at such an overwhelming time at the start of the COVID-19 pandemic. I could not have made it through the work-from-home period without our baking adventures, our home workouts, and TV nights.

Thank you to everyone in the Scott Lab who I have had the fortune to work with and get to know over the past 4 years. Thank you for being the most supportive and fun group of people. <u>Sophia</u> – my lab buddy, "treat yourself" friend, and other half in the lab: your friendship and support means so much to me. Thanks for always being willing to get coffee, or go for a walk, and

for all of the work from home days, baking nights, and Netflix nights. I am so lucky I get to navigate grad school and return to medical school with you. I'll always be thankful that working in this lab brought us together. Sharan – Your mentorship and teaching really helped me hit the ground running in lab, and your guidance especially helped to drive my projects forward, for which I am extremely grateful. Thank you! Molly – Thanks for always being right there (literally) to share ideas with, talk about The Office, and get free food with. I'm glad to have your support and friendship as we all return to medical school together. Also, long live the snack drawer! Jacqueline and Mike – you are both the most hardworking graduate students I have ever met. Jacqueline – you have always inspired me to work harder, to take ownership of my projects from day one, and to never give up. Mike – thanks for always being willing to discuss data and helping me to design experiments more effectively. Also, thanks for introducing me to Quest protein chips. Bryan and Sun-Young – thanks for your collaboration and help with planning and executing my animal studies and dendritic cell studies. This work would not have been possible without you. To everyone else I had the fortune to work with in the lab: Sean, Nick, Sijia, Fanfan, Debora, Trevor, Chamille, Jen, Clayton – I would not have gotten to where I am without all of your help, discussions, and support throughout the years.

Next, I would like to thank the following people from the Northwestern research community for their collaboration and contributions to my work: Vikas Nandwana – thanks for providing all of the MNS particles for this work, the helpful discussions, and the access to the thermal activation instrument. Without your assistance, this work truly would have been impossible. Alex Waters – Thank you for the numerous MRI studies on the Evanston campus. I learned so much about MRI through our discussions, which sparked my current interest in

radiology as a career. <u>Becky Sponenburg</u> and <u>Keith Macrenaris</u> – Thank you for all of your help with ICP-MS, discussions about experimental design and MRI, and troubleshooting. Coming down to QBIC was always a treat, and I'm excited to see all of the work that comes out of the core facility in the future. Finally, thanks to the <u>Meade Lab</u> for use of the relaxometer and Guava cell counter and for all of the discussions about MRI.

I would also like to thank the <u>Northwestern MSTP administration</u>. While the names and faces in the office have changed over time, the encouragement and support has stayed the same.

I am also grateful to all of my teachers and professors from elementary school, middle school, high school, college, and now graduate school, who helped guide me to where I am today. Thank you also to my research mentors throughout the years who taught me the joys of research.

Thank you to my thesis committee: Professors <u>Susan E. Clare</u>, <u>Vinayak P. Dravid</u>, and <u>Nathan Gianneschi</u> for your feedback and insights at my annual committee meetings, which were crucial for the development of my projects.

Finally, I would like to thank my thesis advisor, <u>Professor Evan Scott</u>. Thank you for providing me with such a positive graduate school experience, and for being so patient, supportive, and optimistic about my work. Even after discussing disappointing or confusing sets of data, I would always leave our meetings with hope and excitement for the next steps and follow up experiments. I also appreciate the balance you struck between guiding my studies and giving me the freedom to explore different ideas. Looking back, I realize that this evolved over time depending on what I needed at that point in my training. I owe the growth of my confidence and curiosity as a scientist to your mentorship. Thank you!

LIST OF ABBREVIATIONS

AC	Alternating Current
ALT	Alanine Aminotransferase
ApoB	Apolipoprotein B
AR	Acute Rejection
BBB	Blood Brain Barrier
BCNs	Bicontinuous Nanospheres
BMSC	Bone Marrow Mesenchymal Stem Cells
BPCAs	Blood Pool Contrast Agents
CIJ	Confined Impingement Jet
CNS	Central Nervous System
CPMG	Carr-Purcell Meiboom-Gill
CPT	Camptothecin
Cryo-TEM	Cryogenic Transmission Electron Microscopy
CS	Co-Solvent Evaporation
CT	Computed Tomography

CuS	Copper Sulfide
CVD	Cardiovascular Disease
DCM	Dichloromethane
DCs	Dendritic Cells
DE	Double Emulsion
DH	Direct Hydration
DIC	*N,N'*-Diisopropylcarbodiimide
DiD	1,1'-Dioctadecyl-3,3,3',3'-Tetramethylindodicarbocyanine, 4-Chlorobenzenesulfonate)
DIPEA	*N, N*-Diisopropylethyleamine
DiR	1,1′-Dioctadecyl-3,3,3′,3′-Tetramethylindotricarbocyanine Iodide
DLS	Dynamic Light Scattering
DMF	Dimethylformamide
DMSO	Dimethyl Sulfoxide
DNA	Deoxyribonucleic Acid
DOTA	Dodecane Tetraacetic Acid
DOX	Doxorubicin
DS	Dextran Sulfate

DTPA   Diethylenetriamine Pentaacetate

ECF   Extracellular Fluid

EDS   Energy-Dispersive X-Ray Spectroscopy

FBS   Fetal Bovine Serum

FDG   Fluorodeoxyglucose

FITC-BSA   Fluorescein Isothiocyanate-Tagged Bovine Serum Albumin

FMOC   Fluorenylmethoxycarbonyl

FMs   Filomicelles

FNP   Flash Nanoprecipitation

f_{PEG} PEG Weight Fraction

GBCAs   Gadolinium-Based Contrast Agents

Gd-EOB-DTPA   Gadoxetate Disodium

HAADF   High Angle Annular Dark Field

HBTU   2-(1H-Benzotriazol-1-yl)-1,1,3,3-Tetramethyluronium
             Hexafluorophosphate

HDL   High-Density Lipoproteins

HPLC   High Performance Liquid Chromatography

HSP   Heat Shock Protein

ICG	Indocyanine Green
ICP-MS	Inductively Coupled Plasma Mass Spectrometry
IV	Intravenous
IVIS	Intravital Imaging System
LC/MS	Liquid Chromatography/Mass Spectrometry
LCST	Lower Critical Solution Temperature
LDL	Low-Density Lipoprotein
LIFU	Low Intensity Focused Ultrasound
MACE	Major Adverse Cardiovascular Event
MCs	Micelles
MHC	Major Histocompatibility Complex
MI	Myocardial Infarction
MLNC	Magnetic Lipid Nanocapsule
MNS	Magnetic Nanostructures
MPI	Magnetic Particle Imaging
MPS	Mononuclear Phagocyte System
MRI	Magnetic Resonance Imaging

Mtt	4-Methyltrityl
MTT	3-(4,5-Dimethylthiazol-2-yl)-2,5-diphenyl-tetrazolium Bromide
MWCO	Molecular Weight Cut-Off
NIR	Near-infrared
NIRF	Near-infrared Fluorescence
NMR	Nuclear Magnetic Resonance
NSET	Nanostructure Enhanced Targeting
OPN	Osteopontin
PAI	Photoacoustic Imaging
PBI	Perylene Bisimide
PBS	Phosphate Buffered Saline
PEG	Poly(Ethylene Glycol)
PEG-*b*-PPS	Poly(Ethylene Glycol)-*Block*-Poly(Propylene Sulfide)
PET	Positron Emission Tomography
PFCE-NPs	Perfluorocarbon Nanoparticles
PFH	Perfluorohexane
PFOB	Perfluorooctyl Bromide

PLA   Polylactic Acid

PLGA   Poly(Lactic-*co*-Glycolic Acid)

PSs   Polymersomes

PTX   Paclitaxel

PyBOP   (Benzotriazol-1-yloxy)tripyrrolidinophosphonium hexafluorophosphate

RF   Radiofrequency

ROS   Reactive Oxygen Species

SAR   Specific Absorption Rate

SAXS   Small Angle X-Ray Scattering

SD   Standard Deviation

SP   Semiconducting Polymers

SPIONs   Superparamagnetic Iron Oxide Nanoparticles

SR-A1   Class A1 Scavenger Receptors

STEM   Scanning Transmission Electron Microscopy

TA   Thermal Activation

TEM   Transmission Electron Microscopy

TFA   Trifluoroacetic Acid

TFH   Thin-Film Hydration

TFR1   Transferrin Receptor 1

THF   Tetrahydrofuran

TIS   Triisopropylsilane

TRPV1   Transient Receptor Potential Cation Channel Subfamily V Member 1

US   Ultrasound

VSMC   Vascular Smooth Muscle Cells

DEDICATION

I dedicate this thesis to my mother, Ashwini V. Modak.

Aai, everything I have done and will ever do is possible because of you.

TABLE OF CONTENTS

LIST OF FIGURES

LIST OF TABLES

CHAPTER 1

1. Introduction and Review of Literature

1.1. Dissertation Overview

1.1.1. Motivations and Objectives

Many diseases, particularly cardiovascular disease (CVD) such as atherosclerosis, are driven by the activity of inflammatory cells and physiological responses to inflammation. Targeting and analyzing these inflammatory cells via molecular imaging is one strategy for the non-invasive assessment of atherosclerotic plaque progression; however, current molecular imaging contrast agents are not suited for such targeted imaging applications. This work describes the development of poly(ethylene glycol)-*block*-poly(propylene sulfide) (PEG-*b*-PPS) nanocarriers for the delivery of magnetic resonance imaging (MRI) contrast agents in the context of targeted imaging of atherosclerotic cardiovascular disease.

1.1.2. Dissertation Outline

The following parts of **Chapter 1** will provide a comprehensive review of nanomaterials for molecular imaging, particularly for imaging cell-mediated processes in CVD. The utility of inflammatory cells as diagnostic markers of CVD will be discussed, along with strategies to target these cells via the use of nanocarriers. An overview of nanocarriers for targeted delivery applications will be given, focusing on PEG-*b*-PPS nanocarriers. **Chapter 2** will discuss my work on the use of PEG-*b*-PPS nanocarriers for encapsulating and delivering metal ferrite magnetic structures (MNS), which are nanoscale MRI contrast agents that are primarily used for T2-weighted imaging. **Chapter 3** surveys two specific therapeutic applications of these MNS-loaded nanocarriers: thermal activation and magnetic targeting. **Chapter 4** discusses my work on

engineering vesicular PEG-*b*-PPS polymersomes (PS) to provide T1 MRI contrast enhancement for targeted imaging of atherosclerotic disease. This chapter will also explore the immune cell profile in mouse aortas at multiple stages of heart disease. **Chapter 5** contains a summary of my work and an outline of future directions for the continued development of (i) MNS-encapsulated and (ii) DOTA-displaying PEG-*b*-PPS nanocarriers.

1.2. Review of Literature

1.2.1. Inflammatory Cells as Disease Markers in Cardiovascular Disease

CVD is the primary cause of global mortality, accounting for an estimated 17.8 million deaths annually worldwide[1]. CVD affects the heart and blood vessels, and the vast majority of associated pathologies are of atherosclerotic origin, driven by the buildup of plaques within vessel walls. If unaddressed, these pathologies can lead to a potentially fatal major adverse cardiovascular event (MACE) involving hypoxic injury to cardiac tissue[2]. Currently, there is a lack of non-invasive methods that are capable of determining the risk of MACEs *before* they occur, highlighting a need to develop non-invasive methods for determining this risk before occurrence.

Specific single cell-mediated processes have emerged as key targets for diagnostic and therapeutic strategies due to their critical roles in the pathology and treatment of CVD. One specific CVD that is driven by cell-mediated processes is atherosclerosis: a slow-progressing, inflammatory disease characterized by the build-up of blood vessel-occluding deposits in the intima, or inner layer, of arterial walls[3, 4]. These deposits contain a marked number of both innate and adaptive immune cells, including dendritic cells, macrophages, and T cells[5]. The chronic build-up of these deposits, or plaques, leads to stenosis and downstream tissue hypoxia. Given the gradual nature of plaque development in atherosclerosis, it is often not detected until severe

complications resulting from vessel occlusion occur. These complications, such as myocardial infarction (MI) and stroke, are among the most common causes of death worldwide[6].

The onset of atherosclerosis is triggered by the retention of numerous plasma lipoproteins, including low-density lipoprotein (LDL) and apolipoprotein B (ApoB), in the subendothelium of arterial vessels[6]. Oxidative modification of the retained lipoproteins facilitates the activation of endothelial cells and recruitment of monocytes into the subendothelium[3]. After these events, monocytes differentiate into various other phagocytic cell types, such as dendritic cells (DCs) and macrophages. These differentiated phagocytes mature and generate a persistent immune response that results in the continuation of the atherosclerotic process and plaque buildup. Specifically, it is known that a high burden of DC accumulation within plaques is predictive of more severe atherosclerotic disease, and represents a more "vulnerable" plaque phenotype that is more prone to rupture and associated complications (MACEs, etc.)[5]. The non-invasive assessment of these cellular processes would allow for earlier detection and assessment of CVD progression and would thereby provide an opportunity for therapeutic intervention before the occurrence of life-threatening outcomes, such as MI or stroke.

1.2.2. Molecular Imaging

Molecular imaging is a useful tool for diagnosing CVD[7-10] and allowing for the non-invasive detection, tracing, and quantification of single cell populations[11, 12]. Modalities for molecular imaging include magnetic resonance imaging (MRI), positron emission tomography (PET), and acoustic imaging methods. These methods differ in their spatial resolution, detection sensitivity, and imaging depth[13, 14]. PET imaging offers high sensitivity and imaging depth, but it is limited by the lack of anatomic information[15]. Acoustic imaging modalities, including

ultrasound (US) and photoacoustic imaging (PAI), have good detection sensitivity, but suffer from a relatively low penetration depth[15]. In comparison, MRI provides numerous advantages including high imaging depth, spatial resolution, soft tissue contrast, and lack of ionizing radiation, while being limited by low sensitivity[13]. From this point forward, I will focus on MRI due to these advantages and due to its extensive use in the research presented in this dissertation.

1.2.2.1.   Magnetic Resonance Imaging

MRI is built upon the principles of nuclear magnetic resonance (NMR)[16, 17], allowing for generation of images using the distribution of ^{1}H nuclei in different water-rich or fat-rich tissues in the body[18]. Briefly, radiofrequency (RF) pulses are used to align the magnetic moments of these nuclei in a sample, after which they are "tipped" away from this alignment by a secondary magnetic field[19]. The recovery, or relaxation, of the magnetic moments back to equilibrium after this "tipping" occurs in two forms: longitudinal relaxation or transverse relaxation. By measuring the longitudinal relaxation time (T1 time) or transverse relaxation time (T2 time) for different ^{1}H nuclei across a sample, an MR image can be generated, with spatial contrast in the image arising from the differences in T1 and T2 relaxation times of different tissues[19]. Intrinsic differences in tissue T1 and T2 relaxation times can be leveraged through the use of different image acquisition modes, or T1- or T2-weighted images, to differentiate certain types of tissue depending on the application. As an example, T1-weighted imaging can be used to assess for subacute bleeds in the brain, as blood will have shorter T1 times and appear brighter than surrounding tissue in this specific pathology[20].

The use of exogeneous contrast agents is usually required in order to detect more specific pathologic processes, such as inflammation, cancer, or vascular defects. Currently, almost half of

all clinical MRI studies performed use contrast agents to enhance diagnostics[21]. These contrast agents shorten the T1 or T2 relaxation times (or both) of nearby water molecules (the source of the ^{1}H nuclei), resulting in increased signal intensity (brightening) on T1-weighted images and decreased signal intensity (darkening) on T2-weighted images[22]. As such, strong T1 shortening agents are referred to as positive agents, and strong T2 shortening agents as negative agents.

MRI contrast agents also fall into two major categories based on their composition: (i) paramagnetic ion complexes, which are mostly positive agents, and (ii) superparamagnetic metal ferrite particles, which are mostly negative agents[22]. Paramagnetic contrast agents are primarily comprised of lanthanide elements such as gadolinium (Gd), which is very strongly paramagnetic due to its 7 unpaired electrons[21]. For contrast enhancement, the gadolinium (III) ion is delivered via a chelation complex. Such gadolinium-based contrast agents (GBCAs) generally contain an octadentate polyaminopolycarboxylato-based ligand that is either linear in structure, like diethylenetriamine pentaacetate (DTPA), or macrocyclic, like dodecane tetraacetic acid (DOTA)[23]. Importantly, these GBCAs have a ninth coordination site that is accessible for water ligation, where the coordinated water molecule can undergo exchange with other water molecules in the environment[21]. It is the ability of Gd to induce relaxation of multiple surrounding water molecules as this exchange occurs that results in the shortening of T1 times of the surrounding tissue and the subsequent enhancement in contrast.

The other major category of MRI contrast agents, superparamagnetic contrast agents, are not small molecules but are instead particles having a size in the range of 4-20 nm[22]. These particles are primarily composed of numerous smaller crystallites or clusters of magnetic ions[22]. These crystallites are usually iron-based, though the composition can vary to include manganese, cobalt,

copper, and other metals[24, 25]. These compounds are also referred to in the literature as magnetic nanostructures[26] (MNS) or superparamagnetic iron oxide nanoparticles (SPIONs). Due to the superparamagnetic nature of these MNS, when subjected to an external magnetic field the crystallites in MNS align with the field and the bulk material is magnetic. When this external magnetic field is removed, the MNS are no longer magnetic as the crystallites revert back to their initial random orientations[22]. Superparamagnetic contrast agents generally have a strong effect on T2 relaxation of nearby water molecules, resulting in shortening of T2 times of the surrounding tissue and negative contrast enhancement. However, some superparamagnetic compounds can also serve as T1 agents by shortening T1 times.

MRI contrast agents can also be categorized based on their biodistribution and resulting applications, specifically into extracellular fluid (ECF) agents, intravascular agents (blood pool contrast agents or BPCAs), and "organ-specific" contrast agents[22]. ECF agents for MRI, such as the Gd-chelates Gd-DTPA and Gd-DOTA, are administered intravenously and subsequently disperse into the extracellular space[21]. Intravascular MRI contrast agents persist in circulation much longer than ECF agents and have applications for vascular imaging[22]. Finally, "organ-specific" contrast agents are those that have preferential uptake within certain organs or tissues, primarily the liver. Some examples of "organ-specific" contrast agents include iron oxide-based superparamagnetic agents, and certain GBCAs including gadoxetate disodium (Gd-EOB-DTPA)[22]. However, the biodistribution of "organ-specific" contrast agents relies on passive targeting and is not useful for imaging of specific cellular processes in the liver or elsewhere in the body.

In general, current gold-standard small molecule contrast agents for all molecular imaging modalities, such as GBCAs for MRI or fluorodeoxyglucose (FDG) for PET imaging, are not cell-specific and rely on other strategies such as impaired vasculature or increased cell metabolism to enhance uptake[15]. For imaging of cellular processes, like imaging of cell-mediated inflammation in CVD, targeted delivery of molecular imaging contrast agents to specific cells, tissues, or markers upregulated in disease processes is needed. Thus, the ability of nanomaterials to achieve targeted cargo delivery makes them intriguing platforms for contrast agent delivery applications, especially for those seeking to acquire insightful imaging data of specific pathological features (e.g., monitoring the development of atherosclerotic plaques, etc.).

1.2.3.   Nanomaterials

Nanocarriers are colloidal materials with at least one aspect of their dimensions in the range of 1 – 1000 nm[27]. They have been studied extensively in recent decades for their use as drug delivery vehicles, largely due to their ability to improve the bioactivity, pharmacokinetics, solubility, and stability of encapsulated therapeutic cargo. Various types of nanocarriers are being explored for therapeutic applications, including liposomes[28], solid lipid nanoparticles[29], magnetic nanoparticles[25], quantum dots[30], and polymer-based systems[31] such as polymeric micelles, vesicles, filamentous structures[32], and dendrimers. Of these, self-assembled polymeric nanocarriers offer great versatility, enhanced stability, ease of fabrication, and opportunities for rational design and control over the morphology of the delivery vehicle.

One notable system of self-assembled polymeric nanocarriers used extensively in this thesis work is the diblock co-polymer poly(ethylene glycol)-*block*-poly(propylene sulfide), or PEG-*b*-PPS[33-36]. This polymer system was first introduced in 2001 by the work of the Hubbell

Group[33], and the Scott Group has also subsequently used this polymer system to form nanocarriers with a wide range of morphologies for drug delivery applications. Notably, work from the Scott Group has since shown that PEG-*b*-PPS micelles[36] (MCs), wormlike filomicelles (FMs)[37], vesicular polymersomes (PSs)[38], and bicontinuous nanospheres (BCNs)[39] can be successfully fabricated via the rapid and scalable self-assembly method of flash nanoprecipitation. Of these, BCNs are the newest and most complex nanocarrier morphology assembled from PEG-*b*-PPS, with characteristic structure of multiple intertwined bilayer membranes[39-41]. Thus far, work with BCNs has focused on characterizing their ability to encapsulate and deliver small molecule cargo and understanding their biodistribution. Since these are relatively new nanostructures, there is still much work to be done on exploring and characterizing the utility of BCNs for encapsulation and delivery of nanoscale cargo and for targeted delivery applications. Other work on PEG-*b*-PPS nanocarriers has leveraged the oxidation sensitivity of the PPS block, demonstrating the shift of PEG-*b*-PPS nanocarriers from one morphology to another, such as the "cylinder-to-sphere" transition of FMs to MCs[37]; and employing the oxidative transition of PS[42] or BCN to MC for intracellular cargo delivery[40].

1.2.3.1. Targeting of Nanocarriers via Surface-displayed Moieties

The overall utility of nanocarriers predominantly arises from their ability to facilitate site-specific delivery of encapsulated cargo. This is most often achieved through the decoration of nanocarrier surfaces with targeting moieties specific for markers upregulated in certain pathologies, such as cancer[43]. As an example, many cancers overexpress the folate receptor (FR) on cell surfaces, allowing for targeting of these cells via folate-decorated nanocarriers[44]. In this case, the targeting moiety (folate) is a small molecule, specifically a vitamin. Other classes of

targeting moieties include peptides or proteins, such as antibodies or antibody fragments; nucleic acids, such as aptamers; and other small molecules, such as carbohydrates[43].

For decoration of nanocarrier surfaces with these targeting moieties, a method resulting in stable and efficient display of the targeting agent must be employed. Most often, nanocarrier surfaces are chemically modified or functionalized to allow for covalent conjugation of the desired targeting moiety. These covalent reactions often involve use of carbonyl, amine, sulfhydryl, or azide reactive groups for the formation of hydrazide, amide, thioester, or disulfide bonds, among others[45]. Non-covalent strategies are also employed, including linkages using biotin-(strept)avidin binding for surface display of cell-penetrating peptides[46] or charge-based interactions for display of targeting aptamers[47]. Finally, a third strategy for display of targeting moieties is the use of lipid tail constructs that can insert into nanocarrier membranes and display the targeting moiety[48-50]. These lipid tails can be incorporated into nanocarrier membranes during or after assembly and have key advantages over covalent linkage of targeting moieties, including precise control over the surface density of the moiety of interest, control over the PEG spacer length to ensure display of the targeting moiety above any PEG corona of the nanocarrier itself[51], and a modular synthetic approach allowing for use of these PEG-lipid tail constructs with a variety of vesicular or micellar nanocarriers[48, 50].

1.2.4.   Nanomaterials for Molecular Imaging

Due to their ability to target specific cells and tissues via such surface-displayed targeting agents, nanomaterial-based strategies have been of great interest in recent years for contrast agent delivery, particularly in immune cells[36]. Several nanomaterial systems exist for pre-clinical imaging, including metallic nanoparticles[52], amphiphilic polymers[53], solid core polymeric

nanoparticles[54], and lipid-based nanoparticles[55]. The molecular imaging signal provided by these nanoparticles arises from either their composition, as in the case of metallic nanoparticles like MNS for MRI[56], or through encapsulation or conjugation of small molecules including Technetium-99 (^{99}Tc) for PET imaging[57]. Single cell targeting via nanoparticles can be accomplished through numerous methods such as the use of targeting moieties like antibodies or peptides[58], and *ex vivo* labeling[59]. The use of such nanoparticle platforms towards diagnostic, therapeutic, or combined (theranostic) applications in cardiovascular disease have been reviewed previously[60], with some reviews focusing on a specific imaging modality[61, 62] or nanoparticle design[63] but still covering a wide range of CVD applications. However, with the rapid progression of pre-clinical research in the field of cardiovascular imaging and the emerging developments in nanoparticle targeting to specific cell populations, an updated overview of the field is of interest. The following is a summary of the latest breakthroughs in assessment of cellular processes in CVD via nanoparticle-mediated molecular imaging, with a focus on detecting inflammation, assessing lipid accumulation, and monitoring tissue regeneration.

1.2.4.1.   Targeting Macrophage-derived Vascular Inflammation

Cell-mediated inflammation is known to be a key factor in atherosclerosis, contributing to plaque instability and risk of rupture[4]. Targeting and assessing the immune cell burden within plaques using nanomaterials is a promising strategy for assessing plaque burden and development. While plaques contain a complex mixture of immune cells that include DCs and T cells, macrophages have emerged as one cell of interest for molecular imaging-based plaque detection due to their major role in plaque progression[64].

For this purpose, diverse ligands established for targeting macrophages have been utilized to decorate nanoparticles, including antibodies against markers of monocyte-macrophage lineage. Tarin *et al.* demonstrated macrophage targeting specificity of gold-coated iron oxide nanoparticles conjugated with anti-CD163 (NP-CD163) over non-targeted, IgG-conjugated control nanoparticles (NP-IgG), and found that NP-CD163 were more effectively able to target and allow T2 MRI visualization of plaques[65]. Similarly, anti-CD68 antibody-mediated targeting was shown to be effective at targeting iron (Fe)-doped hollow silica nanospheres (Fe-HSNs) to plaque macrophages. The multifunctional Fe-HSNs allowed for real-time plaque monitoring via US and follow-up examination of plaque macrophages using the 3D spatial resolution of MRI, indicating a robust tool for real-time, single-cell imaging in CVD[11].

Other approaches have leveraged the overexpression of specific cell-surface markers by plaque macrophages as a targeting strategy. Class A1 scavenger receptors (SR-A1) have emerged as a plaque macrophage target, as it has been found to be overexpressed in activated macrophages and facilitates their uptake of oxidized LDL[66]. With this rationale, a unique theranostic nanoparticle was developed by Ye *et al.* using dextran sulfate (DS)-labeled, chitosan-poly(lactic-co-glycolic acid) (PLGA)-iron oxide-perfluorohexane (PFH) nanoparticles to plaque macrophages via SR-A1[66]. The iron oxide facilitated MRI imaging to visualize plaques, while the PFH allowed for subsequent ablation and apoptosis induction in targeted plaque macrophages via low intensity focused ultrasound (LIFU). This application demonstrated the importance of theranostics but will require further investigation into potential post-ablation consequences, such as unwanted plaque destabilization and rupture. A different, less specific approach was taken by Zheng *et al.*, in which near infrared fluorescence (NIRF)-detectable, deoxyribonucleic acid (DNA)-coated SPIONs

(DNA-SPIONs) targeted macrophages via binding to SR-A1 and more efficiently localized to aortic plaques than PEG-coated SPIONs[67]. However, the DNA-SPIONs were also found to have high uptake into liver and splenic macrophages and DCs, indicating that additional targeting agents may be necessary for plaque macrophage specificity. Another highly expressed receptor in infiltrated plaque macrophages is transferrin receptor 1 (TfR1). Liang *et al*. developed a PET-detectable nanomaterial that labeled the targeting compound heavy-chain ferritin with ^{99m}Tc to enhance association with TfR1-positive plaque macrophages[68]. This nanoconstruct produced a PET signal with increased strength, specificity, and diagnostic power relative to small molecule contrast agents that are currently proposed as gold standards for PET detection of plaque burden via passive targeting.

To specifically assess more vulnerable plaques, recent strategies have focused on identifying apoptotic macrophages in plaques via Annexin V-mediated targeting. Li *et al*. developed a single-photon emission computerized tomography (SPECT)/CT active construct of ^{99m}Tc- and Annexin V-tagged gold nanoparticles that localized signal to actively apoptotic cells prominent in atherosclerotic lesions in *ApoE*$^{-/-}$ mice[69]. Similar work from this group has demonstrated the use of ^{99m}Tc- and Annexin V-tagged SPIONs for SPECT/MRI-based assessment[70]. By targeting such specific functional markers and employing multi-modality imaging, these strategies minimize the theoretical dose of solid metal nanoparticle contrast agents needed to effectively detect high-risk plaques.

Other inflammation-targeted strategies for CVD imaging utilize natural nanoparticles such as high-density lipoproteins (HDL) for cell selectivity. Several studies have used HDL-mediated targeting to access macrophages in plaques. One notable study was conducted by Perez-Medina

through the [89]Zr-labeling of HDL for PET-based assessment of plaques[71]. The [89]Zr-HDL nanoparticles showed a strong PET signal associated with damaged vessel walls in murine, rabbit, and porcine models, with enhanced uptake into plaque monocytes and macrophages. Subsequent work has built upon this HDL-mediated plaque targeting platform. Notably, Binderup *et al.* leveraged the use of MRI, PET, CT, and NIRF to assess the use of the [89]Zr-HDL nanoparticles to load and deliver simvastatin for atherosclerosis immunotherapy in rabbit and porcine models, demonstrating the efficacy of their treatment at targeting and inhibiting inflammatory macrophages in atherosclerotic plaques[72].

1.2.4.2.   Targeting Non-Macrophage-Derived Inflammation

Aside from atherosclerosis, other areas of CVD are also marked by cell-mediated inflammation. Acute rejection (AR) following heart transplantation is a key complication and cause of graft disability and is known to be mediated by T lymphocyte infiltration[73]. As an alternative to the invasive, current gold standard of endomyocardial biopsy to detect AR, US-visible anti-CD3-labeled nanobubbles have been employed to detect AR after cardiac transplantation *in vivo*[12]. Targeted nanobubbles were able to noninvasively assess T lymphocyte infiltration in studies comparing isograft and allograft transplantation[12].

Thrombosis is another CVD complication driven by single cell components (or in this case fragments), namely activated platelets, and can lead to severe complications if not detected early. Bonnard et al. recently developed low-fouling, biodegradable NIRF stealth nanoparticles for noninvasive molecular imaging of thrombosis[74]. In the cited study, the particles were functionalized with a single-chain variable fragment antibody specific to the activated form of the glycoprotein IIb/IIIa (anti—GPIIb/IIIa-scFv), the most prominent marker expressed by platelets

upon activation. The functionalized particles facilitated targeting and non-invasive visualization of rat carotid thromboses. Fucoidan labeling of nanoparticles is another strategy used to achieve activated platelet targeting via binding to P-selectin, and was used by Li *et al.* to deliver fucoidan-functionalized microbubbles to selectively target and visualize thrombi via US imaging[75]. Interestingly, the authors showed that these microbubbles could also be burst using destructive US pulses, which they suggested could be used to trigger drug release in follow up studies as a theranostic approach. Other nanoparticle-based approaches to non-invasively visualize thromboses focus on targeting non-cellular components such as fibrin or thrombin or responding to the microenvironment around a thrombus, and are summarized elsewhere[76].

Finally, others have attempted to develop nanoparticles for imaging that simultaneously target multiple inflammatory cells within atherosclerotic plaques, in addition to macrophages. Using an optimized antagonist to the integrin α4β1, which is a non-RGD binding integrin expressed on multiple immune cell types, Woodside *et al.* used Gd-loaded liposomes to target and non-invasively detect atheromas of *ApoE^{-/-}* mice via MRI[77]. The rationale for this approach was to analyze the entire inflammatory cell burden within plaques. The authors discovered that their construct localized to mainly monocytes and macrophages in the subendothelium, along with neutrophils, with no uptake into nearby endothelial cells or cardiomyocytes.

1.2.4.3. Visualizing lipid accumulation

Lipid accumulation is another major factor in the development of atherosclerosis. Lipoprotein retention, modification, and internalization by macrophages and vascular smooth muscle cells (VSMCs) in the vessel subendothelium contributes to the formation of foam cells. These foam cells participate in further immune cell recruitment and promote plaque progression[78].

Targeting foam cells is therefore another strategy for assessing lipid accumulation and plaque burden. The overexpression of osteopontin (OPN) by both macrophage- and VSMC-derived foam cells was targeted by Li *et al.* to deliver dual-modality nanoparticles for detection of vulnerable atherosclerotic plaques[79]. These nanoparticles were composed of a perfluorooctyl bromide (PFOB) core to provide US contrast, a polylactic acid (PLA) surfactant coating, and decorated with fluorescent dye Cy5.5 for optical imaging and anti-OPN antibody for foam cell targeting.

A theranostic approach was taken by Gao *et al.*, who utilized NIR- and acoustic imaging-responsive, copper sulfide nanoparticles labeled with antibodies to transient receptor potential cation channel subfamily V member 1 (TRPV1) cation channels (CuS-TRPV1 nanoparticles) to target VSMCs and inhibit foam cell formation via binding to TRPV1[80]. Upon IV injection, CuS-TRPV1 nanoparticles were found to successfully target plaque VSMCs and facilitate PA imaging to visualize plaques in *ApoE-/-* mice, as compared with non-targeted CuS nanoparticles. Following PA-mediated plaque visualization, CuS-TRPV1 nanoparticles could be photothermally activated via NIR light, activating the thermosensitive TRPV1 cation channel and triggering autophagy to control lipid metabolism. After repeated photothermal treatments, this approach successfully inhibited VSMC-derived foam cell formation and mitigated plaque progression.

As an alternative strategy for foam cell targeting, Wei *et al.* utilized platelet-membrane coated, Gd-loaded PLGA nanoparticles (PNP) to detect vulnerable plaques via MRI. In this strategy, the platelet membrane coating was employed for targeting multiple molecular and cellular targets, including foam cells. The group demonstrated that PNPs could target foam cells along with activated endothelial cells and collagen, labeling this approach "multifactored biologic targeting." Further studies demonstrated the ability of the PNPs to allow live MRI imaging and to

target plaques in various stages of development in *ApoE-/- mice*[81]. Overall, targeting foam cells is a promising method for non-invasive detection of vulnerable plaques but needs further assessment.

1.2.4.4. Tracking tissue regeneration

A third, unique area of single cell-mediated activity in CVD is tissue regeneration. Following cardiac injury, endogenous regenerative mechanisms are not always sufficient to replace injured tissue. To address this, stem cell administration is of interest for replacing damaged myocardium, requiring a non-invasive method to assess cell migration and activity post-administration[82]. SPIONs are well-established for cellular tracking as they can efficiently label stem cells without transfection agents and allow for non-invasive MRI monitoring. This approach was used by Hua *et al*. to track bone marrow mesenchymal stem cells (BMSCs) in rat models of MI[83]. While the negative contrast signal of the SPION-labelled BMSCs was significant one day post-administration, by day 21 the signal intensity had decreased and was indistinct from surrounding tissue. Unfortunately, this study did not present sufficient timepoints to provide insight into the signal variance between day 1 and day 21 post-administration. Other MRI-based cell tracking approaches such as ^{19}F-MRI avoid this issue of low signal intensity, given that ^{19}F has no background tissue signal. Perfluorocarbon nanoparticles (PFCE-NPs) suitable for ^{19}F-MRI detection have been explored for labeling and tracking of stem cells. Constantinides *et al.* used the transfection agent FuGENE to facilitate labeling of two different murine cardiac progenitor cells with PFCE-NPs, allowing for *in vivo* tracking up to 8 days post-injection[84]. Other strategies to minimize background signal in cell tracking applications include PAI via semiconducting polymers (SP), which have specific and narrow photoacoustic spectra leading to low background signal. SPs-based PAI nanoprobes with cell-penetrating peptides as a surface modification have

been developed to track the delivery and engraftment of human embryonic stem cell-derived cardiomyocytes in living mouse hearts for the treatment of ischemic heart disease[85]. The most effective approach to increase cell-tracking sensitivity while minimizing background signal may be through strategic combinations of imaging modalities. Lemaster *et al.* designed a trimodal contrast agent "nanobubble" for US, magnetic particle imaging (MPI), and photoacoustic imaging via assembly of PLGA, iron-oxide, and the fluorescent dye 1,1′-dioctadecyl-3,3,3′,3′-tetramethylindo-tricarbocyanine iodide (DiR)[86]. These nanobubbles were used to label and track cardiac stem cells following intramyocardial injection, and demonstrated high temporal resolution, imaging depth, and contrast due to the unique combination of modalities employed in the study.

1.2.4.5.   Summary

Here, I have reviewed the recent uses of nanomaterials for imaging cellular processes in CVD, with a focus on monitoring and visualizing inflammation, lipid accumulation, and tissue regeneration. I found that while these recent studies employed a range of modalities, MRI and PET were by far the most commonly used. The minimal use of CT was surprising considering its widespread clinical use. Studies mainly employed CT to provide anatomic context in combination with plaque detection via other modalities[69, 72]. Delivering nanoparticles to single cell targets was primarily achieved via specific antibodies that bind to cell-surface receptors, such as CD163[65] or transferrin receptor-targeting[68] for targeting plaque macrophages, or through *ex vivo* labeling in the case of cell tracking. These studies illustrated how cell-selective active targeting is superior to current conventional molecular imaging contrast agents, primarily through enhanced uptake by and specificity for atherosclerotic plaques or other biologic processes of interest. Furthermore, active targeting of nanoparticles to specific cells known to correlate with vulnerable or early active

plaques provides more powerful diagnostic assessment of plaque burden and risk stratification. In comparison, passive targeting strategies mainly prolong diagnostic nanoparticle circulation time[87] and aim to enhance general plaque localization, but fail to provide details on cellular composition that give further insight on the underlying pathology.

While these studies represent progress in this area, there are specific areas that require improvement and future investigation. Most of the current strategies for assessing plaque burden through single cell targeting focus on targeting macrophages and monocytes. However, other cells such as DCs are also known to facilitate atherogenesis[88] and are correlated with more advanced and vulnerable plaques[89] and should be a focus of future non-invasive plaque assessment strategies, as current approaches are lacking. Additionally, given that both DCs and macrophages are implicated in atherosclerosis development, the ratio between these two cell types would be intriguing to assess as a potential metric of plaque progression.

Furthermore, the inability to evade the mononuclear phagocyte system (MPS) resulting in clearance through the liver is a key limitation of many current approaches. Though the studies discussed in this chapter illustrate the accumulation of intravenously injected nanoparticles in aortic plaques, those that assessed nanoparticle biodistribution found that the majority of the injected nanoparticles are cleared by the liver[67, 71, 72]. For the purposes of CVD diagnosis and intervention, improved targeting methods will be required to enhance site- and cell-specific uptake, while lowering MPS clearance.

Emerging methods to achieve enhanced active targeting include combining nanoparticle shape-based targeting with receptor-targeted methods[90]. Yi *et al*. demonstrated nanostructure enhanced targeting (NSET), wherein vesicular polymersomes (PSs) achieved significantly higher

uptake by DCs within atherosclerotic lesions compared to smaller spherical micelles or high aspect ratio filamentous structures[36]. In subsequent work, they improved upon this NSET strategy by engineering PS surfaces for optimal display of the P-D2 targeting peptide that is specific for DC surface receptors. This approach demonstrated significantly higher DC selectivity when the two methods of shape-based targeting and receptor targeting were combined[50].

Finally, the field is currently building upon the use of nanomaterials for CVD diagnostic applications, such as detecting various stages of atherosclerosis by targeting unique cell populations and focusing more on theranostic approaches. In such cases, following initial plaque detection and assessment, a therapeutic functionality of the nanoparticle can be employed such as target cell ablation via LIFU[66] or reactive oxygen species (ROS) scavenging to limit inflammation[91].

While the majority of nanoparticle-based systems are still in pre-clinical studies, the field of nanomaterials is progressing rapidly. Given this, it is expected that nanoparticles for diagnostic, therapeutic, and theranostic uses towards cellular processes in CVD have immense potential and will continue to increase in utility and start to transition to clinical studies in the years to come.

1.3. Scope of this Work

Multiple small molecule and nanoscale contrast agents exist currently for providing MRI contrast enhancement, but a number of challenges limit their diagnostic and theranostic applications. These challenges include the ability to achieve stable delivery *in vivo* with minimal clearance via the liver, and lack of targeting specificity for specific disease processes. The use of PEG-*b*-PPS nanocarriers show promise for addressing these challenges, as previous studies demonstrate that this platform facilitates the simultaneous delivery of multiple therapeutic cargo,

as well as cargo delivery to cells of interest in certain disease processes[36, 38, 39, 48, 50]. For example, PEG-*b*-PPS BCNs are capable of achieving concurrent delivery of hydrophilic and hydrophobic cargo[39] with high uptake in the spleen as compared with the liver[41], and PS displaying the P-D2 targeting peptide (P-D2-PS) have been shown to enhance uptake in DCs in atherosclerotic plaques[50]. Therefore, PEG-*b*-PPS nanocarriers have the potential to enhance the delivery of MRI contrast agents, such as metal ferrite magnetic nanostructures, as well as for facilitating targeted delivery of such contrast agents for imaging of specific disease processes like atherosclerotic plaque development. On the way to achieving these objectives, certain key questions need to be addressed.

Can magnetic nanostructures be stably and efficiently encapsulated within PEG-*b*-PPS nanocarriers for targeted delivery applications? What are the resulting MRI and superparamagnetic properties of these mixed metal and polymeric nanocarriers? Can PEG-*b*-PPS PS be engineered to provide T1 MRI contrast enhancement? What is the dendritic cell:macrophage ratio in mouse aortas at multiple stages of heart disease? What is the immune cell uptake profile of P-D2-PS in mouse aortas at multiple stages of heart disease? These questions inspired the research covered within this dissertation and have been addressed by the studies described herein.

1.4.   Publications in this Chapter

Sections of this chapter have been published with the following citation information:

Modak, M.; Frey, M. A.; Yi, S.; Liu, Y.; Scott, E. A., Employment of Targeted Nanoparticles for Imaging of Cellular Processes in Cardiovascular Disease. *Current Opinion in Biotechnology* **2020,** *66*, 59-68.

CHAPTER 2

2. Development and Characterization of Metal Ferrite MNS-loaded PEG-*b*-PPS

Nanocarriers for Drug Delivery and T2 MRI

2.1.   Abstract

Magnetic nanostructures (MNS) have a wide range of biological applications due to their biocompatibility, superparamagnetic properties, and customizable composition that includes iron oxide (Fe3O4), Zn2+, and Mn2+. However, several challenges to the biomedical usage of MNS must still be addressed, such as formulation stability, inability to encapsulate therapeutic payloads, and variable clearance rates *in vivo*. To address these problems, the use of self-assembled polymeric nanocarriers is of interest, as they allow for the fabrication of nanocarriers with defined hydrophobic and hydrophilic domains. Encapsulation of MNS within such nanocarriers would permit more efficient control over the delivery of MNS without altering their superparamagnetic properties and permit concurrent delivery of additional therapeutic cargo. In this chapter, I explore the encapsulation of MNS within polymeric bicontinuous nanospheres (BCNs), micelles (MCs), and polymersomes (PSs) composed of poly(ethylene glycol)-*block*-poly(propylene sulfide) (PEG-*b*-PPS) copolymers for controlled delivery applications.

2.2.   Introduction

2.2.1.   Magnetic Nanostructures

Due to their superparamagnetic properties, thermal activation ability, ease of fabrication, and biocompatibility, magnetic nanostructures (MNS) have been of great interest for theranostic strategies, offering advantages for both diagnostic imaging and therapeutic delivery[92]. MNS are solid-core magnetic nanoparticles composed primarily of metal ferrites that fall in the size range

of 4-20 nm[24, 26, 93]. Their superparamagnetic nature allows them to be magnetized under an external magnetic field as well as revert to a non-magnetic state when the magnetic field is removed, presenting intriguing biomedical utility[25]. To date, few MNS formulations have been approved for clinical use[94, 95]. One example is Ferumoxytol, a hydrophilic surface functionalized MNS formulation approved specifically for the treatment of iron deficiency in anemic patients. However, concerns about adverse events and allergic reactions may limit its potential[96]. While several hydrophilic dextran-functionalized MNS such as ferumoxides were previously approved by the FDA as magnetic resonance imaging (MRI) contrast agents, they have since been withdrawn from clinical use due to safety concerns[97]. Hydrophobic surface functionalized MNS, including metal ferrite nanocrystals[98], have also been reported; however, these nanomaterials often require the usage of stabilizing agents to optimize delivery[99-101]. MNS currently in pre-clinical development suffer from critical issues such as formulation aggregation and variable clearance rates *in vivo*[102]. Therefore, a suitable delivery system that can simultaneously load and deliver both MNS and other cargoes could enhance applications of MNS by addressing these limitations.

2.2.2. Self-assembled Materials

Self-assembled materials allow for the controllable production of nanocarriers with defined hydrophobic and hydrophilic domains. Encapsulation of MNS within a suitably stable self-assembled nanocarrier would permit more efficient control over the delivery of MNS while maintaining their superparamagnetic properties, as well as allow for concurrent delivery of additional therapeutic cargo. Recently, nanocarriers including liposomes[103], polymersomes[104], and polymeric micelles[105] have been explored as delivery vehicles for iron oxide-based MNS. However, drawbacks to these systems include ineffective MNS loading, weak contrast

enhancement, aggregation, and poor stability *in vivo*[106, 107]. Hence, subsequent efforts have moved toward the development of highly organized magnetic lipid cubosomes[108, 109] or magnetic nanocapsules[110]. Cubosomes are complex nanostructures usually composed of polar lipids such as glycerol monooleate that have intertwined polar and nonpolar channels[111]. While these bicontinuous lipid systems may allow for the increased cargo loading, they suffer from drawbacks including the need for high temperature or pressure for their formation and the need for surfactants to limit aggregation due to exposed lipid regions[111].

2.2.3.   Bicontinuous Nanospheres

Bicontinuous nanospheres (BCNs) are polymeric analogues to lipid cubosomes with advantages including uniformity and stability that have recently attracted attention for biomedical applications[39, 112, 113]. Although fabrication of BCNs has typically been limited to small scale and polydisperse batches[112], poly(ethylene glycol)-*block*-poly(propylene sulfide) (PEG-*b*-PPS) copolymers have recently been found to assemble monodisperse BCNs via the scalable method of flash nanoprecipitation (FNP)[38, 39]. FNP is currently the only method capable of forming monodisperse PEG-*b*-PPS BCNs in a reproducible and scalable manner[38, 39]. PEG-*b*-PPS is a nontoxic, nonimmunogenic self-assembling block copolymer system that can form diverse oxidation-responsive nanostructures depending on the PEG weight fraction (f_{PEG})[114, 115]. PEG-*b*-PPS nanostructures have proven advantageous for the controlled delivery of therapeutics as their lyotropic membranes are highly stable yet bioresponsive to *in vivo* oxidation for safe degradation and clearance, which has been validated in both mouse and primate animal models[50, 116-118]. Importantly, PEG-*b*-PPS BCNs have a high internal surface area due to their interwoven hydrophobic bilayer membranes and aqueous channels, enabling them to co-load both small and

large molecule payloads without disturbing the morphological integrity[39]. The BCN self-assembled architecture provides enhanced stability to accommodate high levels of hydrophobic and hydrophilic cargo relative to other nanostructure morphologies such as micelles and vesicular polymersomes[41, 113]. We hypothesized that this enhanced loading capacity and stability could prove useful for encapsulating nanoscale cargo like MNS concurrently with small molecule therapeutic cargo. Furthermore, the oxidation-responsive behavior of PEG-*b*-PPS polymer has been proven to be highly versatile for triggered release, allowing on-demand nanocarrier disassembly as well as inducible transitions in nanostructure morphology[113, 116, 119].

The aim of this work was to explore the encapsulation of MNS within PEG-*b*-PPS nanocarriers for drug delivery applications. Here, I discuss my development and characterization of MNS-encapsulated micelles, polymersomes, and bicontinuous nanospheres, focusing primarily on this last morphology.

2.3. Results and Discussion

2.3.1. Self-assembly and Physicochemical Characterization

We have recently demonstrated that PEG-*b*-PPS block copolymers can self-assemble into morphologically diverse nanostructures, ranging from simple spherical MCs and vesicular PSs to highly organized BCNs via the technique of FNP[38, 39, 116, 117]. Among these nanostructures, BCNs possess high internal surface area with a large hydrophobic volume that can accommodate the encapsulation of a wide range of therapeutic payloads[39]. I therefore aimed to embed nanoscale hydrophobic MNS payloads (sub-10 nm) within the hydrophobic volume of larger, self-assembled
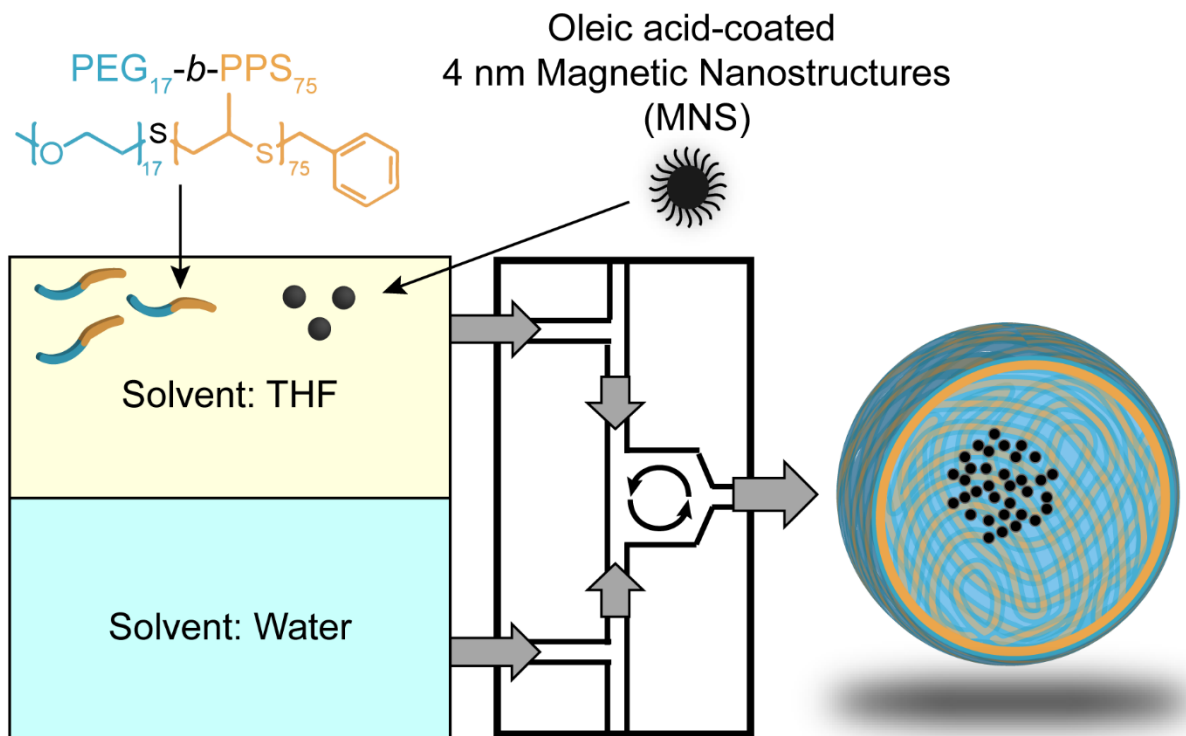
Figure 2-1. Schematic of the assembly of MBCNs using the FNP method. PEG$_{17}$-*b*-PPS$_{74}$ copolymer and 4 nm oleic-acid coated MNS were both dissolved in THF and impinged against water in a confined impingement jet (CIJ) mixer to form MBCNs.

BCNs to allow more versatile control over *in vivo* MNS delivery. However, the loading of such ultra-small nanoparticles into self-assembled nanostructures often poses great challenges concerning nanostructure integrity, ease of fabrication, low encapsulation, and aggregation[120, 121].

FNP is a rapid, scalable nanoprecipitation technique, which permits concurrent loading of hydrophobic and hydrophilic payloads, including both small and macromolecules[122]. I envisioned that FNP could allow the encapsulation of ultra-small MNS within BCNs without compromising nanostructure integrity. I therefore loaded 4 nm oleic-acid coated $Zn_{0.2}Mn_{0.8}Fe_2O_4$ nanoparticles as hydrophobic MNS into PEG-*b*-PPS BCNs using the FNP technique (Figure 2-1). The loading of 4 nm hydrophobic MNS into bilayer membranes of BCNs was found to be a rapid and facile process using the FNP method. The structural integrity of the resulting magnetic bicontinuous

nanospheres (MBCNs) was confirmed using dynamic light scattering (DLS), cryogenic electron microscopy (cryo-TEM) and small-angle x-ray scattering (SAXS) studies. DLS analysis of MBCNs showed a Z-average diameter of 330 nm, and neither the diameter nor the zeta potential of the MBCNs was significantly different than unloaded BCN controls (Table 2-1). Cryo-TEM of the MBCNs (Figure 2-2a) revealed the presence of aqueous channels (white arrows) inside the nanocarriers with MNS particles (black dots) embedded in the hydrophobic bilayers. The presence of aqueous channels inside MBCNs is consistent with blank BCNs as demonstrated with our previous cryo-TEM studies[39]. Importantly, MNS loading did not disrupt nanocarrier assembly as the characteristic size and cubic architecture of BCNs was retained, as demonstrated via small-angle X-ray scattering (SAXS) (Figure 2-2b). The scattering curves in Figure 2-2b show that both blank BCNs (black line) and MBCNs (red line) have characteristic Bragg spacing ratios at $\sqrt{2}$, $\sqrt{4}$ and $\sqrt{8}$, respectively. These Bragg spacing ratios indicate the presence of primitive type (*Im3m*) cubic internal organization. The lattice constant (a_{Im3m}) calculated using SAXS for the blank and MNS loaded BCNs was found to be 31.5 and 32.1 nm, respectively.

Table 2-1. Diameter, PDI, and zeta potential of blank BCNs and MBCNs.

	Diameter (nm)	PDI	Zeta Potential (mV)
Blank BCN	312 ± 15	0.184 ± 0.018	-0.127 ± 0.0935
MBCN	330 ± 36	0.233 ± 0.023	-1.69 ± 0.01323
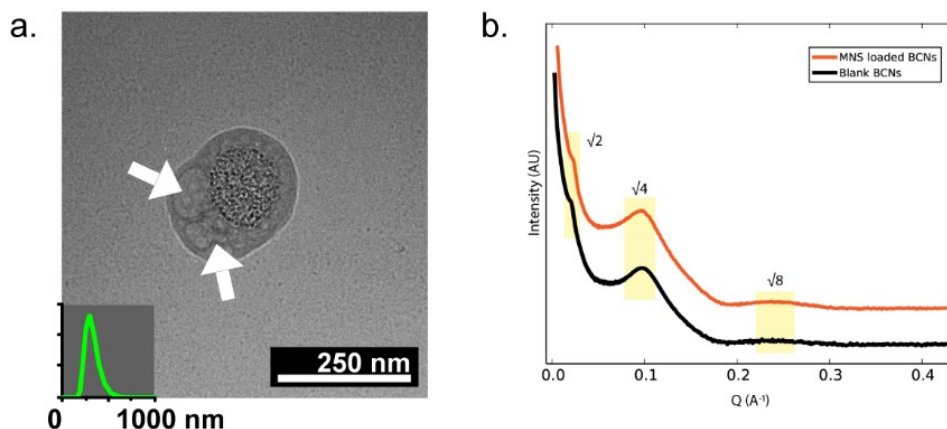
Figure 2-2. Cryo-TEM and SAXS analysis of MBCNs. (a) Representative cryogenic TEM image and overlaid DLS number distribution of MBCNs. White arrows indicate aqueous channels inside MBCNs. Scale bar represents 250 nm. (b) SAXS data for MBCNs (red) and non-MNS loaded BCNs (black) with labeled Bragg peaks indicating cubic internal structure.

Loading of the 4 nm oleic acid-functionalized MNS within PEG-*b*-PPS micelles (MCs) and polymersomes (PSs) was also successfully demonstrated via FNP to form MMCs and MPSs, respectively. Self-assembly of MMCs and MPSs was characterized via cryo-TEM and DLS (Figure 2-3). For MMCs (Figure 2-3a), the MNS were encapsulated within the hydrophobic core of micelles, with each micelle containing multiple individual MNS. Interestingly for MPSs (Figure 2-3b), the hydrophobic MNS did not appear to load within the bilayer membrane in the hydrophobic domain, but instead were aggregated within the aqueous core of the vesicular polymersomes. This loading pattern of the MNS into the BCNs, MC, and PS suggests a possible self-assembly mechanism of these complex structures. During FNP, the hydrophobic MNS likely rapidly precipitate and aggregate together under supersaturated conditions induced by the mixing of the organic and aqueous solvents. These MNS clusters may thus serve as nucleation points for subsequent assembly of the surrounding sulfur-rich PEG-*b*-PPS polymer into the final MC, PS, or

BCN structure. This nucleation mechanism has been proposed to explain the self-assembly of block copolymers around hydrophobic drug cores during standard FNP fabrication of micelles loaded with small molecule therapeutics[123].
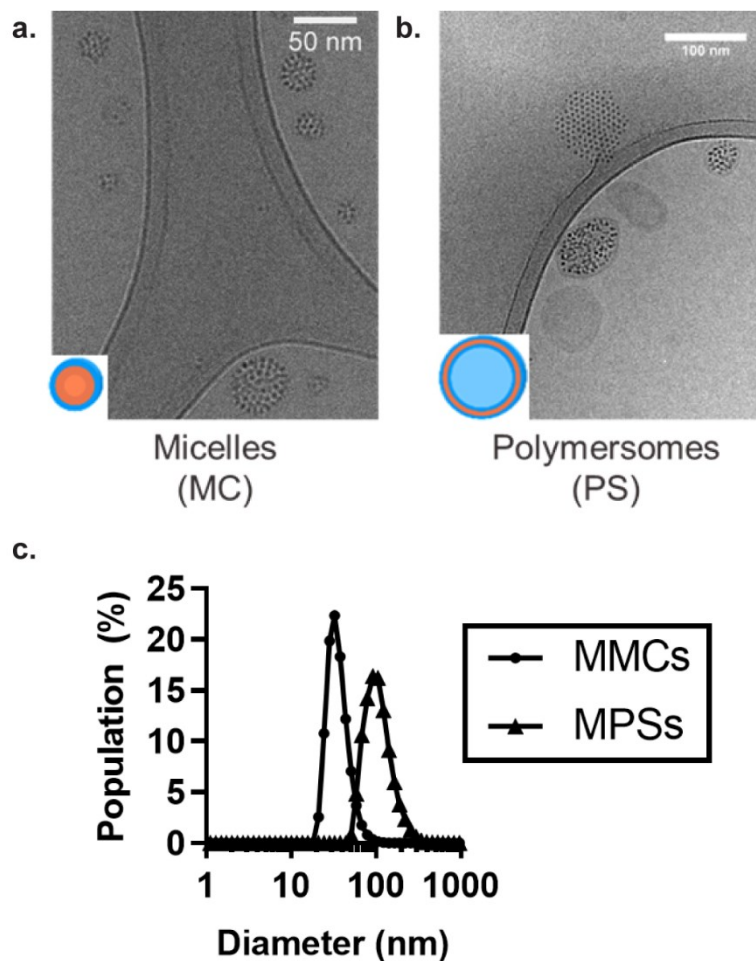
Figure 2-3. Cryo-TEM and DLS analysis of MMCs and MPSs. Representative cryogenic TEM image of a) MMCs and b) MPSs. c) DLS size characterization of MMCs and MPSs.

Table 2-2. Approaches for encapsulation of MNS within PEG-*b*-PPS nanocarriers. FNP = flash nanoprecipitation. TFH = thin-film hydration. CS = cosolvent evaporation. DH = direct hydration. DE = double emulsion.

PEG-*b*-PPS Polymer	Intended Morphology	Self-assembly Method	MNS functionalization	MNS diameter	Successful MNS encapsulation?	Notes
PEG$_{17}$-*b*-PPS$_{75}$	**BCN**	**FNP**	**Oleic acid**	**4 nm**	**Yes**	-
PEG$_{17}$-*b*-PPS$_{33}$	**PS**	**FNP**	**Oleic acid**	**4 nm**	**Yes**	**Inefficient**
PEG$_{17}$-*b*-PPS$_{33}$	PS	TFH	Oleic acid	4 nm	No	No rehydration of MNS and polymer film
PEG$_{17}$-*b*-PPS$_{33}$	PS	CS	Oleic acid	4 nm	No	MNS stuck to magnet
PEG$_{17}$-*b*-PPS$_{33}$	PS	DH	Oleic acid	4 nm	No	MNS stuck to magnet
PEG$_{17}$-*b*-PPS$_{33}$	PS	DE	Oleic acid	4 nm	No	No MNS encapsulation observed
PEG$_{45}$-*b*-PPS$_{20}$	**MC**	**FNP**	**Oleic acid**	**4 nm**	**Yes**	-
PEG$_{45}$-*b*-PPS$_{20}$	MC	TFH	Oleic acid	4 nm	No	No rehydration of MNS and polymer film
PEG$_{45}$-*b*-PPS$_{20}$	MC	FNP	Oleic acid	8 nm	No	MNS crashed out of solution
PEG$_{17}$-*b*-PPS$_{75}$	PS	FNP	Oleic acid	8 nm	No	MNS crashed out of solution
PEG$_{17}$-*b*-PPS$_{33}$	BCN	FNP	Oleic acid	8 nm	No	MNS crashed out of solution
PEG$_{17}$-*b*-PPS$_{33}$	PS	FNP	Citrate	8 nm	No	No MNS encapsulation observed

Other self-assembly methods besides FNP were also investigated for the encapsulation of the MNS within PEG-*b*-PPS nanocarriers, but were unable to successfully form MNS-encapsulated nanocarriers (Table 2-2). These methods included thin-film hydration (TFH), co-solvent evaporation (CS), direct hydration (DH)[124], and double emulsion (DE). In the TFH method, a thin film of PEG-*b*-PPS MC or PS polymer and the oleic acid-functionalized MNS was formed on the walls of a scintillation vial and was attempted to be rehydrated with 1 mL of 1X phosphate-buffered saline (PBS). However, the PBS was unable to solubilize the MNS off of the vial walls and form any nanocarriers even after aggressive agitation, likely due to their very hydrophobic nature (Figure 2-4a). On the other hand, CS and DH methods required the use of a magnetic stir bar and resulted in the MNS immediately sticking to the stir bar before successful nanocarrier self-
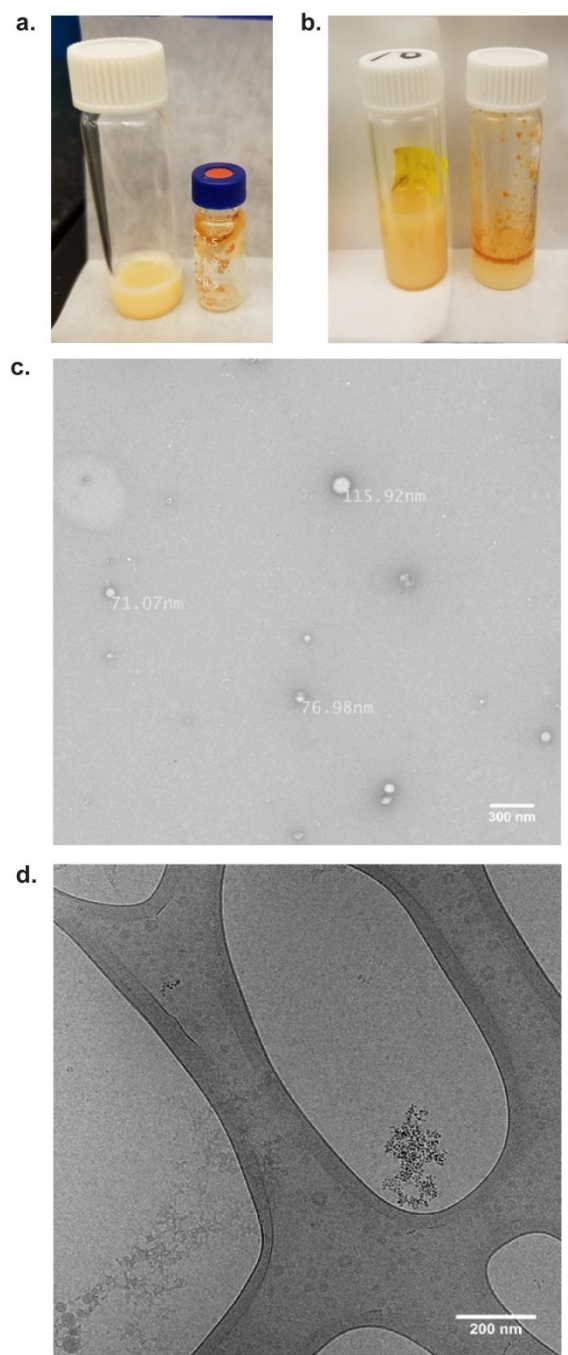
Figure 2-4. Images of failed formulations of MNS-encapsulated PEG-*b*-PPS nanocarriers. Attempted encapsulation of a) 4 nm oleic acid-functionalized MNS within PS via TFH, b) 8 nm oleic acid-functionalized MNS within PS via FNP, c) 4 nm oleic acid-functionalized MNS within PS via the DE method, and d) 8 nm citrate-functionalized MNS within PEG-*b*-PPS polymersomes via FNP. Numbers next to individual structures indicate nanocarrier diameter measured via Gatan Digital Micrograph software.

assembly and encapsulation could occur. In the case of the DE assembly method, PEG-*b*-PPS polymer appeared to form spherical structures in the 70-115 nm range (Figure 2-4c), though these nanocarriers were all empty and did not have any encapsulated MNS.

The effect of MNS diameter on their encapsulation within PEG-*b*-PPS nanocarriers was also studied. Specifically, 8 nm oleic acid-functionalized MNS were used as compared with the previously discussed 4 nm MNS. However, these larger MNS were unable to be encapsulated in either MC, PS, or BCNs (Table 2-2), as they either aggregated and settled immediately out of solution or onto the vial walls (representative image of attempted encapsulation in PS in Figure 2-4b). These formulations were not taken forward for further analysis. Failure of encapsulation of the 8 nm MNS was surprising in the case of MC, which have a hydrophobic core and were able to encapsulate multiple 4 nm oleic acid-functionalized MNS (Figure 2-3a). However, for (i) BCNs which have bilayer membranes with a hydrophobic domain of around 10 nm as seen via cryo-TEM, and for (ii) PS which were unable to contain even the 4 nm MNS within their bilayer membranes, the inability to encapsulate the larger 8 nm MNS was more expected given these spatial constraints.

Finally, the ability of PEG-*b*-PPS nanocarriers to encapsulate hydrophilic citrate-functionalized 8 nm MNS was also studied via the FNP method. For these hydrophilic MNS, only PS were studied given their aqueous core, which theoretically should accommodate hydrophilic cargo[38, 122]. However, the hydrophilic MNS were unable to be successfully encapsulated within PS, with only empty vesicles observed upon cryo-TEM analysis (Figure 2-4d). Interestingly, the resulting empty vesicles were much smaller than traditional PS.

Given these results, only FNP-formed MMCs, MPSs, and MBCNs were characterized further. These findings further support the utility of FNP over other self-assembly methods, demonstrating that it is a versatile method of stable nanocarrier assembly for efficient encapsulation of metal ferrite MNS with PEG-*b*-PPS nanocarriers.

2.3.2. **Structural Characterization via Elemental Analysis**

To further investigate the structure of the MBCNs, high angle annular dark field (HAADF) scanning transmission electron microscopy (STEM) along with energy-dispersive X-ray spectroscopy (EDS) was performed (Figure 2-5). Due to the high atomic number of the MNS, they can be seen as a bright dense inner core within the overall MBCN structure in the HAADF image (Figure 2-5c), which is consistent with the cryo-TEM images. Using EDS, the MNS distribution and loading within MBCNs were explicitly confirmed. The sulfur signal (green, Figure 2-5a) from the PPS backbone of the BCN polymer and the iron signal (red, Figure 2-5b) on the EDS maps shows clear overlap (merged image in Figure 2-5d) and verifies the direct association of the polymer with the iron oxide. Of note, the MNS were not evenly distributed throughout the BCN in an isotropic manner and appear as a dense cluster within the BCN interior. A line scan through the iron aggregate (Figure 2-5e and f) revealed an expected increase in the iron signal within the dense MNS core. The peak of the sulfur signal was also found in this dense MNS core, indicating an increase in the amount of polymer around the MNS, which is suggestive of a dense polymer aggregate as opposed to the highly organized and porous cubic domains within the surrounding BCN architecture.
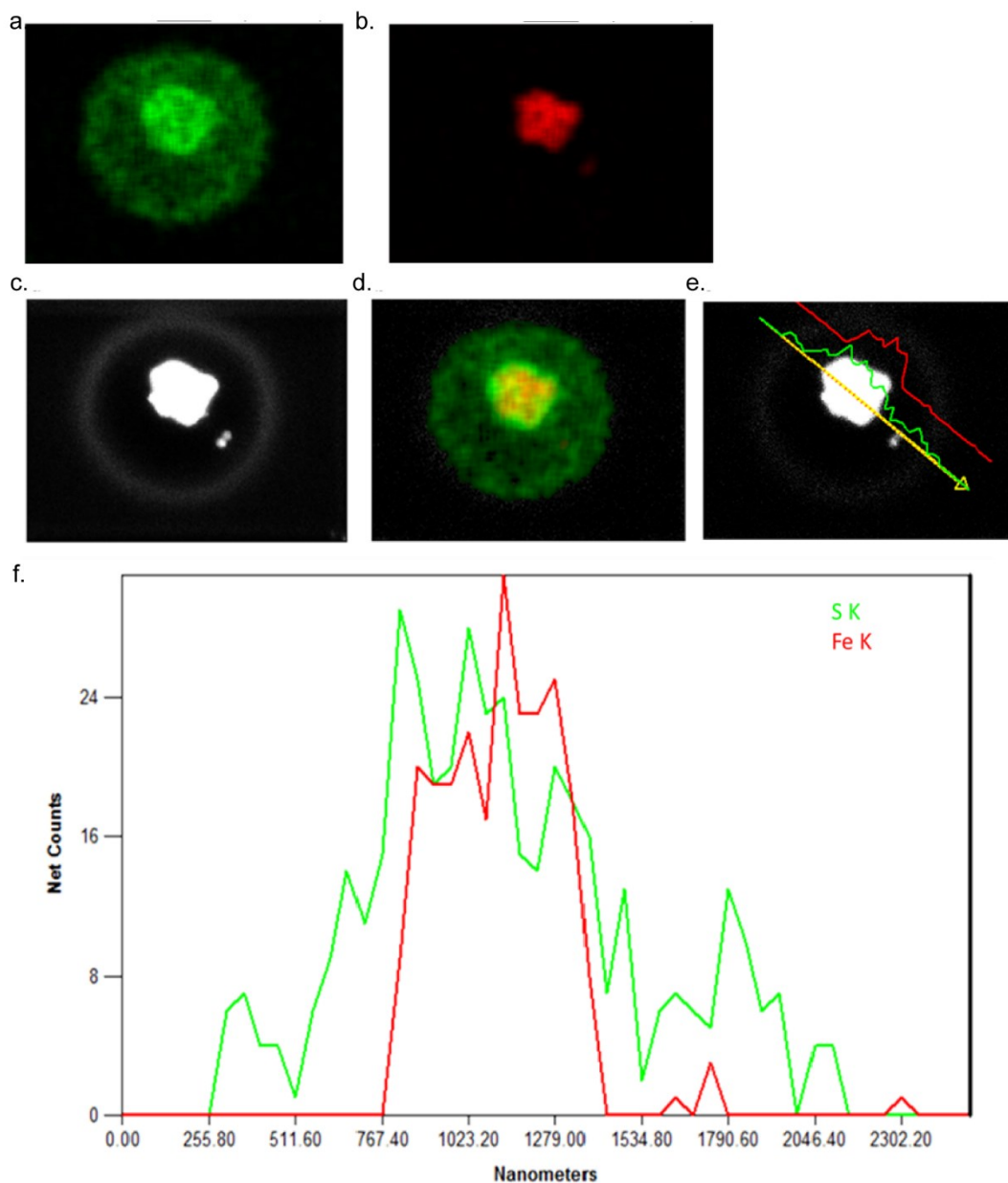
Figure 2-5. STEM-EDS of MBCNs. Representative STEM image of a MBCN with subsequent EDS mapping of the sulfur (a) and iron (b) distribution within the nanocarrier. c) Corresponding dark field image of the representative MBCN, demonstrating high contrast MNS loaded in the center of the nanocarrier. d) Overlay of iron and sulfur EDS signal of MBCNs. Line scan (e) and corresponding sulfur (green) and iron (red) EDS counts (f) across a MBCN particle.

Interestingly, as more MNS were loaded per mg of PEG-*b*-PPS polymer, they formed increasingly large clusters within the larger cubic MBCN structure (Figure 2-6). This observation further supports the hypothesis about the self-assembly mechanism of these nanocarriers starting with initial aggregates of the MNS serving as nucleation points for nanocarrier assembly during FNP. In this case, more MNS present during the FNP process are likely leading to larger initial nucleation points for subsequent PEG-*b*-PPS polymer assembly into the final MBCN morphology.
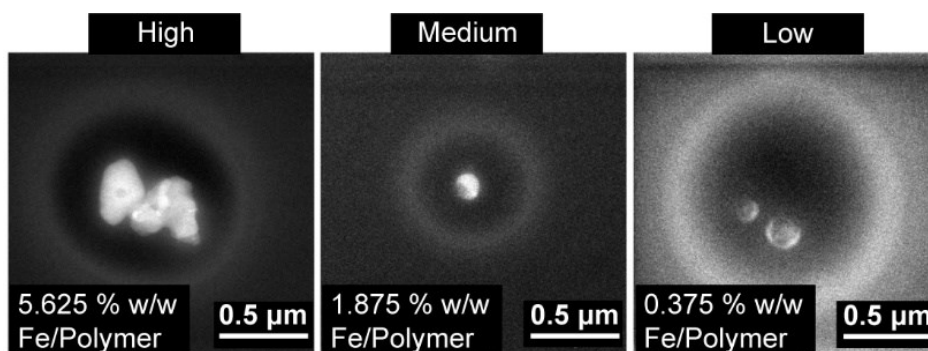
Figure 2-6. HAADF imaging of MBCNs. HAADF images of MBCNs with differing levels of MNS loading (High, Medium, Low). Brighter contrast denotes an abundance of iron, a high atomic weight element.

2.3.3. Loading of Small Molecule and Nanoscale Cargo

While we have previously demonstrated the efficient encapsulation of hydrophobic and hydrophilic small molecules and proteins within BCNs[39, 41], in this work we have quantified for the first time the ability of BCNs to load nanoscale cargo via FNP, namely 4 nm MNS. Inductively coupled plasma mass spectrometry (ICP-MS) analysis showed that BCNs could encapsulate MNS with over 95% efficiency (Figure 2-7). This high MNS loading within BCNs via FNP did not impede additional loading of both lipophilic and hydrophilic cargo.
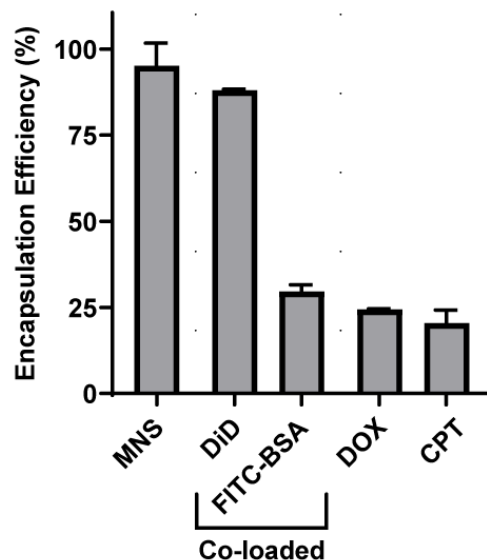
Figure 2-7. MBCN cargo encapsulation efficiency. Encapsulation efficiency of nanoscale and small molecule cargo within MBCNs. Error bars = S.D.

Specifically, loading of the model lipophilic dye 1,1'-dioctadecyl-3,3,3',3'-tetramethylindodicarbocyanine, 4-chlorobenzenesulfonate (DiD) and model hydrophilic protein fluorescein isothiocyanate-tagged bovine serum albumin (FITC-BSA) into MBCNs was found to be 80% and 28%, respectively. This result is consistent with our previous reports suggesting the partitioning of hydrophobic cargo into the hydrophobic bilayer region and hydrophilic cargo into aqueous channels of the MBCNs during the self-assembly process[39]. To assess the utility of this process for future theranostic applications, MBCNs were loaded with anti-cancer therapeutic cargoes including doxorubicin (DOX) and camptothecin (CPT) (Figure 2-7). Interestingly, in all cases where hydrophilic cargo like FITC-BSA and doxorubicin, and hydrophobic cargo like DiD and camptothecin were loaded within MBCNs, MNS loading efficiency remained unchanged. This high capacity for loading multiple therapeutic cargos, particularly hydrophilic cargo, is due to the

intertwined PEG-*b*-PPS bilayer membranes that form aqueous channels throughout the nanocarrier, within which hydrophilic cargo are entrapped in a size-dependent manner[39, 41].

MMCs and MPSs showed an MNS encapsulation efficiency of 71% and 12%, respectively, which is lower as compared to BCNs (Table 2-3). These variances in loading are likely due to differences in internal hydrophobic surface area of these 3 morphologies. PEG-*b*-PPS BCNs possess the highest internal hydrophobic surface area and subsequent MNS encapsulation efficiency; followed next by micelles, which have space for encapsulation of the MNS within their small hydrophobic core; and then vesicular polymersomes. PS theoretically should accommodate hydrophobic cargo only within the hydrophobic domain of their single bilayer membranes, though in this case were found to load the 4 nm oleic acid-functionalized MNS in an "all-or-nothing" manner, with some PS containing several MNS while other PS were empty (Figure 2-3b). This finding is further evidence of the nucleation-based hypothesis of how these MNS-encapsulated nanocarriers are assembling during FNP.

These results thereby prove the superiority of BCNs over MCs and PSs in loading MNS, and further demonstrate the potential usage of MBCNs as theranostic nanocarriers. Considering this, the MBCNs were investigated further for theranostic applications.

Table 2-3. Encapsulation efficiency of MNS within MMCs and MPSs. Encapsulation efficiency of MNS into PEG-*b*-PPS micelles and polymersomes, determined using ICP-MS.

	MMCs	MPSs
MNS Encapsulation Efficiency (%)	70.5 ± 9.7	11.9 ± 7.2

2.3.4.   Relaxivity Measurements

Due to their small size (sub-20 nm), MNS are superparamagnetic and have the potential to enhance r_2 relaxivity[25, 93] which is a quantitative measure of the sensitivity and contrast enhancement of material for T2 MRI imaging. The r_2 relaxivity of the MBCNs was measured at 1.4 and 7 T (Figure 2-8a and b, respectively). Remarkably, r_2 relaxivity of MBCNs (182 mM^{-1}*s^{-1}) was found to be higher than that of 4 nm water-soluble, citrate-coated MNS (74 mM^{-1}*s^{-1}) and the current clinical T2 contrast agent Ferumoxytol (62.3 mM^{-1}*s^{-1})[125]. This enhancement in relaxivity is likely due to clustering effects of the MNS within BCNs[106, 110, 126]. Dense clusters of magnetic nanoparticles have been found to generate a larger magnetic moment per a given volume than individual particles[127, 128]. The resulting stronger influence on the water surrounding this cluster leads to a larger effect on proton relaxation, resulting in higher relaxivity. MBCN r_2 relaxivity also increased with increasing MNS-loading, up to 174 mM^{-1}*s^{-1} for MBCNs loaded with 1.25% MNS by weight. This observation is also likely due to clustering effects, supported by our earlier observations that the loaded MNS form increasingly large clusters within the overall MBCN nanocarrier (Figure 2-6). Notably, this trend of MBCN r_2 relaxivity improvement with increased MNS-encapsulation was seen at two distinct clinically relevant field strengths (1.4 T and 7 T), suggesting a synergistic effect of MNS clustering within MBCNs on relaxivity, as previously reported in other MNS-based nanoconstruct systems[110, 126]. Interestingly, additional loading of MNS past 1.25% by weight into BCNs did not lead to a significant change in relaxivity. Subsequent *in vitro* and *in vivo* studies were thus performed with 1.25% MBCNs.

Since enhancement in relaxivity is due to the ability of the MNS to affect reduce relaxation times of surrounding water protons[129], the high degree of relaxivity observed for MBCNs indicate

high access of MNS to water molecules while loaded within BCNs. If the clustered MNS did not have adequate water access within the center of the MBCNs, the r_2 relaxivity would have decreased upon MNS encapsulation. Instead, the r_2 relaxivity increased, indicating continued access to water and enhancement due to clustering. Thus, these data importantly demonstrate not only efficient encapsulation of MNS within MBCNs, but also the persistence of the characteristic aqueous channels within the MBCNs, even with internal loading of a nanoscale cargo.
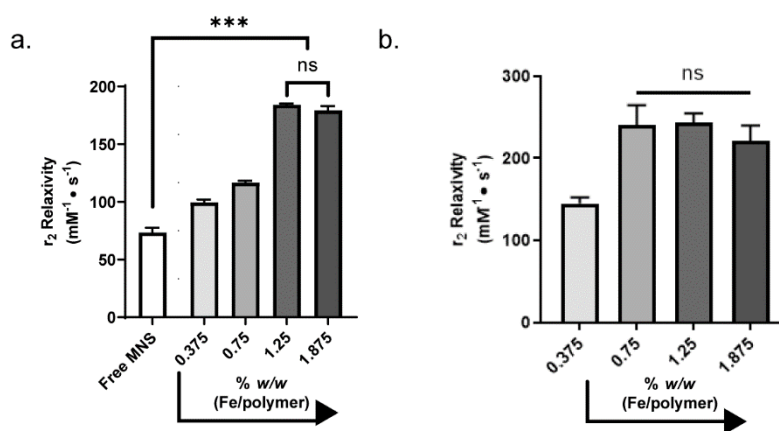
Figure 2-8. MBCN Relaxivity. Relaxivity (r_2) measurements at a) 1.4 T and b) 7 T of MBCNs with increasing amounts of MNS loaded per mg of PEG-*b*-PPS copolymer as compared with hydrophilic, citrate-coated 4 nm free MNS. Error bars = S.D., significance determined via Dunnett's multiple comparisons test, *** $p < 0.001$.

2.3.5.   Stability Characterization

Considering the therapeutic applications of nanocarriers, an important parameter to analyze for any new nanocarrier system is its colloidal stability over time on the benchtop and in the presence of serum proteins. Such studies give insight into the longevity and the performance of a system in biological environments. We investigated the room-temperature stability of MBCN formulations over 6 months. Using DLS, no significant decreases or increases in size were observed at 1, 3, and 6 months compared to the initial size measurement after MBCN assembly

(Figure 2-9a, black line). Additionally, the iron content of the MBCNs (Figure 2-9a, red line) remained consistent over these 6 months as measured by ICP-MS, indicating stable encapsulation of the MNS over time within the MBCNs. Potential escape of the encapsulated MNS is expected to lead to their immediate aggregation given their hydrophobic nature, which would be reflected as a change in the measured nanocarrier diameter or the measured MNS weight percent. As neither of these measures changed significantly, these results confirm the stability of the MBCN morphology over 6 months.

The stability of MBCNs in fetal bovine serum (FBS) was also investigated. MBCNs were found to be stable in serum up to 24 h (Figure 2-9b) based on their size, with minimal change in Fe content indicating minimal MNS leaching out of the MBCNs (Figure 2-9c). The ideal performance of the MBCNs in this *in vitro* study is suggestive of continued stability and performance in the systemic circulation.
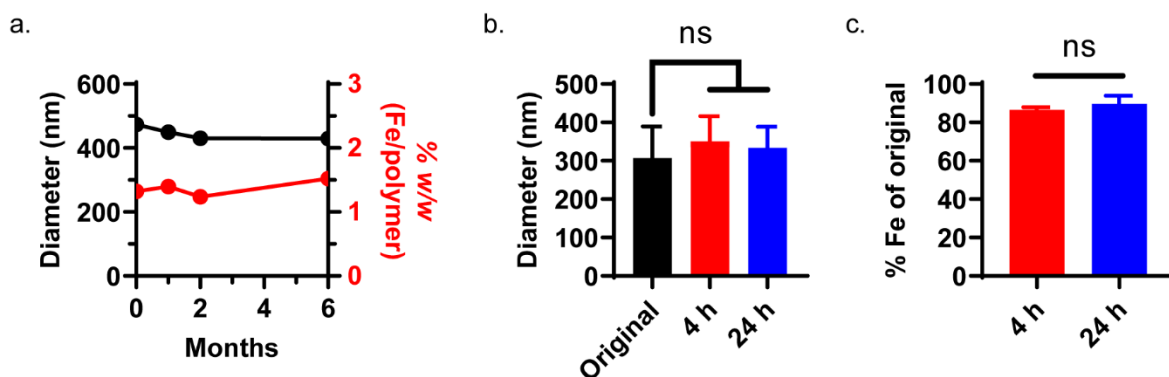
Figure 2-9. Benchtop and serum stability of MBCNs. Benchtop and serum stability of MBCNs over time. (a) Hydrodynamic diameter (black) and encapsulated MNS weight % (red) of MBCNs over a period of 6 months. (b) Diameter and (c) percentage of iron retained in the MBCNs over time in the presence of serum proteins. Error bars = S.D., n = 3, significance determined via Dunnett's multiple comparisons test, *** $p < 0.001$.

2.3.6. Organ-level Biodistribution of MBCNs

We have previously examined the organ-level biodistribution of BCNs in mice and demonstrated that they accumulate differentially in organs, with high uptake into the spleen[41]. We similarly aimed to determine the biodistribution of MBCNs upon intravenous (IV) administration in comparison with water-soluble, citrate-functionalized MNS. The presence of the MNS within MBCNs allows them to be tracked via ICP-MS, providing a more quantitative and highly sensitive detection method of assessing their organ-level uptake than previously demonstrated for PEG-*b*-PPS nanocarriers alone. As an orthogonal method of tracking these nanocarriers, indocyanine green (ICG) was loaded into MBCNs to investigate their uptake via NIR fluorescence. MBCNs were found to have high accumulation in the spleen followed by the liver, as determined by both IVIS (Intravital Imaging System) and ICP-MS over 7 days post IV injection (Figure 2-10). This high accumulation in the spleen for MBCNs is consistent with our prior biodistribution studies with non-MNS-loaded BCNs[41]. Given the strong influence of nanoparticle structure and chemistry on biodistribution[117], these results suggest that the presence of MNS within the BCNs does not significantly alter BCN physicochemical parameters *in vivo*. Additionally, the close correlation between the quantified IVIS signal (Figure 2-10b) and ICP-MS signal (Figure 2-10c) in organs indicate dual delivery of the MNS and ICG, signifying delivery of MBCNs with intact payloads and supporting the stability of these nanocarriers *in vivo* over 7 days. There are also key differences between the organ-level biodistribution of MBCNs and free, hydrophilic MNS with a 4 nm metallic core and citrate shell (Table 2-4). Free MNS had higher uptake than MBCNs into the liver at all 3 timepoints (Figure 2-10d), with no significant uptake in the other 5 organs that were

analyzed. This observation is consistent with other biodistribution analyses of hydrophilic surface-modified iron oxide MNS[130-132].

Given the retention of MBCNs within mice for up to 7 days, we additionally assessed liver and kidney function of mice from the 7-day timepoint via estimation of alanine aminotransferase (ALT) and creatinine serum levels (Figure 2-11), respectively, and found both to be within normal ranges[133, 134]. This analysis is consistent with our previous studies in mice and non-human primates demonstrating that PEG-*b*-PPS nanostructures are non-toxic at relevant diagnostic and therapeutic concentrations[118].

Thus, these *in vivo* biodistribution results demonstrate the potential of MBCNs as unique delivery vehicles for both molecular and nanoscale payloads *in vivo* for up to 7 days. The organ-level biodistribution of MBCNs suggests that, like non-magnetic BCNs, they may be useful for immunotheranostic[135] strategies due to their high splenic uptake and the key role of the spleen in immune cell activation.

Figure 2-10. *In vivo* **biodistribution of MBCNs after IV administration**. *In vivo* biodistribution of MBCNs after IV administration. (a) Representative IVIS images for mouse livers and spleens harvested 4 h, 24 h, or 7 d post IV injection of PBS or MBCNs. (b) Quantification of radiant efficiency of the MBCN fluorescent signal in livers and spleens at 4 h, 24 h, and 7 days post IV injection. ICP-MS analysis of organs of mice treated with (c) MBCNs or (d) water-soluble, hydrophilic citrate-coated MNS at 4 h, 24 h, and 7 days post IV injection. Error bars = S.D., significance determined via Dunnett's multiple comparisons test, * $p < 0.033$, ** $p < 0.002$, and *** $p < 0.001$.

Table 2-4. Hydrophilic MNS physicochemical characterization. Hydrodynamic diameter and zeta potential of hydrophilic MNS used as controls in organ-level biodistribution assessment.

	Diameter (nm)	Zeta potential (mV)
4 nm metallic core, citrate-coated MNS	18 +/- 2 nm	-20 +/- 2 mV
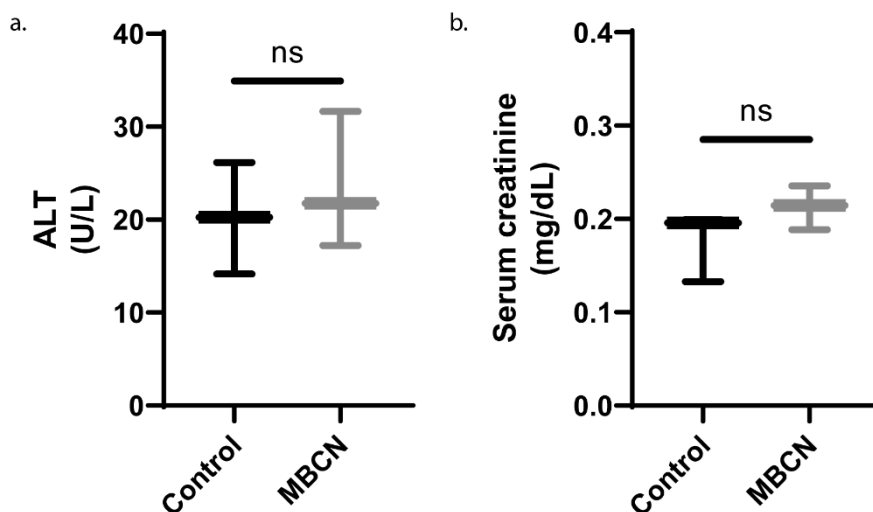
Figure 2-11. Liver and kidney toxicity of MBCNs. Serum a) ALT and b) creatinine values of MBCN- or control-treated mice, 7 days post-injection. Error bars = S.D., n = 3, significance determined via Student's t-test.

2.3.7. *Ex vivo* MRI Contrast Enhancement of MBCNs

Given the high delivery of MNS to the liver via the MBCNs (Figure 2-10), I next wanted to assess the effect of this on T2 contrast enhancement via *ex vivo* MRI analysis of excised livers following MBCN treatment. Briefly, mice were injected with either PBS, MBCNs, or free 4 nm citrate-functionalized MNS as in the previous biodistribution study. The iron concentration of the MBCN and MNS treatments were matched for this study. After 24 h, mouse livers were excised and T2-weighted images were taken and used to generate T2 color-coded maps. The results from two independent studies are shown in Figure 2-12 (T2 images and maps) and Table 2-5 (T2 times).

For T2-weighted imaging, negative contrast agents like the MNS should generate a decrease in T2 times and a darkening of the signal in regions where they accumulate. This can be seen in Figure 2-12 in both studies, where the livers from MNS-treated mice appear darker on all images than the PBS-treated mouse livers and have a correspondingly low T2 time (Table 2-5). However, the MBCN-treated mouse organs did not have much obvious negative contrast enhancement, appearing marginally darker than the PBS-treated mouse livers but not as dark as the MNS-treated mouse livers. Their corresponding T2 times were also in between those of the PBS- and MNS-treated mouse livers.

These findings are unexpected, considering the higher solution-based r_2 relaxivity of the MBCNs as compared with the free MNS (Figure 2-8). In this case, the MBCNs and MNS are in a more complex biologic environment, as opposed to simply being in solution, so encapsulation within the BCN structure may minimize the MNS interaction with water molecules when in a biologic environment. Perhaps the MBCNs are being physically compressed in some way that disrupts their aqueous channels, or perhaps by the 24 h timepoint they are being processed by liver cells in a way that affects their structure and subsequent relaxation of nearby water molecules. However, this latter possibility is less likely given the retained ICG signal of the MBCNs at the 24 h timepoint, which suggests presence of intact MBCNs (Figure 2-10b). Further studies with the MBCNs are needed to explore their MRI contrast enhancement in biologic environments and to better understand this discrepancy in T2 shortening compared with the free MNS. Therefore, these *ex vivo* MRI results suggest that the utility of the MBCNs for T2-weighted imaging is limited, given that they had only a moderate effect on T2 shortening and negative contrast enhancement as compared with free citrate-functionalized MNS.
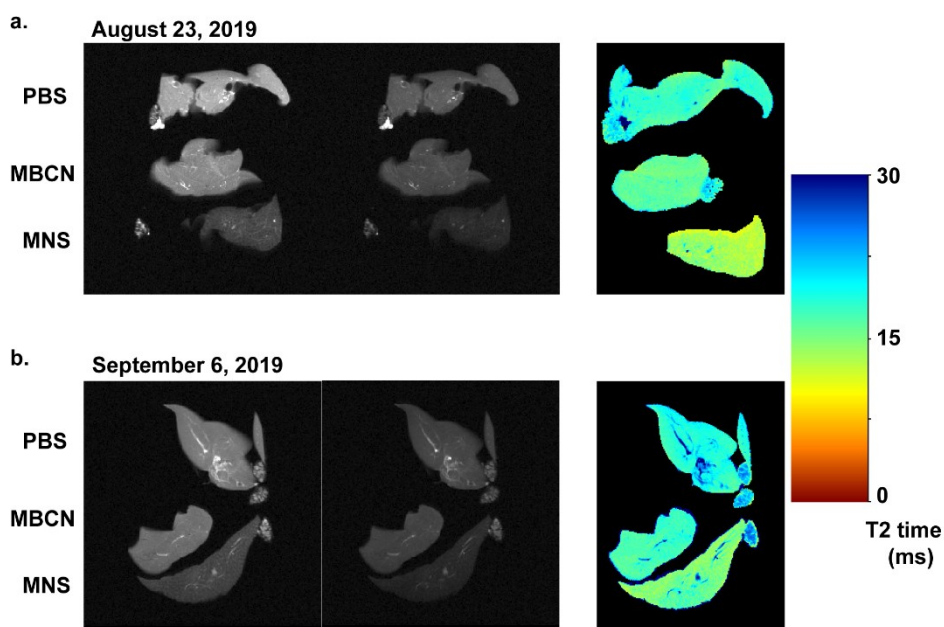
Figure 2-12. *Ex vivo* **imaging of MBCNs.** T2-weighted images and color-coded maps of excised livers from mice treated with PBS, MBCNs, or free hydrophilic MNS over 2 different experiments.

Table 2-5. T2 times from MBCN *ex vivo* **imaging.** T2 times of excised livers from mice treated with PBS, MBCNs, or free hydrophilic MNS over 2 different experiments.

Group	8/23/2019 T2 time (ms)	9/6/2019 T2 time (ms)
PBS	17.46	19.22
MBCNs	16.36	17.63
MNS	14.29	15.76

2.3.8. Intracellular Cargo Delivery and Cytotoxicity Analysis of MBCNs

A unique benefit of MBCNs is their ability to co-load diverse therapeutic payloads; therefore, it is crucial to assess whether these payloads can be effectively delivered intracellularly. Cell uptake of MBCNs and delivery of therapeutic payloads from MBCNs was therefore investigated in MCF7 breast cancer cells. MBCNs dual-loaded with FITC-BSA and DiD were incubated with MCF7 cells for 4 h, and the uptake was analyzed using confocal microscopy and flow cytometry. Previously, we have shown that BCNs (non-MNS-loaded) are taken up into endolysosomes of cells[39] following phagocytosis by RAW 264.7 macrophages. Here we have observed similar uptake of MBCNs by MCF7 cells, which have been shown to be phagocytic and to uptake nanoparticles between 250-375 nm[136, 137]. On confocal microscopy, punctae of both DiD (red) and FITC-BSA (green) signals were colocalized with lysosomal dye Lysotracker (blue) signal (Figure 2-13a). In addition, flow cytometric analysis showed a positive correlation for FITC-BSA and DiD cell uptake, indicating successful co-delivery of the small molecule payloads (Figure 2-13b).

To further characterize the delivery of MNS *via* MBCNs, STEM and EDS elemental mapping were performed on MCF7 cells following 4 h of MBCN treatment. The delivered MBCNs can be seen as high contrast features within vesicular structures in the cytoplasm (Figure 2-13c). EDS mapping of these regions confirms that these high contrast features are composed of iron (Figure 2-13d). This technique may serve as an alternative and reliable method to precisely track cellular loading of complex nanocarriers like BCNs, whose analysis with conventional fluorescent-based techniques involve several optimization steps and interference from cellular components. Together, the confocal microscopy images of endosomal DiD and FITC-BSA along with the EDS

mapping of endosomal MNS indicate successful multi-intracellular delivery of all MBCN payloads simultaneously. ICP-MS was used to more quantitatively determine uptake of the MNS payload via analysis of the iron amount per cell following incubation with MBCNs. Notably, MNS delivery was found to be tunable, with more iron delivery to cells after treatment with higher MNS weight % MBCNs (Figure 2-13e). The baseline iron content of cells is indicated in red. MBCNs were furthermore found to be non-cytotoxic (Figure 2-14), similar to other PEG-*b*-PPS nanostructures that have been used extensively for drug delivery applications. The *in vivo* and *in vitro* results here, along with previous studies validating the non-immunogenicity of PEG-*b*-PPS BCNs [39], indicate their potential as nanocarriers for future drug delivery applications.
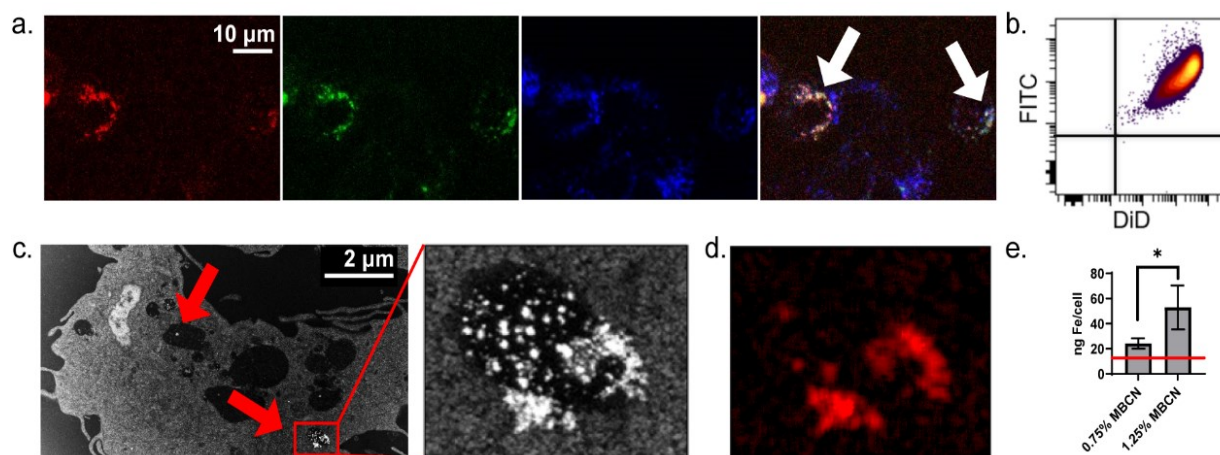
Figure 2-13. Intracellular delivery of multiple payloads by MBCNs. Intracellular delivery of multiple payloads by MBCNs. (a) Confocal images of MCF7 cells stained with lysosomal dye Lysotracker (blue) after 4 h incubation with MBCNs co-loaded with lipophilic dye DiD- (red) and hydrophilic dye FITC-BSA (green). White arrows in the merged image indicate examples of colocalized signal from DiD, FITC-BSA, and Lysotracker. (b) Flow cytometry analysis showing MCF7 cells are double positive for FITC and DiD following 4 h incubation with DiD + FITC-BSA loaded MBCNs. (c) STEM image of a single MCF7 cell with endosomal uptake of MBCNs (red arrows) and zoomed in image of red box. (d) EDS mapping of the iron signal of MBCNs within an endosomal compartment. (e) ICP-MS analysis of MNS delivery to MCF7 cells via two different MBCN formulations containing 0.75% or 1.25% Fe by weight. Error bars = S.D., significance determined via Dunnett's multiple comparisons test, * $p < 0.033$.
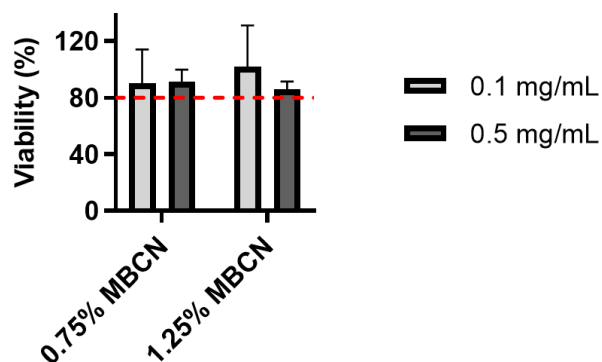
Figure 2-14. Cytotoxicity of MBCNs. at two different treatment concentrations (0.1 and 0.5 mg/mL PEG-*b*-PPS polymer). Red line indicates 80% viability. Error bars = S.D., N = 3.

2.3.9.   Assessment of MBCN Oxidation Responsiveness

An advantage of PEG-*b*-PPS copolymer for biomedical applications is its oxidation responsiveness. As the hydrophobic PPS block oxidizes, PEG-*b*-PPS transitions to the more hydrophilic derivatives of either PEG-*b*-poly(propylene sulfoxide) or PEG-*b*-poly(propylene sulfone)[116]. Due to this change in the hydrophilic mass fraction of the copolymer, the nanocarrier morphology transitions to a more thermodynamically stable structure. Previously, we have demonstrated that such a transition can be induced via photo-, chemical or biological oxidation, resulting in a stimuli-responsive transition from PEG-*b*-PPS FMs[37], PSs[42], and BCNs[40] into micelles. During cylinder-to-sphere transitions, small molecule hydrophobic payloads within filomicelles were retained within micelles at similar concentrations to allow slow release of drug-loaded nanocarriers from filamentous hydrogels[37].

We recently demonstrated that BCNs undergo similar transitions to micelles upon oxidation, allowing triggered endosomal escape of micelles loaded with small molecule

chemotherapeutics into the cell cytosol for on-demand cytotoxicity[40, 113]. We thus sought to determine whether BCNs loaded with MNS can undergo a similar oxidation-induced transition and retain these larger nanoscale payloads within the released micelles (Figure 2-15a). As we have previously performed when assessing oxidation-dependent PEG-*b*-PPS nanostructure transitions[37], a high concentration of H_2O_2 was selected to achieve an accelerated BCN degradation for the generation of sufficient concentrations of micelles for subsequent physicochemical characterization.

MBCNs were found to slowly transition into micellar nanocarriers upon oxidation (Figure 2-15b), as confirmed by TEM (Figure 2-15c). A nearly complete transition from BCNs to this smaller micellar population (37 ± 24 nm) was detected after 24 h (Figure 2-15d). This micellar population was separated via centrifugation and analyzed for the presence of encapsulated MNS using ICP-MS. If any oleic-acid functionalized MNS were to be released from the MBCNs in free form and not stabilized by polymer, they should aggregate and be removed by this centrifugation step. Therefore, any iron in the released micelles should be from MNS that are incorporated within the monodisperse population of micelle-sized structures. The separated, smaller population was found to contain MNS via ICP-MS, with almost 80% of the MNS being released in this micellar form after 24 h (Figure 2-15e). Interestingly, the MNS-loaded micelles that were released *via* oxidation of MBCNs (Figure 2-15f) were identical in size, structure and MNS density as MMCs that were formed directly using FNP using the same 4 nm MNS and PEG$_{45}$-*b*-PPS$_{44}$ polymer (Figure 2-15g), which is known to self-assemble micelles[117]. MBCNs are therefore stimuli-responsive as they transition into monodisperse MNS-loaded micelles upon oxidation. Furthermore, this oxidation-responsiveness suggests that MBCNs should be metabolized via

physiological oxidation over time, as observed with other PEG-*b*-PPS nanocarriers[37, 42]. This transition is driven by the change in interfacial tension that occurs as the PPS backbone of the PEG-*b*-PPS polymer oxidizes, which we have extensively modeled in previous studies[37]. While other vesicle to micelle transitions have been reported, to the best of our knowledge this is the first report of the transfer of a nanoscale payload from one nanocarrier morphology to another, as well as the first demonstration of *in situ* generation of MNS-loaded micelles. This capability may prove useful for sustained nanocarrier delivery or theranostic applications in the treatment of clinical conditions marked by high oxidative stress, such as cancer, atherosclerosis, and chronic kidney disease[138].
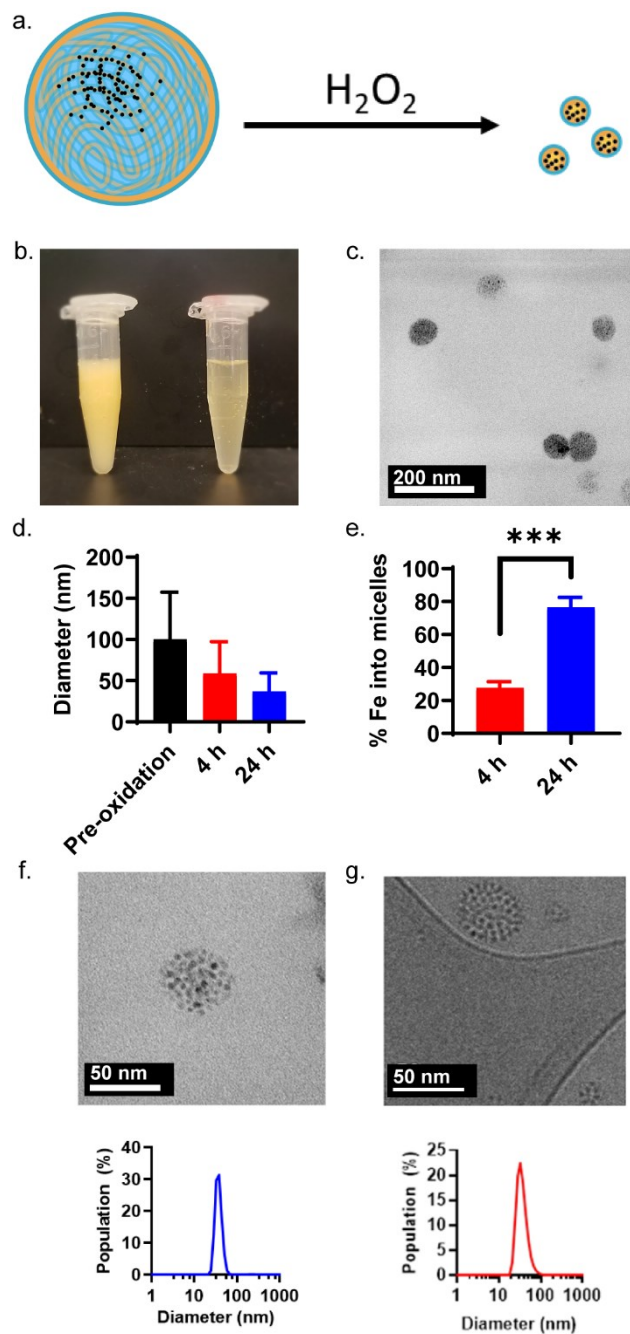
Figure 2-15. Oxidation-mediated morphological transition of MBCNs to MMCs. (a) Schematic representing MBCNs transition into micelles carrying MNS upon oxidation using H_2O_2. (b) Photographic images showing oxidative degradation of cloudy MBCNs (left tube) into translucent micellar nanocarriers (right tube) after H_2O_2 treatment. (c) TEM of the oxidized MBCNs. (d) Diameter of the MBCNs over time under oxidative conditions. (e) Percentage of iron carried over into micellar nanocarriers over 24 h upon oxidative degradation of MBCNs. Micelles released by MBCNs (f) were found to be identical in structure and size to MNS-loaded micelles that were directly formed by FNP (g) as assessed by TEM and DLS.

2.3.10.   Conclusions

Here, I have discussed the development and characterization of MNS-loaded polymeric bicontinuous nanospheres (MBCNs) with potential future applications in drug delivery and theranostics. MBCNs were successfully assembled via FNP and were able to encapsulate metal ferrite MNS with high encapsulation efficiency along with both hydrophobic and hydrophilic small molecules within their internal bilayer membranes and aqueous channels. MNS-encapsulated MCs and PSs were also successfully formed via FNP, though with lower encapsulation efficiency. The encapsulated MNS allowed the MBCNs to enhance r_2 relaxivity, as measured for samples in solution. MBCNs were able to successfully deliver their encapsulated small molecule and nanoscale payloads *in vitro* and *in vivo* and demonstrated high splenic uptake. However, despite their high r_2 relaxivity in solution and efficient *in vivo* delivery, the MBCNs did not notably enhance MRI contrast in *ex vivo* study in MBCN-treated mice, suggesting further optimization for diagnostic applications is needed. Finally, MBCNs demonstrated a morphological transition into MNS-loaded micelles under oxidative conditions, making them a versatile platform for future sustained delivery applications.

2.4.   Materials and Methods

2.4.1.   Synthesis of PEG-*b*-PPS Block Copolymer

PEG-*b*-PPS block copolymers were synthesized as described previously[38, 39]. Briefly, methyl-ether PEG was end-functionalized using methanesulfonyl chloride to give a mesylate leaving group. The product was then converted to PEG-thioacetate via reaction with thioacetic acid. The PEG-thioacetate was activated with the base to produce a thiolate anion to initiate ring-opening living polymerization of propylene sulfide. After 10 minutes of polymerization, the reaction was quenched by end-capping the block-copolymer with benzyl bromide. After 2 h of end-capping, the resulting block copolymer was precipitated in methanol and then stored under nitrogen at -20 °C. 1H NMR was used to confirm the degree of polymerization.

2.4.2.   Synthesis of $Zn_{0.2}Mn_{0.8}Fe_2O_4$ Magnetic Nanostructures

The $Zn_{0.2}Mn_{0.8}Fe_2O_4$ nanoparticles were synthesized using a well-known thermal decomposition method that resulted in monodispersity, single crystallinity, and controlled stoichiometric composition[26, 139]. For $Zn_{0.2}Mn_{0.8}Fe_2O_4$ nanoparticles synthesis, Fe(acac)3 (2 mmol), Mn(acac)2 (0.8 mmol), Zn(acac)2 (0.2 mmol), 1,2-hexadecanediol (10 mmol), oleic acid (6 mmol), oleylamine (6 mmol), and phenyl ether (20 mL) were charged in a 100 mL three-neck round-bottom flask and magnetically stirred under a flow of nitrogen. The mixture was first heated to 110 °C for 1 h to remove moisture and then refluxed for 1h before cooling down to room temperature. The black-brown mixture was precipitated, washed with ethanol, and was then dispersed in hexane.

To make hydrophilic MNS, the as-synthesized oleic acid coated hydrophobic $Zn_{0.2}Mn_{0.8}Fe_2O_4$ nanoparticles were functionalized with citrate via a ligand-exchange process

[140]. A chloroform dispersion (2 mL) of $Zn_{0.2}Mn_{0.8}Fe_2O_4$ nanoparticles (12.5 mg) and a dimethyl sulfoxide (DMSO) solution of citric acid (1 mL, 31.25 mg) were mixed and sonicated overnight at room temperature. The modified $Zn_{0.2}Mn_{0.8}Fe_2O_4$ nanoparticles were washed with dichloromethane three times, dried under nitrogen gas, and finally dispersed in water. The dispersion was dialyzed to remove any residual surfactants using a dialysis bag (MWCO = 10000) for 2 days in water. A 200 nm syringe filter was used to remove any precipitation, and the final concentration of citrate-functionalized $Zn_{0.2}Mn_{0.8}Fe_2O_4$ nanoparticles dispersed in water was determined by inductively coupled plasma mass spectrometry (ICP-MS) analysis.

### 2.4.3.	PEG-*b*-PPS Nanostructure Assembly and Cargo Loading

PEG-*b*-PPS MCs, PS, or BCNs were assembled and loaded with hydrophobic MNS using the flash-nanoprecipitation (FNP) method as described previously using a confined impingement jet (CIJ) mixer[38, 39]. Briefly, PEG-*b*-PPS polymer (10 or 20 mg) and oleic acid-functionalized MNS (6 to 120 ug) were dissolved in 500 μL of tetrahydrofuran (THF). This solution was then loaded into a 1 mL disposable syringe. A second syringe was loaded with 500 μL of Milli-Q water for BCNs or 1X PBS for MCs and PSs. These organic and aqueous phases then impinged within the CIJ mixer into a 1 mL reservoir of Milli-Q water for BCNs and 1X PBS for MCs and PSs. Loading of other hydrophobic or hydrophilic agents into these particles was done by adding hydrophobic agents into the THF phase and hydrophilic agents into the aqueous phase prior to impingement. Unloaded agents and THF were removed using a Sepharose LH-20 size exclusion column with a 1x PBS mobile phase. The loading efficiency of small molecules was determined by fluorescence measurements at the following wavelength (excitation (nm)/emission (nm)): FITC-BSA: 485/535, DiD: 644/670, doxorubicin: 470/585, camptothecin: 370/450.

2.4.4. MNS-loaded PEG-*b*-PPS Nanocarrier Physicochemical Characterization

DLS: Dynamic light scattering (DLS) measurements of all nanoparticles were done using a Zetasizer Nano-ZS (Malvern Instruments, UK). All samples were diluted 1 in 1000 using PBS and then analyzed.

Cryo-TEM: For cryo-TEM, a pretreated holey carbon 400 mesh TEM grid was applied with 5 µL of the sample (5 mg/ml) and plunge-frozen with a Gatan Cryoplunge freezer. These specimens were imaged using a JEOL 3200FS transmission electron microscope operating at 300 keV at 4000× nominal magnification. All the images were collected in vitreous ice using a total dose of ~10 e− Å−2 and a nominal defocus range of 2.0–5.0 µm. Micrographs were acquired as 20-frame movies during a 5 s exposure using a Gatan 3.710 × 3.838 pixel K2 Summit direct electron detector operating in counting mode. A Digital Micrograph software (Gatan) was utilized to align individual frames of each micrograph and compensate for stage and beam-induced drift. These aligned images were summed up and used for image processing. A tilt range of −15° to +15° at was utilized and individual images were taken at −15°, 0°, and +15°.

SAXS: Small-angle X-ray scattering studies were performed at the DuPont-Northwestern-Dow Collaborative Access Team (DNDCAT) beamline at Argonne National Laboratory's Advanced Photon Source (Argonne, IL) using 10 keV (wavelength λ = 1.24 Å) collimated X-rays, as described previously.

ICP Sample Preparation: Metal concentration was measured using inductively coupled plasma mass spectrometry (ICP-MS). 50 µL of sample was added to 300 µL of concentrated nitric acid (BDH AristarPlus Nitric acid, 70%) in 15 mL conical tubes. The mixture was heated at 65°C for 3 h, and then ultrapure H_2O (18.2 Ω·m) was added to bring each sample up to 10 mL total volume.

ICP-MS was performed on a computer-controlled (QTEGA v. 2.6) Thermo (Thermo Fisher Scientific, Waltham, MA) iCapQ ICP-MS equipped with an ESI SC-2DX autosampler and autodilution system (Elemental Scientific Inc., Omaha, NE).

2.4.5.   Relaxivity and MRI

T2 relaxation times were measured on a Bruker minispec mq60 60 MHz (1.41 T) NMR spectrometer (Billerica, MA). 500 µL of each formulation was prepared such that all were at the same concentration. Each formulation was then serially diluted four times, resulting in five 500 µL samples for each formulation. Samples were heated to 37°C for 2 minutes and then placed into the spectrometer. T2 was measured using a Carr Purcell Meiboom Gill (CPMG) sequence: four scans per point, 2000 data points for fitting, monoexponential curve fitting, phase cycling, 1 ms pulse separation, and a 15 sec recycle delay. The inverse of the relaxation time ($1/T2$, s^{-1}) was plotted against the Fe concentration (mM) determined by ICP-MS for each formulation. T2 color-coded maps of MBCN samples were generated via imaging samples on a 7 T Bruker Pharmascan MRI System and then processing images using Matlab by fitting the signal decay of each pixel to a single exponential function.

2.4.6.   Oxidation Responsiveness and Serum Stability

To study oxidation responsiveness, MBCNs (0.2 mL, 5 mg/mL) were incubated with 0.2 mL of hydrogen peroxide for 4 or 24 h at 37°C. Following incubation, samples were centrifuged for 10 minutes at 10,000 Gs. The supernatant and pellet were collected separately, and the pellet was gently resuspended by slowly pipetting up and down, with no residual precipitates observed on the tube walls or in solution. Samples were then analyzed via DLS and ICP-MS.

Similarly for serum stability studies, MBCNs (0.2 mL, 5 mg/mL) were incubated with 0.2 mL of 1X fetal bovine serum (FBS) for 4 or 24 h at 37°C. Following incubation, samples were centrifuged for 10 minutes at 10,000 Gs to pellet the MBCNs, which were resuspended in 0.4 mL of 1X PBS by gently pipetting up and down to achieve complete resuspension of the pellet without residual precipitates, and then analyzed via DLS and ICP-MS.

2.4.7.   Cellular Uptake

MCF7 breast cancer cells were seeded in each well of a 12-well plate and cultured overnight. MBCNs (0.75% MNS or 1.25% MNS by weight) were co-loaded with FITC-BSA and DiD were added to each well (5 mg/mL in PBS, 100 μL) were added to each well and incubated for 4 h. After incubation, cells were washed three times with PBS and harvested in 0.5 mL PBS for either flow cytometry or metal quantification per cell. For metal quantification, cells were first counted using a Guava EasyCyte Mini Personal Cell analyzer. Briefly, 50 μL of the cell suspensions was mixed with 150 μL Guava ViaCount reagent and stained at room temperature for 5 minutes. Following this, the samples were vortexed and then counted using the Guava analyzer. The remaining 450 μL of cell sample was digested with 3% nitric acid and 0.75% hydrogen peroxide at 65 °C for 3 h as described above, and then analyzed for their iron content using a computer-controlled (QTEGA v. 2.6) Thermo (Thermo Fisher Scientific, Waltham, MA) iCapQ ICP-MS. For flow cytometry, samples were then stained with Zombie Aqua (live/dead stain) and analyzed using a LSRII flow cytometer (BD Biosciences).

2.4.8.   Confocal Microscopy

MCF7 cells (2×10^5 cells per ml, 150 μL) were plated in each well of an 8-well coverslip-bottom slide and cultured overnight. MBCNs co-loaded with FITC-BSA and DiD were added to

each well (5 mg/mL in PBS, 100 µL) were added to each well and incubated for 4 h. After incubation, the cells were washed with DMEM, and stained with DAPI (nuclear stain). The cells were then fixed and imaged using a 63× oil-immersion objective on a SP5 Leica confocal microscope.

2.4.9. Cytotoxicity

MCF7 breast cancer cells were seeded in a 96-well plate at 2×10^4 cells per well. Cells were treated with 0.5 mg/mL of MBCNs (loaded with 0.75% MNS or 1.25% MNS by weight) in triplicate and incubated for 24 h. MTT reagent (3-(4,5-dimethylthiazol-2-yl)-2,5-diphenyl-2H-tetrazolium bromide, 10 µL of 5 mg/mL solution in PBS) was added to each well and incubated for 5 h. Following this, the media was removed from each well and 200 µL of dimethyl sulfoxide (DMSO) was added to dissolve the precipitated formazan crystals. The absorbance of the wells was then measured using a plate reader at 570 nm, with the cell viability percentage calculated using: Cell viability % = (Absorbance of MBCN treated cells/absorbance of PBS treated cells) x 100.

2.4.10. Scanning Transmission Electron Microscopy

MBCN characterization: 1µL of 5mg/mL MBCNs were mixed thoroughly with 1µL of 2% methyl cellulose and 3µL of water. .5µL of the mixture was deposited on Formvar/Carbon 200 Mesh Copper TEM grids from Electron Microscopy Sciences that were glow discharged to create a hydrophilic surface.

Cell uptake analysis: For cellular uptake analysis via STEM, MCF7 cells (2×10^6 cells) were plated in T75 flasks and cultured overnight. Cells were treated with 0.75 mg/mL of MBCNs or PBS and incubated for 4 h. Following this, cells were collected and fixed in a solution of 2.5%

glutaraldehyde, 2% paraformaldehyde in 0.1M sodium cacodylate buffer and post fixed in 2% osmium tetroxide prior to dehydration in a graded series of ethanol. The cells were then infiltrated with EMBed812 epoxy resin and embedded in Beem capsules. The resin was polymerized at 60C for 48 h. 80nm thin slices of the fixed and embedded cells were gathered on slotted grids with a diamond knife using a Leica UC7 ultramicrotome, and the sections were stained with 3% uranyl acetate and Reynold's lead citrate solutions to enhance relative contrast. Image data of the stained ultra-thin sections were gathered in a Hitachi HD2300 STEM at 80keV utilizing the high angle annular dark field detector (HAADF). Scanning transmission electron microscopy images were gathered in a Hitachi HD2300 STEM at 80keV utilizing the high angle annular dark field detector (HAADF).

2.4.11.   Energy Dispersive X-ray Spectroscopy

EDS maps were taken on a Hitachi HD-2300A dedicated STEM equipped with dual EDS detectors and Thermo Fischer Scientific NSS software. Operating at 200kV with a 58μA emission current and an aperture with 75μm diameter, over 40 frames of a 512 x 384 pixel EDS map were collected in EDX Mode. The overall frame time was 10s with a pixel dwell time of 50 μs. Data was processed by binning with a 15 x 15 kernel size.

2.4.12.   Animal Care and Use

C57BL/6J female mice, 8−10 weeks old, were purchased from Jackson Laboratories. The Center for Comparative Medicine at Northwestern University was used to house and maintain all of the mice. All animal experimental procedures were performed according to protocols approved by the Northwestern University Institutional Animal Care and Use Committee.

2.4.13.   *In vivo* Administration of MBCNs

BCN formulations (150 µL, 5 mg/mL) or controls were injected intravenously into C57BL/6J mice via the tail vein. After 4 h, 24 h, or 7 days, 500 µL of blood was collected retro-orbitally, and mice were euthanized. Whole body perfusion via the heart was done with 3 mL of 1X PBS. The liver, kidneys, spleen, lungs, hearts, and brains were collected for imaging and ICP-MS analysis.

2.4.14.   Organ Level Biodistribution of MBCNs

The liver, kidneys, spleen, lungs, hearts, and brains were imaged using an IVIS Spectrum *in vivo* imaging system (PerkinElmer, Waltham, MA). Organs were imaged using the preset filter for indocyanine green (ICG) with acquisition settings of 5 seconds exposure time and 0.5 mm height. Living Image software was used to calculate total radiant efficiency.

Following imaging, organs were submerged in 1.5 mL concentrated nitric acid and 375 µL hydrogen peroxide and heated at 65°C for 3 h. Milli-Q H2O was added to bring each sample up to 50 mL total volume. ICP-MS was then performed to detect metal content of tissues as described above using a computer-controlled Thermo iCapQ ICP-MS.

2.5.   Acknowledgments

I would like to acknowledge Sharan Bobbala for his help with the characterization of bicontinuous nanospheres via SAXS, cargo loading studies, and oxidation studies. His help with planning and executing several of these studies, and discussions on BCNs overall were critical for the completion of this work. I also want to acknowledge Yu-Gang Liu for his assistance with all of the animal work in this project. I would also like to acknowledge Chamille Lescott for her work

2.6. Publications in this Chapter

Sections of this chapter have been published with the following citation information:

Modak M, Bobbala S, Lescott C, Liu YG, Nandwana V, Dravid VP, Scott EA. Magnetic Nanostructure-Loaded Bicontinuous Nanospheres Support Multicargo Intracellular Delivery and Oxidation-Responsive Morphological Transitions. ACS Appl Mater Interfaces. 2020 Dec 16;12(50):55584-55595. doi: 10.1021/acsami.0c15920. Epub 2020 Dec 1. PMID: 33259182

CHAPTER 3

3. **Thermal Activation and Magnetic Targeting Characterization of MNS-encapsulated PEG-*b*-PPS Nanocarriers**

3.1. Abstract

Metal ferrite MNS have great therapeutic potential due to their superparamagnetic properties, which primarily arise from their ultrasmall size (< 20 nm). Aside from providing the ability to generate MRI contrast enhancement, these superparamagnetic properties provide MNS with the ability to generate heat via thermal activation and to be magnetically guided via an external magnetic field. Here, I characterized the ability of MNS-encapsulated PEG-*b*-PPS nanocarriers to be (i) thermally activated for triggered drug release and cancer cell death applications, and (ii) magnetically guided.

3.2. Introduction

In this chapter, I explore two specific therapeutic applications of MNS-encapsulated PEG-*b*-PPS nanocarriers: thermal activation and magnetic targeting. To best understand the results discussed here, I will first introduce (i) the principle of thermal activation of metal ferrite MNS and its uses for triggered drug release and cancer cell apoptosis, and (ii) the utility of magnetic-guidance for enhancing nanocarrier delivery.

3.2.1. Thermal Activation

Given their superparamagnetic nature, metal ferrite MNS have the ability to generate heat under an external radiofrequency (RF) field via a process known as thermal activation[24]. The heat generated via thermal activation of MNS can be used both for direct killing of cancer cells via

hyperthermia and for triggered release of therapeutic cargo co-delivered with the MNS[110, 126]. This thermal activation ability of the metal ferrite MNS from the Dravid Group has been optimized in earlier studies via tailoring the composition and surface properties of the MNS[26], harnessed to achieve actuated release of therapeutic payloads from MNS-encapsulated magnetic lipid nanocapsules (MLNCs)[110], and proven to induce cancer cell death upon RF field exposure, both with and without concurrent anticancer drug delivery[126].

The process of thermal activation of MNS relies on the conversion of magnetic energy to thermal energy. Under the appropriate external RF field, generally in the hundreds of kHz, the magnetization direction of metal ferrite MNS rapidly switches directions, alternating back and forth[24]. As this occurs, magnetic energy is lost and converted to thermal energy through two separate mechanisms. First, the physical rotation of the MNS during thermal activation as their magnetization direction switches causes frictional energy losses, in a process known as Brownian relaxation[24]. Additionally, magnetization reversal during thermal activation, known as Neel relaxation, represents another form of energy loss[24]. Together, Brownian and Neel relaxation result in the generation of thermal energy and the subsequent local temperature elevation around the MNS.

The target temperature of thermal activation-based strategies for inducing cancer cell death is between 41 – 46 °C, at which cellular processes mediated by heat shock proteins (hsp) become activated and ultimately result in apoptosis[141]. Above this range, necrosis and carbonization can occur as opposed to apoptosis. Therefore, for MNS and their delivery systems it is crucial to characterize and tune their thermal activation properties to ensure adequate temperature elevations for apoptosis while avoiding the risk of inducing necrosis. Additionally for achieving thermal

activation-triggered drug release via MNS-encapsulated nanocarriers, careful engineering of such systems is needed to achieve actuated cargo release either via (i) compromised structural stability of the MNS delivery system[110] or (ii) a temperature elevation above the lower critical solution temperature (LCST) of the MNS delivery system with subsequent change in the nanocarrier structure and cargo release[126].

3.2.2.   Magnetic Targeting

In addition to their potential for thermal activation, metal ferrite MNS also have the ability to be magnetized and spatially manipulated due to their superparamagnetism[24]. While magnetic guidance of MNS has been explored for the applications of micro-mixing[142] and colloidal assembly[143], an especially intriguing application of magnetic guidance of MNS their accumulation in target tissues via an external magnetic field[144, 145]. Such target tissues include tumors, most often tumors of the central nervous system (CNS) which are past the blood brain barrier (BBB) and are especially hard to target. Several MNS systems have been developed and explored for magnetic guidance[145, 146]. These systems use a powerful neodymium magnet (0.01-0.22 T) as the source of an external magnetic field, with the magnetic either being implanted internally[146] or fixed externally[147] near the tumor or target accumulation site. Overall, such magnetic guidance strategies are promising for enhancing drug delivery, though they require optimization for each individual MNS system.

3.3.   Results and Discussion

3.3.1.   Characterization of MMC and MBCN Thermal Activation

Following successful assembly and characterization of MNS-encapsulated PEG-*b*-PPS micelles (MMCs) and bicontinuous nanospheres (MBCNs) as discussed in Chapter 2, I aimed to characterize their thermal activation capability. For this study, MNS-encapsulated MC and BCN formulations were prepared via flash nanoprecipitation (FNP), with 1.0% *w/w* MNS:polymer encapsulated. Samples were then placed in the coil of the RF generator for thermal activation. The following parameters were kept constant for all of the following experiments as per the instrument protocol: power level of 5 kW and frequency of 300 kHz. The bulk temperature of each sample was measured over time via a nonmetallic temperature probe.

The temperature profiles of MBCNs and MMCs upon 2 minutes of thermal activation is shown in Figure 3-1a, with the rate of temperature change calculated and plotted in Figure 3-1b. These MBCN and MMC formulations had very similar rates of temperature change, both increasing about 0.4 °C in 2 minutes (Figure 3-1a). The initial temperature prior to thermal activation was slightly variable depending on ambient temperature at that moment in time.
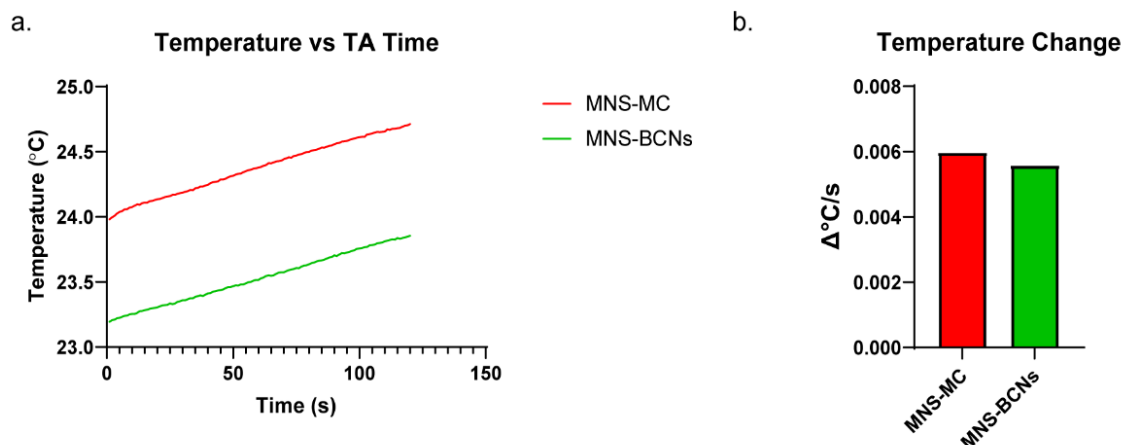
Figure 3-1. Thermal activation of MBCNs and MMCs. a) Temperature profiles of MNS-encapsulated micelles (MMCs) and bicontinuous nanospheres (MBCN) upon two minutes of thermal activation.

This increase in temperature of MNS-encapsulated formulations was specifically proven to be due to thermal activation in a subsequent study comparing the temperature profile of MBCNs placed in the RF coil with and without turning on the RF field for 10 minutes (Figure 3-2). Dotted red and black lines represent when the RF field was turned on and off, respectively. MBCNs placed in the RF coil without turning on the RF field (Figure 3-2, black line) actually decreased in temperature at a steady rate, likely due to returning to ambient temperature after any transient temperature increase from being held in my hands during sample setup. On the other hand, upon turning on the RF field with MBCNs in the sample coil (Figure 3-2, green line), the bulk sample temperature steadily increased until the field was turned off, after which the temperature immediately decreased. This data confirms that it was the effect of the RF field that contributed to the observed temperature increases. Interestingly in this second study, the temperature increase of MBCNs was found to be more gradual, rising about 0.4 °C in 10 minutes as compared with 0.4 °C in 2 minutes in the previous study (Figure 3-1). This was surprising given that the same MBCN sample (1.0% *w/w* MNS:polymer) was used for these studies. Overall, the temperature elevations

seen via thermal activation were quite variable depending on the experiment, as discussed later in

this chapter.
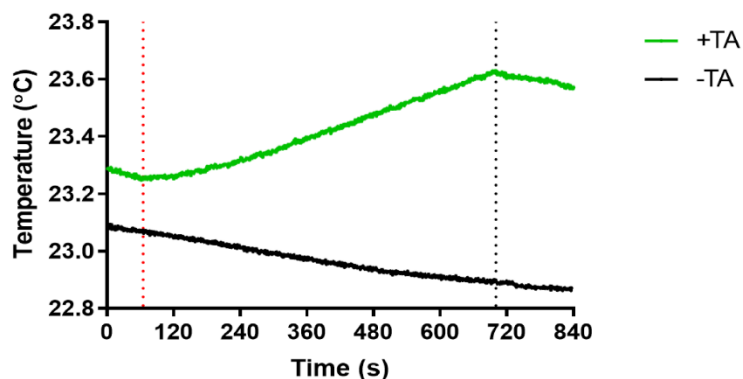
Figure 3-2. MBCN temperature profile with and without thermal activation. Temperature profiles of MBCNs (1.0% *w/w* MNS:polymer) with (green) and without (black) ten minutes of thermal activation. Red and black dotted lines represent when the RF field was turned on and off, respectively.

The effect of two minutes of thermal activation on the size of MBCNs and MMCs (both

1.0% *w/w* MNS:polymer) was also assessed via DLS (Figure 3-3), with no significant difference

in nanocarrier size seen after 10 minutes of thermal activation.
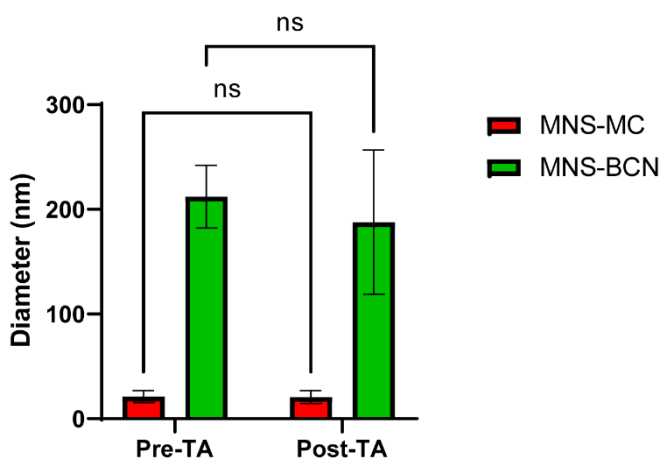
Figure 3-3. DLS characterization of MMCs and MBCNs pre- and post-thermal activation. Error bars = S.D., n = 3, significance determined via Student's t-test, ns = not significant.

3.3.2.   Effect of MNS Encapsulation on TA of MBCNs and MMCs

The effect of varying the MNS encapsulation within MBCNs and MMCs on their thermal activation ability was also investigated. Here, MBCNs and MMCs were formulated with increasing weight % of MNS to PEG-*b*-PPS polymer, with subsequent characterization of temperature profiles upon thermal activation (Figure 3-4). In these studies, final sample polymer concentrations were matched, at 5 mg/mL PEG-*b*-PPS. For both MBCNs and MMCs, the temperature elevation rate and the total temperature elevation generally increased with higher MNS encapsulation. This increase in thermal activation efficiency is likely due to larger clusters of MNS within each individual nanocarrier, as such clustering is known to enhance thermal activation[110]. While the presence of these larger clusters of MNS within PEG-*b*-PPS BCNs with higher MNS encapsulation has been confirmed (Chapter 2, Figure 2-6), additional cryo-TEM studies are still needed to determine if the same effect is occurring for MMCs with higher MNS encapsulation.

Aside from the general trend of increasing temperature elevation with increasing MNS encapsulation, the data in Figure 3-4 also illustrates the variability of the temperature profiles measured during thermal activation. Specifically, large temperature spikes would occasionally be seen during thermal activation, occurring quite randomly. Examples of this can be seen in Figure 3-4a for the 1.0% MBCNs at around the 5 minute mark, and in Figure 3-4b for the 2.0% MMCs at around the 8 minute mark. To further explore this, repeated thermal activation trials of the same MBCN formulation were performed (Figure 3-5). Here, large spikes in temperature can be seen for trials 2 and 3 at the 1.5 minute mark, but not at all over several minutes of thermal activation in trial 1. During the thermal activation studies, samples were left untouched within the RF coil

for safety as well as to not alter temperature measurements. This unpredictable variability of temperature profiles during thermal activation, even within the same sample, suggests that perhaps this is due to effects of the thermal activation instrumentation and a need for optimization of instrument parameters, and not something that could be altered by optimizing nanocarrier formulation.

Overall, due to these unpredictable spikes in temperature, comparisons between MNS-encapsulated formulations were quite difficult to make. One parameter that can be used to compare the thermal activation efficacy of various formulations is their specific absorption rate (SAR), given in W/g, which is a measure of their heat dissipation power[126]. However, calculation of an MNS-encapsulated nanocarrier's SAR requires accurate assessment of its temperature elevation relative to its Fe content, and thus could not be done here due to the unusually high variation in sample temperature profiles upon thermal activation.

Finally, while temperature elevation was seen for both MBCNs and MMCs, the degree of temperature elevation did not reach levels needed for cytotoxicity (up to 41°C) at least within 10 minutes of thermal activation for MBCNs (Figure 3-2). Looking at the temperature elevation of 0.4°C over 2 minutes as seen in one particular trial (Figure 3-1), this suggests that at least 20 minutes of thermal activation may be needed to reach a cytotoxic temperature of 41°C from a physiologic temperature of 37°C. While this is on par with studies of metal ferrite MNS alone[26], given the influence of the variable spikes in temperature during thermal activation studies, instrument parameters of the RF generator may first need to be optimized before making larger conclusions about the thermal activation performance of MNS-encapsulated PEG-*b*-PPS nanocarriers.
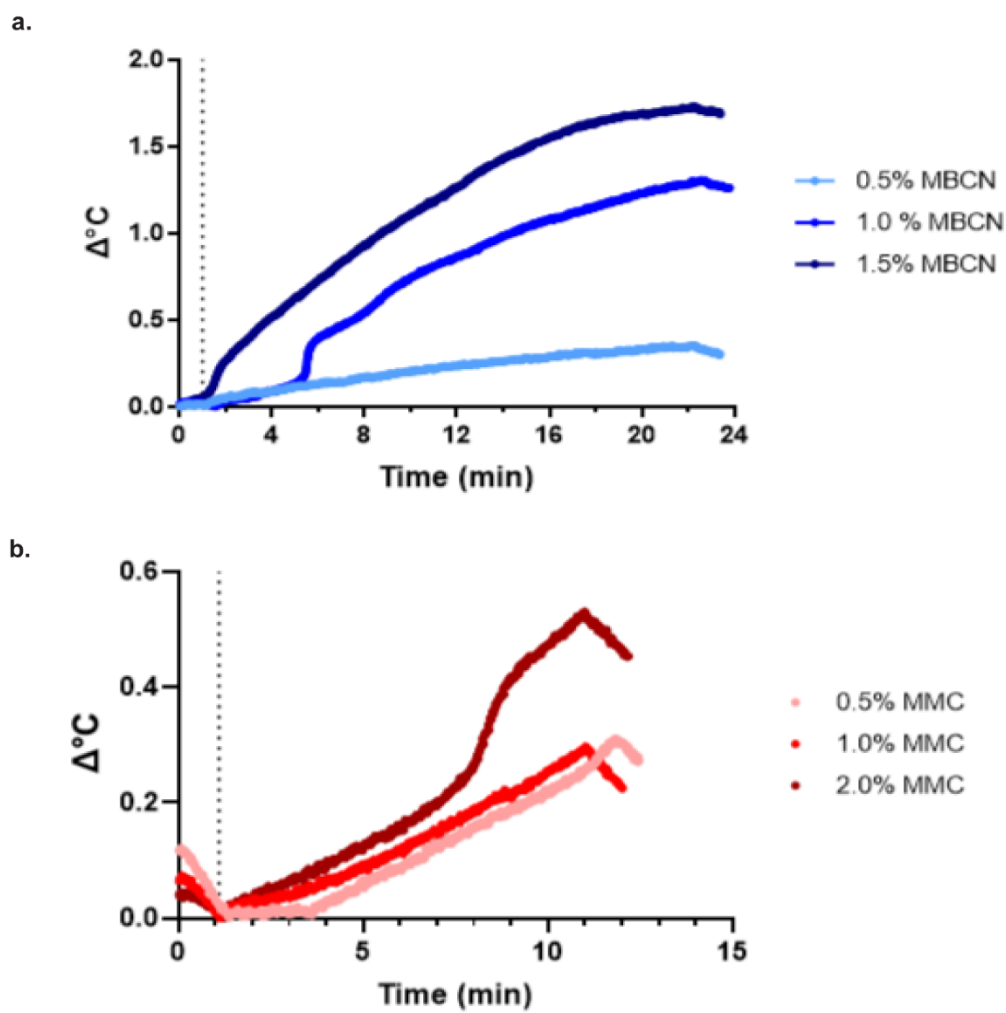
Figure 3-4. Thermal activation of MBCNs and MMCs with increasing MNS encapsulation. Representative thermal activation temperature profiles of a) MBCNs and b) MMCs with increasing MNS encapsulation.
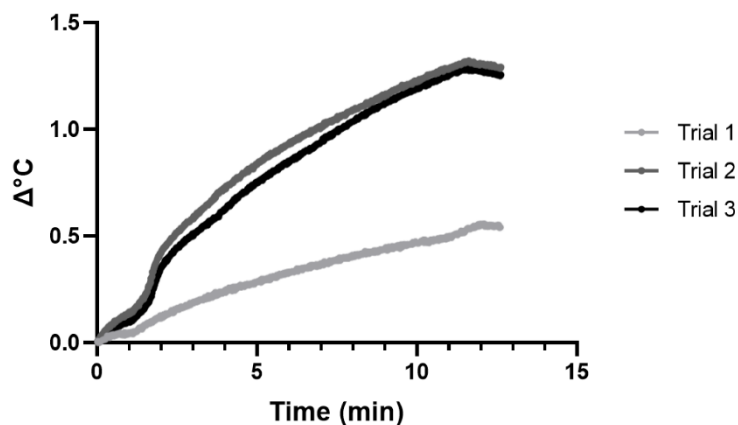
Figure 3-5. Multiple thermal activation trials of one MBCN formulation. Thermal activation temperature profiles of one MBCN formulation over three independent measurements.

3.3.2. Effect of TA on Payload Release and Cytotoxicity of MBCNs and MMCs

Aside from assessing the temperature elevation of MNS-encapsulated PEG-*b*-PPS nanocarriers, the final set of studies thermal activation studies I conducted were to assess if thermal activation could facilitate release of a co-encapsulated small molecule drug for inducing cancer cell death. Here, the expected mechanism of release of any payloads was assumed to be due to disruption of nanocarrier structure, as seen previously with magnetic lipid nanocapsules[110].

For this study, the anticancer agent camptothecin (CPT) was co-loaded into MBCNs along with MNS to form CPT-MBCNs. The initial fluorescence of CPT-MBCNs was measured (Figure 3-6, pre-spin) before samples underwent thermal activation for 2 minutes. Following thermal activation, CPT-MBCN samples were centrifuged to collect nanocarriers in a pellet, washed with 1X PBS, and their fluorescence was measured again (Figure 3-6, post-spin). If any CPT was being released via thermal activation, a decrease in CPT-MBCN fluorescence would be expected. While there was a slight decrease in CPT-MBCN fluorescence post-thermal activation and post-spin, this

decrease was observed for both samples that underwent thermal activation (+TA) as well as those that did not (-TA). This suggests that this decrease in fluorescence was not due to thermal activation itself, but instead due to sample processing and potential loss of nanocarriers during the spin and wash steps. Perhaps different thermal activation parameters, different drug concentrations, or different MNS encapsulation % is needed to achieve triggered drug release.
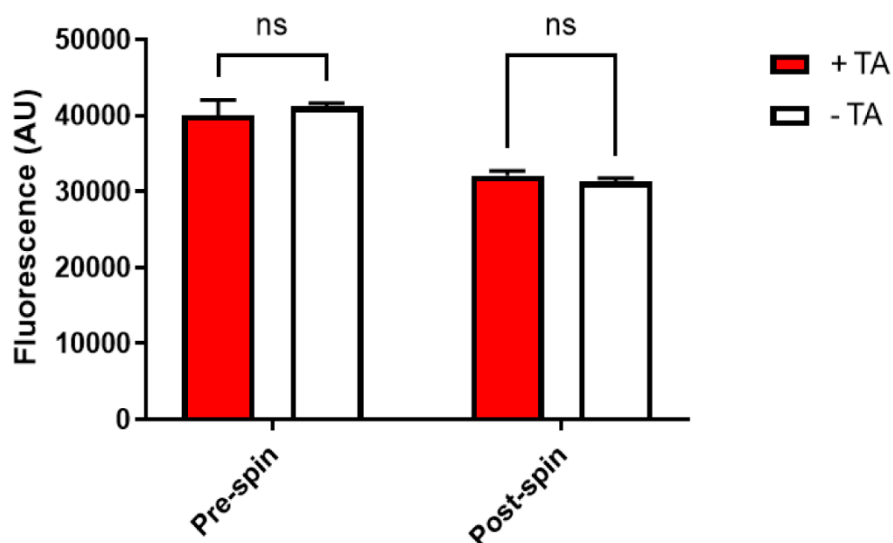
Figure 3-6. Thermal activation-triggered drug release studies with CPT-MBCNs. Fluorescence of CPT-encapsulated MBCNs (CPT-MBCNs) pre- and post-centrifugation, both with and without thermal activation (TA). Error bars = S.D., n = 3, significance determined via Student's t-test, ns = not significant.

Although there was no observed TA-triggered release of small molecule cargo from PEG-*b*-PPS nanocarriers co-loaded with anticancer agents and MNS, the ability of such nanocarriers to induce cell death in cancer cells via TA was still investigated in a pilot study. Here, MMCs (1.0% *w/w* MNS:polymer) were co-loaded with paclitaxel, an anticancer agent sold under the brand name of Taxol, to form PTX-MMCs. MCF7 breast cancer cells were then treated with MMCs or PTX-MMCs and underwent thermal activation for 2 minutes (Figure 3-7). Thermal activation was able to induce cell death in both MMC-treated and PTX-MMC-treated cells, as compared with cells

that did not undergo thermal activation. Notably, thermal activation led to more cytotoxicity for cells treated with PTX-MMCs that underwent thermal activation versus those that did not. This suggests that thermal activation may be responsible for this increase in cytotoxicity through triggered release of the encapsulated PTX. Overall, these data suggest that (i) MMCs are able to induce cell death via thermal activation, and that (ii) thermal activation of MMCs dual-loaded with an anticancer therapeutic cargo can increase cytotoxicity, potentially through triggered cargo release.

This result is somewhat surprising, given that in the previous study (Figure 3-6), thermal activation was insufficient to trigger release of an anticancer agent, though that study was performed with a different nanocarrier morphology and different drug. The two MNS-encapsulated nanocarriers studied here, MMCs and MBCNs, have vastly different structures that could explain these surprising results. MBCNs are more complex and more stable nanocarriers[148], with the encapsulated MNS shielded from the bulk environment via multiple bilayer membranes of PEG-*b*-PPS polymer (Chapter 2, Figure 2-2). On the other hand, MMCs have encapsulated MNS in their hydrophobic core that are enveloped by just one single layer of PEG-*b*-PPS polymer (Chapter 2, Figure 2-3). Given this much simpler structure, MMCs should theoretically be easier to disrupt and achieve payload release from compared with the more stable MBCNs, which may have contributed to the enhanced cytotoxicity of PTX-MMCs with thermal activation versus without. However, this is inconsistent with the lack of change of MMC size following thermal activation as measured in a previous study (Figure 3-3). Aside from nanocarrier morphology, differences in payload properties could also influence the ability of thermal activation to trigger their release from within nanocarriers. Factors such as payload size and hydrophobicity of small
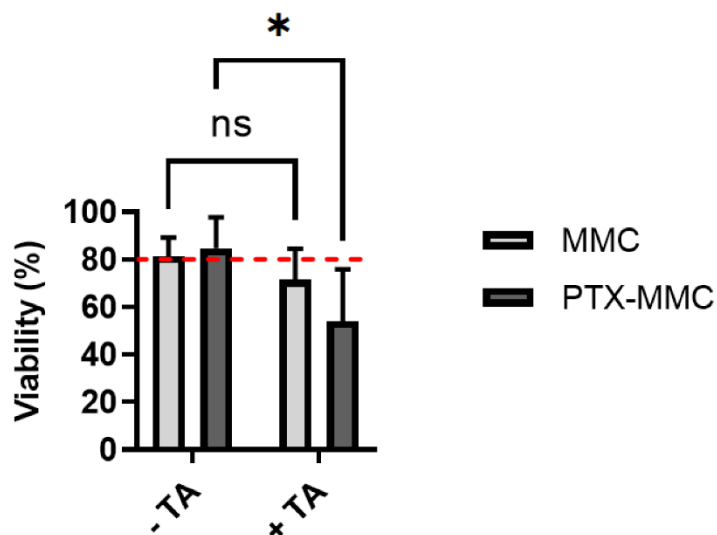
Figure 3-7. Thermal activation-mediated cytotoxicity studies with MMCs. Viability of MCF7 breast cancer cells after treatment with MMCs and subsequent thermal activation, both with and without co-loading of paclitaxel (PTX). TA = thermal activation. Error bars = S.D., n = 3, significance determined via Student's t-test. , * $p < 0.033$, ns = not significant.

molecular cargo may certainly influence how likely they are to be released from within MNS-encapsulated nanocarriers with thermal activation, as these parameters are known to influence release of cargo from PEG-*b*-PPS BCNs even without any external stimuli[39].

Overall, more studies need to be done to further explore the potential of MNS-encapsulated PEG-*b*-PPS nanocarriers for thermal activation-induced payload release and cancer cell death. First, studies systematically comparing the release of payloads from MBCNs and MMCs are needed, to investigate what effect nanocarrier structure and payload properties have on thermal activation-mediated release. Additionally, studies investigating the mechanism of cell death following thermal activation via MMCs and MBCNs are needed, to determine whether the cell death is due to apoptosis or necrosis. Furthermore, the dose response of cell death based on the nanocarrier, MNS, and anticancer agent concentrations should be studied in order to determine the

optimal formulation parameters for thermal activation-induced cancer cell death. Finally, given the overall inconsistencies seen in the thermal activation studies in this chapter, thermal activation parameters themselves need to be optimized before moving forward with this platform for further applications.

3.3.3.   Magnetic Targeting of MBCNs

To explore the magnetic manipulation capability of MNS-encapsulated PEG-*b*-PPS nanocarriers, a preliminary study was conducted via embedding MBCNs within an agarose gel (0.2% agarose) to roughly simulate a biologic environment. In Figure 3-8a, this MBCN-gel can be seen as a tan colored gel in a plastic weigh boat, with the tan color arising from the embedded MBCNs. The overall homogenous color of the gel indicates the even dispersal of MBCNs within the agarose. Following gelation, a broken crescent-shaped neodymium magnet was placed below the gel in contact with the plastic weigh boat and left overnight to observe any accumulation of the MBCNs. Notably, accumulation of MBCNs can be seen following the overnight incubation as a dark brown outline within the gel in the same pattern as the magnet (Figure 3-8b). The image of the gel was converted to grayscale for more clarity (Figure 3-8c). This result of MBCN accumulation suggests the utility of MBCNs for magnetic guidance, though more thorough studies are needed for optimization of this application to build upon this crude pilot study presented here.

Specifically, other morphologies of MNS-encapsulated PEG-*b*-PPS nanocarriers like MMCs should be explored for their magnetic guidance capabilities. Additionally, the effect of field strength and exposure time to the magnetic field should be assessed, as only one magnet with an unknown strength and an overnight timepoint was studied here. Finally, the effect of the amount of MNS-encapsulation on targeting ability should be explored, in order to determine the optimal

MNS:polymer ratio for this application. More specific studies to better assess the magnetic guidance of MNS-encapsulated PEG-*b*-PPS nanocarriers are discussed in Chapter 5 (Future Directions).
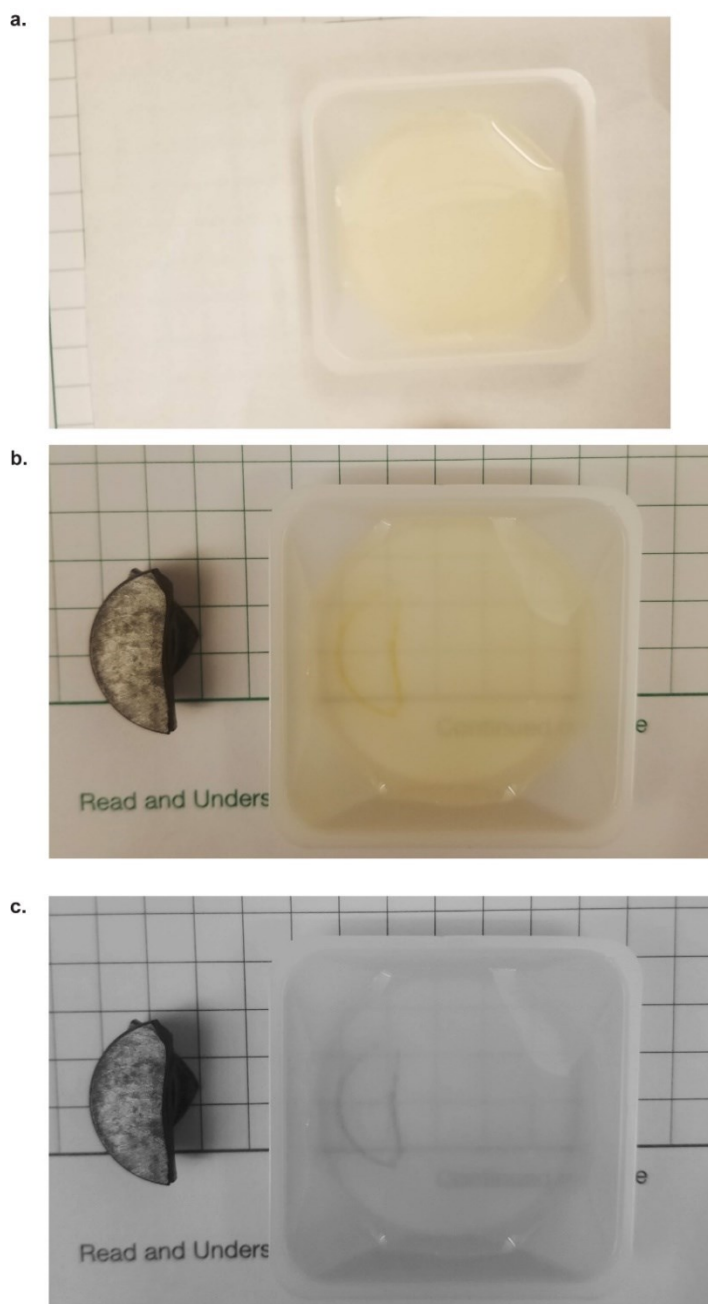
Figure 3-8. Magnetic manipulation of MBCNs. MBCNs embedded in a 0.2% agarose gel a) before and b) after magnet exposure. c) Grayscale image of post-magnetic field exposure gel to better show magnetic accumulation of MBCN.

3.4. Materials and Methods

3.4.2. Thermal Activation

Thermal activation experiments were performed on an MSI Automation Inc. Hyperthermia Research System (model hyper 5) RF generator at a frequency of 300 kHz and a power of 5 kW. Nanocarrier formulations were positioned within the 5 cm coil generating 5 kA/m AC magnetic field. A nonmetallic, nonmagnetic optical temperature probe was used to record temperature over time.

3.4.3. Cytotoxicity

MCF7 breast cancer cells were seeded in 35 mm Petri dishes at 0.3×10^6 cells per dish. Cells were treated with 0.5 mg/mL of MBCNs (with or without co-loading of anticancer drugs) and incubated for 4 h. Following this, cell dishes were placed in the RF coil for thermal activation studies, and then cells were plated in 96 well plates. MTT reagent (10 µL of 5 mg/mL solution in PBS) was added to each well and incubated for 5 h. Following this, the media was removed from each well and 200 µL of DMSO was added to dissolve the precipitated formazan crystals. The absorbance of the wells was then measured using a plate reader at 570 nm, with the cell viability percentage calculated using: Cell viability % = (Absorbance of MBCN treated cells/absorbance of PBS treated cells) x 100.

3.4.4. Magnetic Targeting

A 0.2% agarose gel with MBCNs embedded was formed by adding 0.4 g LE Quick Dissolve Agarose to 100 MilliQ water and mixing with a 5 mg/mL solution of MBCNs (1% *w/w* MNS:polymer) at a 1:1 ratio. This MBCN:agarose solution was then carefully added to a plastic

weigh boat and allowed to solidify for 1 hour. Following this, a neodymium magnet was placed under the weigh boat overnight, and the gel was inspected the next day.

3.5. Acknowledgments

I would like to acknowledge Vikas Nandwana for providing all of the MNS formulations used here and for his assistance and access to the thermal activation instrument. Without him, this work would not have been possible. I would also like to acknowledge the Clare Lab for providing the MCF7 cell line used in this work.

3.6. Publications in this Chapter

Sections of this chapter have been published with the following citation information:

CHAPTER 4

4. Development of T1 MRI Contrast-Enhancing PEG-*b*-PPS Nanocarriers for Immune Cell Targeting in Atheromas

4.1. Abstract

Atherosclerosis is a chronic inflammatory disease driven by the activity of specific inflammatory cells, including dendritic cells (DCs) and macrophages. Targeting these cells is of interest for therapeutic delivery to atherosclerotic plaques and for diagnostic monitoring of plaque progression. On the therapeutic side, the Scott Lab has made progress towards targeting DCs within early stage atherosclerotic plaques with PEG-*b*-PPS PS via a specific targeting peptide, P-D2. However, for diagnostic assessment of plaque progression, current small molecule contrast agents such as Gd-DOTA are not suited for such targeted imaging applications due to their lack of target specificity. Loading of such small molecule contrast agents within PEG-*b*-PPS nanocarriers is a promising strategy for achieving their controlled delivery. In this chapter, I discuss my work towards achieving this goal of non-invasive assessment of plaque progression. I first share my progress in engineering PEG-*b*-PPS polymersomes (PSs) to load and deliver Gd-DOTA for MRI contrast enhancement, followed by my exploration of the P-D2 peptide displaying PS for targeting of atherosclerotic plaques at both early and late stages of atherosclerotic cardiovascular disease.

4.2. Introduction

In this chapter, I discuss the development of PEG-*b*-PPS PS for the display and delivery of Gd-DOTA for T1 MRI, with the goal of utilizing these nanocarriers for the non-invasive imaging of atherosclerotic disease via targeting of DCs. For clear understanding of the findings discussed here, I will first summarize: (i) the role of DCs in atherosclerotic disease, their utility for

atherosclerosis staging, and approaches to targeting them, and (ii) the utility of T1 MRI contrast agents, specifically of gadolinium-based contrast agents (GBCAs), and how they are commonly delivered via nanocarriers.

4.2.1.   Role of DCs in Atherosclerotic Plaque Development

DCs are key mediators of atherosclerosis, due to their function in cholesterol regulation (uptake of lipoproteins), role in antigen presentation to and activation of T cells, and participation in efferocytosis (clearance of apoptotic cells)[3]. Accumulation of DCs within plaques is predictive of more severe atherosclerotic disease and is associated with a "vulnerable" plaque phenotype, characterized by a necrotic core and overlying fibrous scar[5]. This overlying scar is prone to rupture, which is what makes such plaques "vulnerable" and likely to result in associated complications (MACEs, etc.)[6].

The higher burden of DCs within plaques is thought to arise from their diminished ability to migrate in hyperlipidemic conditions[5]. First, impaired migration of DCs is hypothesized to impair their ability to participate in cholesterol regulation and efferocytosis, resulting in a favorable environment for production of a necrotic core and subsequent vulnerable plaque formation[5]. Additionally, impaired DC migration likely leads to retention of mature DCs that continue to secrete inflammatory cytokines and recruit and activate T cells, contributing to exacerbation of local inflammation and plaque advancement[4].

DCs therefore play a key role in plaque progression, and their accumulation in late stage atherosclerotic plaques presents an opportunity for targeting atherosclerosis for both therapeutic and diagnostic applications. Other cells implicated in atherosclerotic plaque progression include macrophages, which also contribute to the chronic inflammation within plaques via ingestion of

lipoproteins, transformation into foam cells, and participation in efferocytosis[4]. As discussed in Chapter 1, macrophages have been studied extensively in recent years as targets for plaque assessment via nanocarriers. As both DCs and macrophages are implicated in atherosclerosis development, the ratio between these two cell types may provide a metric of plaque progression but has not been specifically quantified thus far.

4.2.2. P-D2 Peptide Construct for DC Targeting

Previous work has shown the ability of polymeric nanocarriers to be targeted to DCs via surface display of the P-D2 peptide sequence[50, 149], which is specific for the CD11c marker[150]. This marker has been found to be particularly highly expressed on DCs[151], and was used by the Scott Lab in 2019 to deliver immunotherapeutic treatments to DCs via P-D2-displaying PEG-*b*-PPS PS (P-D2-PS)[50].

In that study, the P-D2 targeting peptide was displayed on PS surfaces via a PEG-lipid tail construct. Our lab has shown the utility and versatility of these PEG-lipid tail-based constructs for the controlled display of targeting peptides on the surface of multiple PEG-*b*-PPS nanocarrier morphologies, such as micelles[48, 49] in addition to PS. The general design of these targeting constructs consists of (i) a lipid molecule, such as palmitic or palmitoleic acid, conjugated to (ii) a PEG spacer, which is linked to (iii) a short peptide sequence. All 3 of these components can be tailored depending on the application, such as choosing 1 or 2 lipid tails per construct; selecting the PEG linker length based on the nanocarrier morphology or for optimal peptide display[51]; and most importantly, incorporating different peptide sequences based on the targeting application.

4.2.3.   T1 MRI

GBCAs comprise the majority of MRI contrast agents and are utilized in about 40% of all clinical MRI scans[152]. In the work described here, GBCAs were focused on primarily due to the presence of functional groups such as carboxylic acids for conjugation and incorporation in nanocarrier formulations, their efficacy at T1 enhancement, and their current status of FDA approval[21]. Aside from their use in MRI, GBCAs were of particular interest here due to their potential for allowing elemental-based, inductively-coupled plasma mass spectrometry (ICP-MS) mediated quantitative tracking of nanocarriers[153], which has been a goal of the Scott Lab for the past few years.

Within the realm of GBCAs, macrocyclic chelators such as DOTA are of particular interest, due to concerns of lower stability of linear chelators such as DTPA[154]. Linear chelators tend to have higher dissociation constants for enclosed Gd ions, compared with macrocyclic chelates, resulting in a higher likelihood that free Gd can be released into circulation or surrounding tissues[155]. While chelated Gd is known to be fairly quickly cleared from the body via the kidneys, free Gd can accumulate in tissue after injection, and has been shown to occur more frequently and to a higher degree for linear GBCAs compared with macrocyclic GBCAs[156].

Approaches that have been used for incorporating macrocyclic Gd chelators into vesicular formulations like PS have included conjugation to large proteins like albumin or large molecules such as high molecular weight dextrans, and then encapsulating these within the vesicle's aqueous core. However, this approach of encapsulating Gd within the aqueous lumen of vesicular nanocarriers has been shown to be inferior to the alternative approach of binding Gd to the nanocarrier surface[23]. This is likely due to higher access to water of nanocarrier surface-bound Gd,

as even though the interior of vesicular nanocarriers is aqueous, the effectiveness of the encapsulated Gd at relaxing the nearby bulk water can vary depending on the permeability of the nanocarrier membrane[157]. Due to this, incorporation of Gd on the surface of PS bilayer membranes was a strategy used in this work.

4.3.   Results and Discussion

4.3.1.   Design, Assembly, and Characterization of DOTA Peptide Construct

With the overall goal of developing DC-targeting PS for plaque assessment via MRI, I first decided to address the objective of engineering PEG-*b*-PPS PS for MRI contrast enhancement via encapsulation or delivery of a T1 enhancing agent. For this initial approach, the approach of immobilizing Gd on the PS surface via a macrocyclic chelator was employed.

Recently, the Scott Lab has shown the utility and versatility of PEG-lipid tail-based constructs for the controlled display of targeting peptides on the surface of PEG-*b*-PPS nanocarriers[48, 50]. Here, I leveraged this same approach to facilitate the incorporation of Gd-DOTA within PEG-*b*-PPS PS (Figure 4-1). Specifically, this construct design consisted of two molecules of palmitoleic acid conjugated via a lysine residue to a PEG_6 linker, which was conjugated on the other end to a short peptide sequence: lysine, glycine, glycine, lysine, glycine, glycine, lysine (KGGKGGK). This sequence was carefully determined with each amino acid residue included for a specific purpose. Lysine residues were chosen due to the availability and accessibility of their sidechain amines for peptide coupling with carboxylic acid functional groups of DOTA molecules. Three lysine residues were chosen for this design in order to incorporate multiple DOTA molecules per peptide construct to (i) achieve higher MRI signal and higher Gd concentration per nanocarrier for ICP tracking, while (ii) maintaining a relatively short peptide chain to minimize potential

alterations of PS surface properties, given that an additional targeting peptide (P-D2) was to be incorporated later. The glycine residues were included as spacers between each lysine residue due to their inert nature. Two glycine residues were chosen in order to provide more spacing between each lysine and minimize any steric hindrance between each lysine side chain during the DOTA conjugation steps. Additionally, this spacing would also prevent any steric effects from affecting access of water molecules to each DOTA group after the final construct was synthesized. This DOTA-peptide construct (chemical structure in Figure 4-2a) was synthesized using solid-phase peptide synthesis and analyzed via Liquid Chromatography/Mass Spectrometry (LC-MS) (Figure 4-2b).
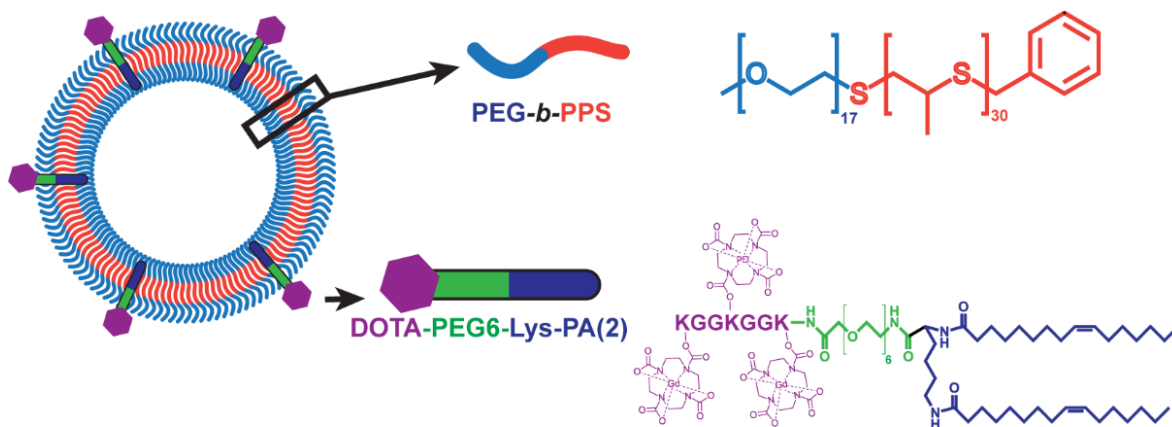
Figure 4-1. Schematic of DOTA-PS. Simplified schematic of PEG-*b*-PPS polymersomes (PS) displaying the DOTA peptide construct. Lys = Lysine, PA = palmitoleic acid.

a.

(Palmitoleic acid)2-K-(PEG6)-K(DOTA)-GG-K(DOTA)-GG-K(DOTA)

Exact Mass: 2724.64
Molecular Weight: 2726.33

b.

+ESI Scan (0.2-0.5 min, 33 scans) Frag=40.0V

2724.5897

1180.7030

824.5165

1816.0624

3906.2831

Counts (%) vs. Mass-to-Charge (m/z)
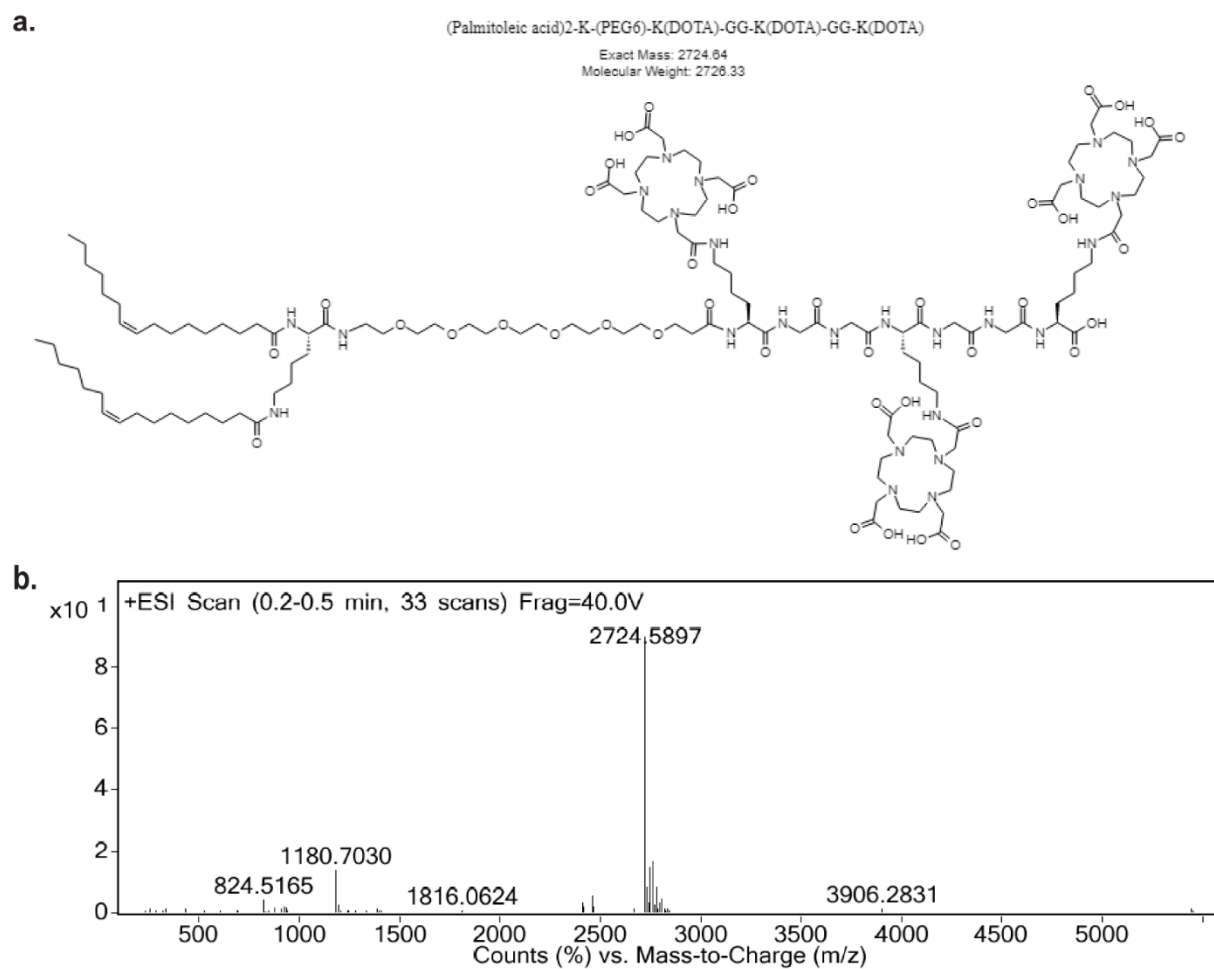
Figure 4-2. DOTA peptide construct chemical structure. a) Chemical structure and b) LC-MS/MS spectra of the DOTA peptide construct.

4.3.2.   Quantification of Gd Chelation of DOTA-PS

Following verification of successful synthesis of the DOTA peptide construct, I tested its incorporation into PEG-*b*-PPS PS. PS were self-assembled using the previously established flash nanoprecipitation method[38], and then incubated after assembly with the DOTA peptide construct at specific molar ratios of DOTA-peptide to PEG_{17}-*b*-PPS_{30} for incorporation into PS membranes[50]. The ratios I chose ranged from 0% (no peptide) to 15%, based on previous studies with similar PEG-lipid tail constructs[48-50]. The DOTA-PS were then incubated with an excess of $GdCl_3$ in 0.5 M sodium acetate buffer to facilitate Gd chelation[158]. PS samples were then filtered using a 7 kDa molecular weight cutoff spin column, to remove both unchelated Gd and free DOTA-peptide, and then analyzed using ICP-MS to quantify the Gd chelation (Figure 4-3). After filtration via the spin columns, the only Gd remaining in the sample should be that which is chelated by DOTA-peptide that has successfully inserted into PEG-*b*-PPS PS. This is illustrated in Figure 4-3, where all DOTA-PS samples were incubated with similar amounts of Gd (Pre-filter), but only the DOTA-PS samples with 5, 10, and 15% molar ratios of DOTA-peptide retained Gd
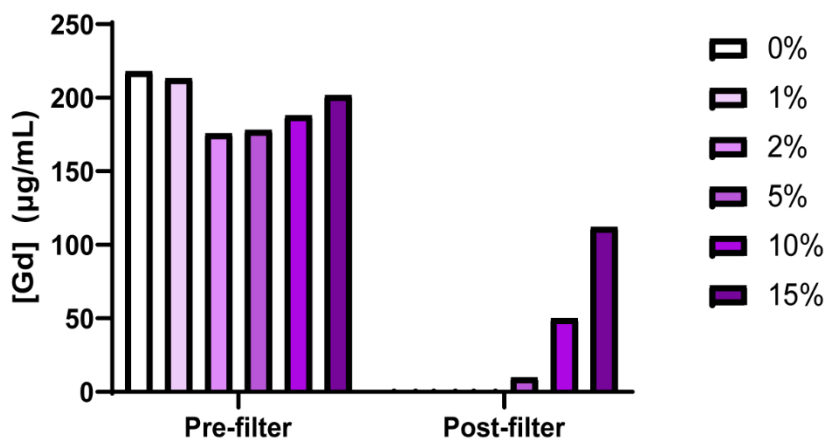
Figure 4-3. Gd chelation of DOTA-PS. ICP-MS-based quantification of Gd chelation of PS with increasing molar ratios of DOTA peptide construct displayed in the bilayer membrane. 0% = no DOTA peptide, 15% = 0.15 mol DOTA peptide:1 mol PEG_{17}-*b*-PPS_{30}.

in the μg/mL range after filtration (Post-filter). There was also an increase in the amount of Gd in each sample as DOTA-peptide display increased, serving as further confirmation of successful chelation of Gd via display of the DOTA-peptide.

4.3.3. Physicochemical Characterization of DOTA-PS

Using dynamic light scattering (DLS) and cryogenic transmission electron microscopy (cryo-TEM), the size and structure of the DOTA-PS were analyzed (Figure 4-4). DOTA-PS had an average hydrodynamic diameter of 93 nm and retained the characteristic vesicular structure of PS after DOTA-peptide insertion, with a dark outer border indicating the bilayer membrane of each PS and a lighter aqueous interior. This vesicular structure and size range is consistent with previous studies of PEG-*b*-PPS PS, both with[50] and without[36] incorporation of similar peptide constructs.
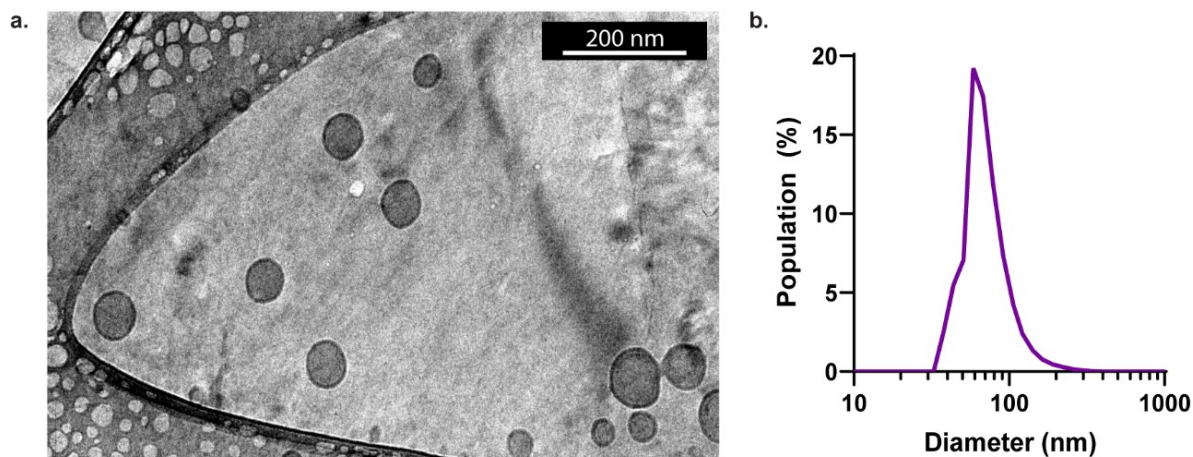
Figure 4-4. Physicochemical characterization of DOTA-PS. a) Representative cryo-TEM micrograph and b) DLS size characterization of 10 mol% DOTA-PS.

The retained vesicular structure of the PS after DOTA peptide display highlights the utility and the modularity of these types of PEG-lipid tail constructs overall. This is the fourth example now from the Scott Lab of this type of peptide construct successfully incorporated within PEG-*b*-PPS nanocarriers, with the base structure of: a lipid tail linked to PEG spacer linked to a short peptide. Each component has the potential to be modified (different lipid group, different PEG spacer length, different peptide sequence) depending on the type of nanocarrier morphology (micelles and PS) for different applications (targeting endothelial cells, targeting dendritic cells, incorporating a Gd-chelate), and in each case display of the peptide has been stable, controllable, and has not changed the resulting nanocarrier size or structure. While only one specific DOTA peptide construct was evaluated here in this work, it would be valuable to understand the effects of changing different aspects of the DOTA peptide construct (PEG spacer length, peptide sequence, or type of lipid tail) on its incorporation into PS and subsequent performance, which I discuss in Chapter 5 (Future Directions).

4.3.4.   Relaxivity and T1-weighted Imaging of DOTA-PS in Solution

In MRI, the T1 contrast enhancement effect can be measured by r_1 relaxivity, or the slope of the relaxation rate (R1, s^{-1}) when plotted versus the concentration of T1 contrast agent in mM. To assess this for the DOTA-PS, T1 times were measured on a 1.4 T relaxometer for serial dilutions of the 5 mol%, 10 mol%, and 15 mol% DOTA-PS, and then plotted against the Gd concentration of each dilution, as measured via ICP-MS (Figure 4-5a). The corresponding slope, or r_1 relaxivity per Gd, for these 3 formulations is plotted in Figure 4-5b. For all 3 DOTA-PS formulations, the r_1 relaxivity was higher than the relaxivity of free Gd-DOTA (DOTAREM) at 1.5 T, illustrated by the red dashed line in Figure 4-5b. This is likely due to the effects of the DOTA

(and chelated Gd) being displayed on the surface of a large nanocarrier. This attachment of chelated Gd on nanocarriers or macromolecules is known to increase r_1 relaxivity via decreasing the rotation or rate of tumbling of each Gd molecule[159]. Decreasing the tumbling rate increases the rotational correlation time (T_r) of a molecule, which in turn results in an increase in r_1 relaxivity per Gd at low fields (<1.5 T)[160]. Using these data, the per particle relaxivity (per mM of PS) was also calculated and was determined to be 576, 1954, and 2976 $1/(mM^{-1}*s^{-1})$.
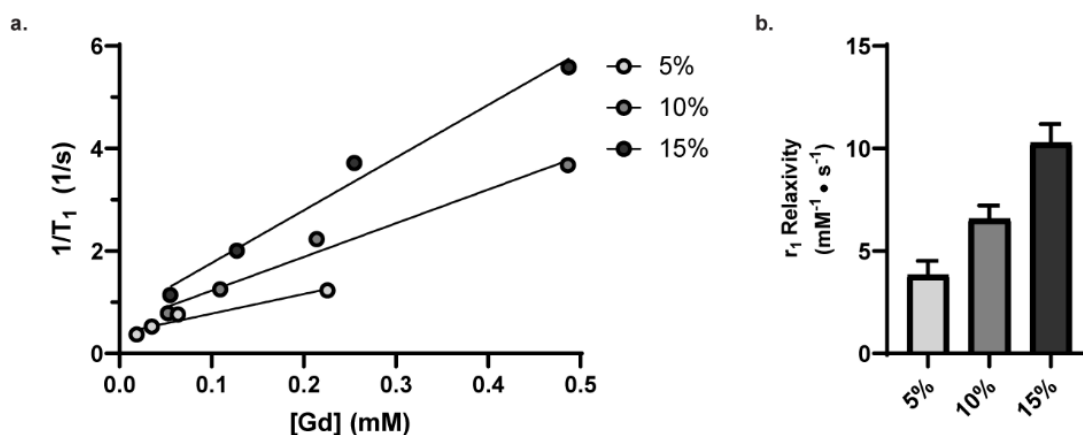
Figure 4-5. Relaxivity of DOTA-PS. a) R1 relaxation rates vs Gd concentration and b) corresponding r_1 relaxivities per Gd of different DOTA-PS with increasing mol % of DOTA peptide displayed. Error bars = S.D. N = 3.

Interestingly, both the r_1 relaxivity per Gd and per PS of the DOTA-PS increased with increasing display of the DOTA peptide up to 15 mol%. For the per PS relaxivity, this intuitively makes sense, as more Gd-DOTA per PS should facilitate more T1 shortening per PS. This is less intuitive for the per Gd relaxivity, but has been seen before with other nanocarrier systems where Gd-DOTA was varied per nanocarrier[161]. However, in this referenced study, the increase in relaxivity with more Gd per particle was seen at lower Gd concentrations until a maximum r_1 was reached. Past that point, additional Gd per particle resulted in a decrease in relaxivity likely due to "quenching" resulting from higher packing of Gd within a given volume, restricting water access

to each individual Gd. Here, higher display of DOTA peptide (more than 15 mol%) and the corresponding r_1 relaxivity was not tested due to limitations in the amount of DOTA peptide available for each experiment, but this would be intriguing to investigate in future directions. At the moment, it is largely unclear why the per Gd relaxivity increased for the DOTA-PS with increasing DOTA peptide display, but may be due to decreased local rotation and movement of the Gd-DOTA on the lysine sidechains due to steric effects as more and more DOTA peptide is displayed on the PS surface, as this decreased local rotation of Gd chelates is known to increase per Gd relaxivity[159, 162]. This concept is discussed further in Chapter 5 (Future Directions).

As a next step in the MRI characterization of the DOTA-PS, serial dilutions of DOTA-PS samples in PBS were imaged using a 9.4 T small animal scanner and used to generate color-coded maps of T1 times (Figure 4-6). DOTA-PS were successfully able to induce T1 shortening, which is what contributes to contrast enhancement in T1-weighted images. In this study, the most concentrated DOTA-PS sample had a T1 time of around 2200 ms as compared with 3000 ms for the PBS sample.
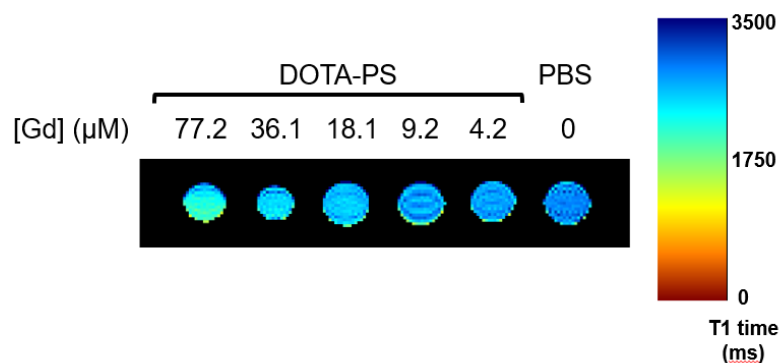
Figure 4-6. Color-coded maps of T1 times of DOTA-PS solution phantoms.
Samples are serial dilutions of DOTA-PS, and one PBS sample. Corresponding concentration of Gd is given, as measured on ICP-MS.

Interestingly, there was a gradient of signal intensities seen across individual sample cross sections, most apparent for the high concentration sample (77.2 µM Gd). Warmer signal can be observed at the bottom of the sample, as opposed to cooler signal near the top, suggesting settling of the nanocarriers at the bottom of the sample. Such settling of nanocarriers is to be expected over time, though it is surprising that this appears to be occurring in the matter of a few hours (the length of time for these MRI scans). This settling is also surprising given that these PS are relatively small, with an average diameter less than 100 nm. To minimize this settling effect in future studies, agarose gel-based phantoms could be used instead to provide a more solid sample with similarly high water content.

The r_1 relaxivity per Gd of these DOTA-PS (15 mol %) at this higher field strength (9.4 T) was found to be 1.472 L/(mmol*s), which is dramatically lower than what was measured at 1.4 T via a relaxometer. A lower r_1 was expected in general, as the relaxivity enhancing effect of slower molecular tumbling was likely negated at this higher field strength (9.4 T), leading to less T1 shortening than might be expected at lower fields (1.5 T and lower)[159, 160]. However, such a dramatic decrease in r_1 was surprising. Nevertheless, given the promising relaxivity at 1.5 T, and the observed T1 shortening at 9.4 T, I proceeded forward with further evaluation of the DOTA-PS for MRI *in vitro*.

4.3.5. Uptake and T1-weighted Imaging of DOTA-PS *in vitro*

To determine the MRI contrast enhancement of the DOTA-PS *in vitro*, DC 2.4 cells (murine DC cell line) were treated with either blank PS (displaying no DOTA peptide) or DOTA-PS (displaying the DOTA peptide at 15 mol%), at different concentrations. The nanocarrier treatment concentrations were chosen in the range of previously administered PEG-*b*-PPS

nanocarrier concentrations[38, 39]. Following treatment for 24 h, cells were harvested and pelleted in capillary tubes for MR imaging. T1-weighted images were acquired of all samples (Figure 4-7), and T1 times of these samples were also measured (Table 1).

DOTA-PS displayed positive contrast enhancement for treated cells, with brightening of the signal and concentration dependent decreases in T1 times seen at treatment concentrations down to 0.125 mg/mL PS. This data indicates that DOTA-PS are able to deliver Gd-DOTA to cells for T1 shortening contrast enhancement. Notably, the blank PS did not display any visual differences in contrast or significant shortening of T1 times of treated cells.

Additionally, as these T1-weighted images were taken of cross-sections of cell pellets, there was no obvious "settling" of samples at the bottom of the tubes. While there were variations in signal within individual samples, these are seen more randomly and can be attributed to variations in how the cells clump down into pellets, variations in cell uptake of the DOTA-PS within a sample, or differences in the T1 shortening of individual cells themselves. These findings support the utility of cell-pellet imaging as a step in assessing the contrast enhancement effect of nanocarriers for MR imaging, and further support the contrast enhancement capability of the DOTA-PS.
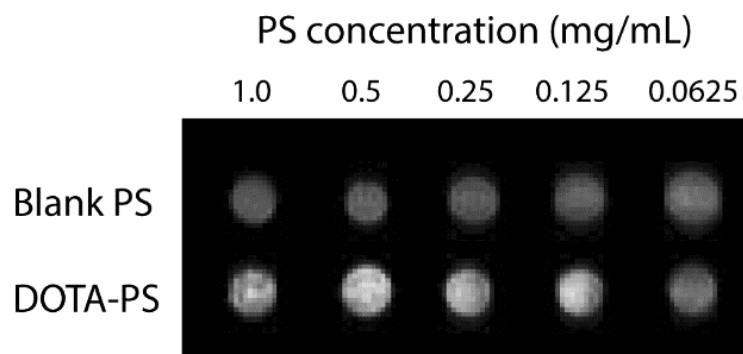
Figure 4-7. *In vitro* **MRI imaging of DOTA-PS.** T1-weighted images of DC 2.4 cells treated with blank PS or DOTA-PS (15 mol%) at different concentrations of polymer at 9.4 T.

Table 4-1. T1 times of Blank PS and DOTA-PS treated cells at 9.4 T.

Blank PS		DOTA-PS	
Polymer concentration (mg/mL)	T1 time (ms)	Polymer concentration (mg/mL)	T1 time (ms)
1	2010.53	1	604.331
0.5	1978.34	0.5	815.101
0.25	2349.18	0.25	1201.68
0.125	2087.52	0.125	1272.71
0.0625	2134.9	0.0625	2003.67

4.3.6. DOTA-PS Biodistribution and Toxicity

The organ-level biodistribution of PEG-*b*-PPS PS has been previously evaluated in mice[36, 41], demonstrating their high uptake into the liver. Here, I sought to determine whether surface display of the DOTA peptide influenced this biodistribution pattern. Additionally, I wanted to assess whether the DOTA peptide and chelated Gd would allow for ICP-MS based tracking of these nanocarriers, to provide a more sensitive and quantitative method of assessing their organ-level uptake than is possible with IVIS. Thus, similar to the MBCN biodistribution study[148], both IVIS and ICP-MS were used as orthogonal methods to assess the organ-level biodistribution of the DOTA-PS after intravenous administration in C57BL/6J mice. For IVIS, all PS groups (blank PS and DOTA-PS) were loaded with the hydrophobic near-infrared (NIR) dye 1,1-dioctadecyl-3,3,3,3-tetramethylindotricarbocyanine iodide (DiR). For ICP-MS, the level of Gd per organ sample was quantified.

DOTA-PS were found to have highest uptake into the liver via IVIS (Figure 4-8a), as compared with the spleen, kidney, and lungs, which was consistent with the blank PS distribution via IVIS in addition to previous studies with non-peptide displaying PS[36]. The distribution of the DOTA-PS as determined via ICP-MS (Figure 4-8b and c) was in strong agreement with the IVIS results, also demonstrating highest overall uptake in the liver (single μg Gd/individual organ). In contrast, ICP-MS analysis of the organs of mice treated with PBS or blank PS (Figure 4-8d and e) both showed low levels of Gd (< 1 ng Gd/individual organ), as expected given that these mice were not administered any Gd-containing formulations. ICP-MS analysis of the serum samples (Figure 4-9) showed no significant difference in the Gd content after 24 h for any of the 3 groups

(PBS, blank PS, or DOTA-PS), indicating that after 24 h the PS were likely cleared from circulation, which is expected for nanocarriers of this size range.

The similarity of the biodistribution of the DOTA-PS to the blank PS and previous studies[36, 41] demonstrates that the surface display of the DOTA peptide did not impact the *in vivo* uptake of these PS, suggesting that the dominant factor driving organ-level uptake was the nanocarrier morphology. Furthermore, the high correlation between the quantified IVIS and ICP-MS signal from organs (liver, spleen, kidneys, lungs) of mice treated with the DOTA-PS indicates that these nanocarriers are delivered intact to organs at the 24 h timepoint, with both the DiR and the DOTA peptide being delivered simultaneously.

Given the concerns of nephrotoxicity for GBCAs[154], the kidney function of these mice was important to assess. The serum creatinine levels (Figure 4-10) of these mice were found to be within normal limits[163], suggesting no nephrotoxicity at the 24 hour timepoint due to the Gd delivered via the DOTA-PS. These findings support the stability of the DOTA-PS in physiological conditions and encourages their use for diagnostic and therapeutic applications.
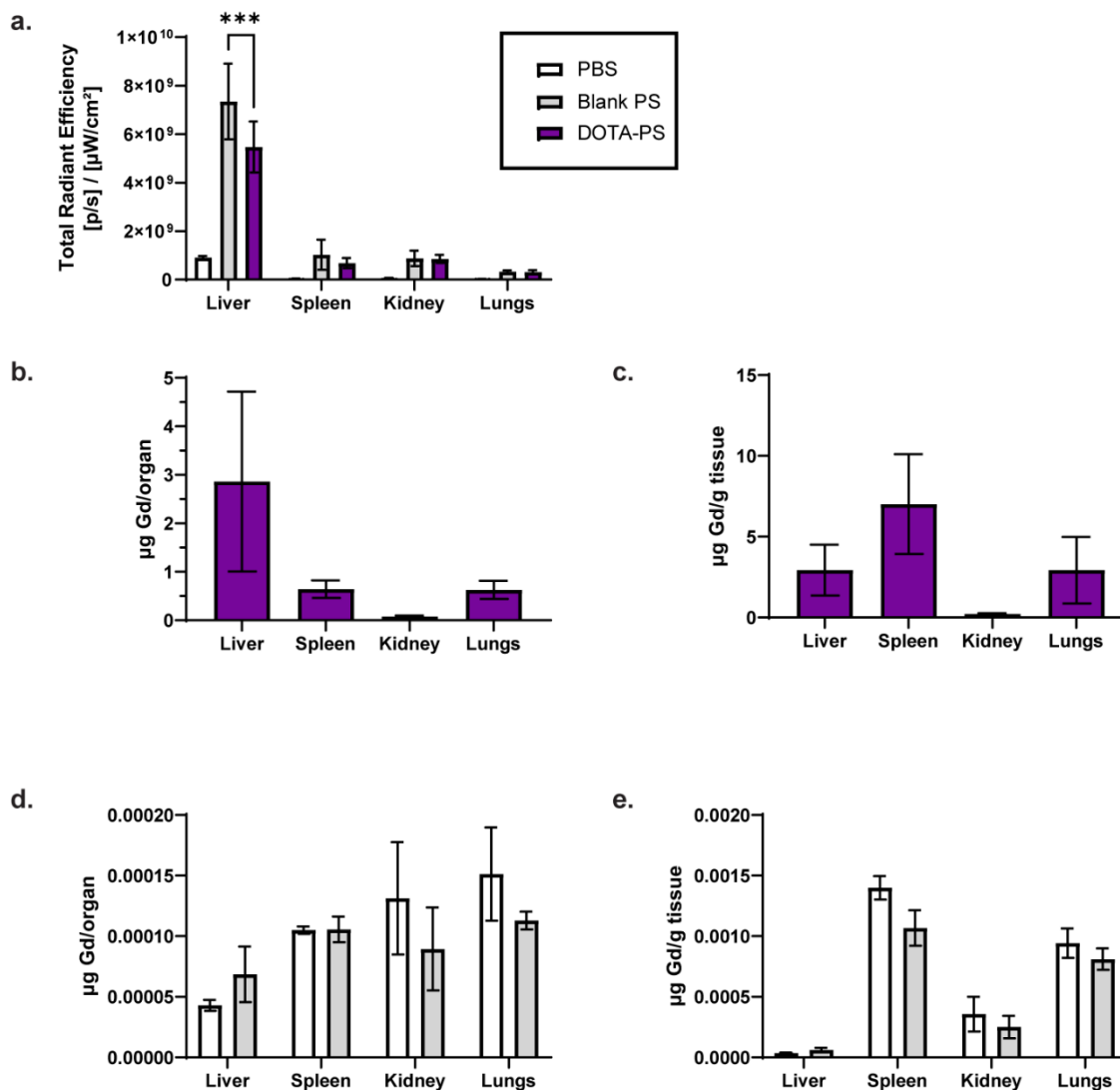
Figure 4-8. Organ-level biodistribution analysis of DOTA-PS. a) Quantification of radiant efficiency of the DiR fluorescent signal in mouse livers, spleens, kidneys, and lungs at 24 h post IV injection of PBS, blank PS, or DOTA-PS. ICP-MS analysis of organs of mice treated with DOTA-PS b) per organ or c) per g tissue at 24 h post IV injection. ICP-MS analysis of organs of mice treated with blank PS and PBS d) per organ or e) per g tissue at 24 h post IV injection. Error bars = S.D., n = 4.
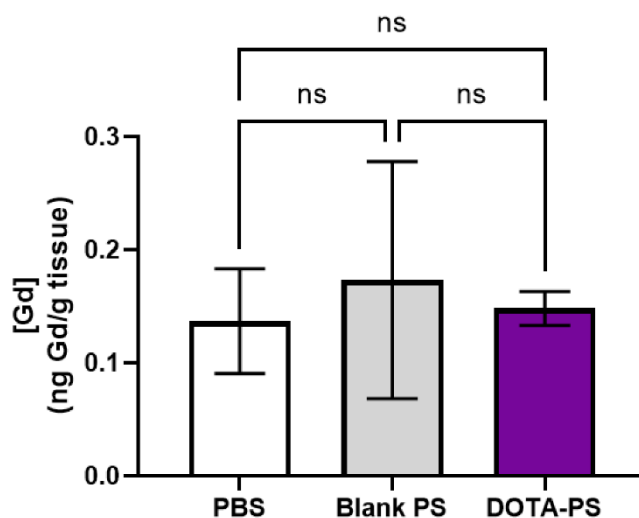
Figure 4-9. Serum Gd content of mice treated with DOTA-PS. ICP-MS analysis of the Gd content in the serum from mice treated with PBS, Blank PS, or DOTA-PS at 24 h post IV injection. Error bars = S.D., significance determined via Dunnett's multiple comparisons test, ns = not significant.
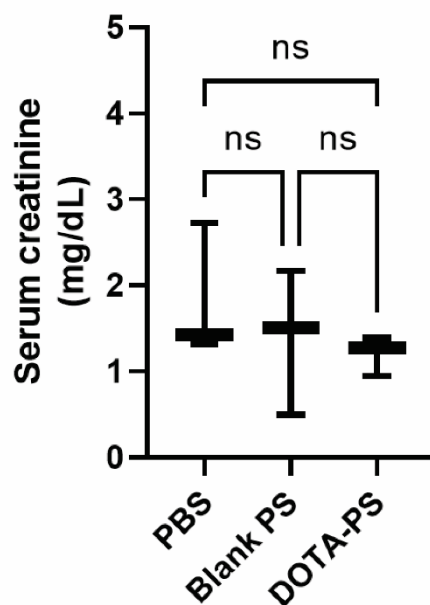
Figure 4-10. Kidney toxicity of DOTA-PS. Error bars = S.D., significance determined via Dunnett's multiple comparisons test, ns = not significant.

4.3.7. **DOTA-PS *ex vivo* MRI**

Given the ability of the DOTA-PS to enhance contrast *in vitro* and having characterized their organ-level uptake and toxicity *in vivo*, I next sought to determine their ability to enhance contrast in mouse organs post-IV administration. Only two mice were used for this preliminary study: one was administered PBS as a control, and the other was administered the DOTA-PS (15 mol %). Following IV administration, the liver, spleen, and kidney of each mouse was harvested and imaged on the 9.4 T small animal MRI scanner. Color-coded maps of the T1 times of each organ were generated (Figure 4-11a). After imaging, organs were digested and analyzed via ICP-MS to assess the Gd content of each as a measure of DOTA-PS uptake (Figure 4-11b).

As can be seen in Figure 4-11a, there was no visible difference in T1 times of the organs from PBS-treated mice (top) versus those from the DOTA-PS treated mice (bottom). This was surprising, given that there was high delivery of Gd-DOTA to the mouse organs as determined by ICP-MS (Figure 4-11b and c), at levels consistent with the previous organ-level biodistribution study (Figure 4-8). This difference and lack of T1 shortening, despite efficient delivery of Gd-DOTA via the DOTA-PS, could be explained by a few factors. First, organs and tissues are a much more complex environment than solution phantoms and cell pellets composed of a single cell type, as in the preceding DOTA-PS MRI studies. This complex background of different stromal cells, immune cells, vasculature, and other tissue components could certainly contribute to differential access to water than the DOTA-PS would have in a simpler, more homogenous background. A potential effect of this can already be seen in the intrinsic T1 times of the organs of the mice that were treated with PBS (Figure 4-11a, top 3 organs), which were around 900 ms for all 3 organs, compared with the T1 time of PBS-treated cells (Table 1), which was around 2000 ms. In these

studies, mouse organs already had a shorter T1 time than *in vitro* cells, meaning that a T1 enhancing agent would have to cause a larger drop in T1 times in organs compared with cultured cells, in order to achieve any detectable difference. This could explain why the DOTA-PS were able to enhance contrast and demonstrate T1 shortening in the cell pellets, but not in this *ex vivo* study. Finally, the relaxivity enhancing effect of slower molecular tumbling (due to the display of Gd-DOTA on the surface of a larger nanocarrier) is likely negated at this higher field (9.4 T), leading to lower T1 shortening than might be expected at lower fields (1.5 T and lower)[159].
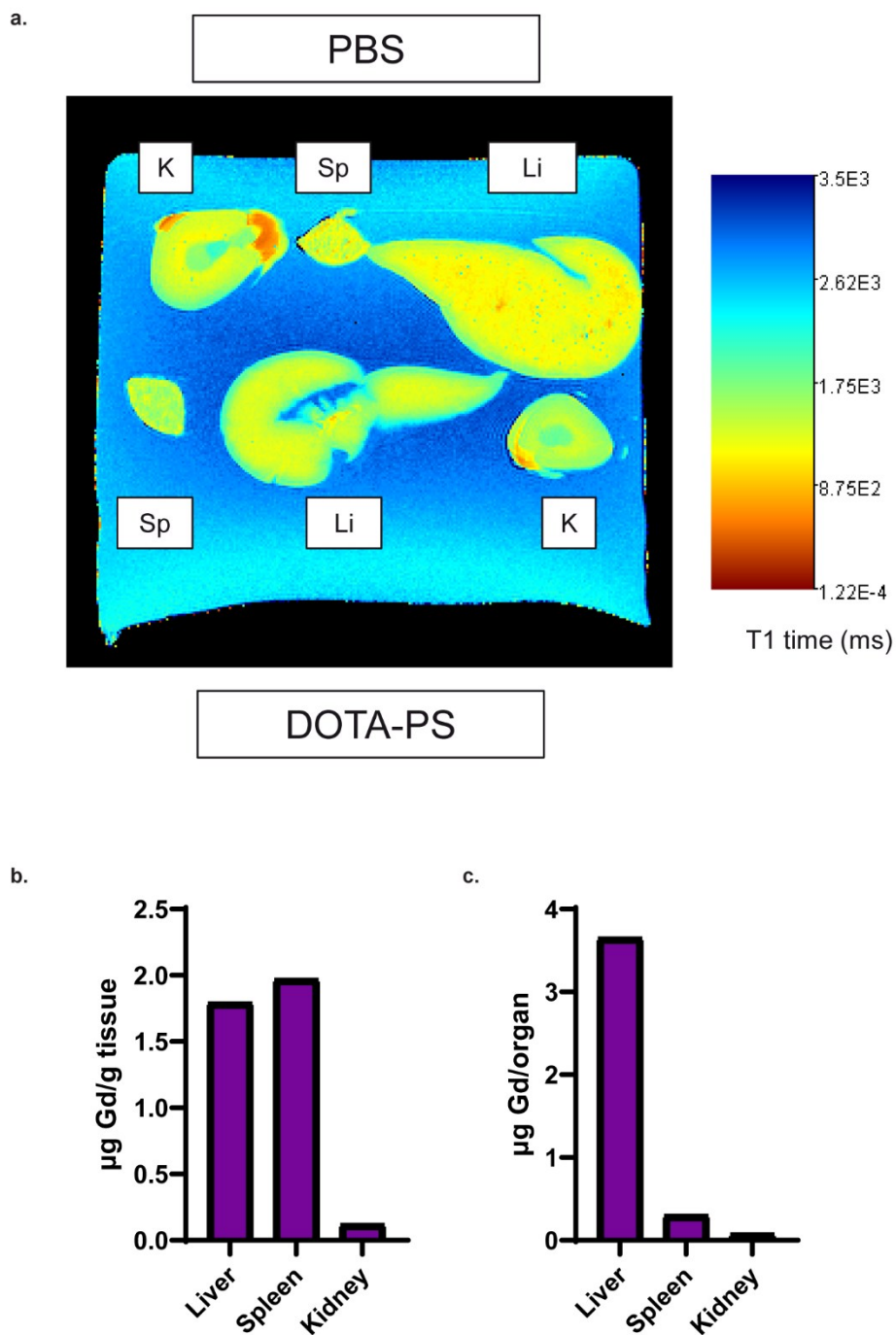
Figure 4-11. *Ex vivo* **MRI of DOTA-PS.** a) Ex vivo T1 color-coded maps of the livers (Li), spleens (Sp), and kidneys (K) of mice 24 h post IV injection with either PBS or DOTA-PS . ICP-MS analysis of the b) per g tissue and c) per organ Gd content of the liver, spleen, and kidney of a mouse treated with DOTA-PS at 24 h post IV injection.

In order to avoid this potential effect of high field MRI, the DOTA-PS were imaged at 1.5 T on a scanner dedicated for cardiovascular MRI. In this pilot study, 1 mL samples of dilutions of blank PS and DOTA-PS (15 mol %) were scanned using a T1-weighted pulse sequence. Surprisingly, there were no apparent differences in contrast seen between individual dilutions of the DOTA-PS or compared with blank PS (Figure 4-12). Currently, I have a few hypotheses for why contrast enhancement was not observed in this study, despite being observed in the previous cell pellet studies (Figure 4-7). Most importantly, the 1.5 T scanner used here is not optimal for small samples of < 5 mL volumes, as it is primarily intended for imaging the cardiovascular system in human subjects, specifically the cardiac chambers and aorta. If this were to be repeated, sample volumes greater than 1 mL could be prepared for imaging. In this case, availability of the DOTA peptide was a key limiting factor in determining sample volume and preparing formulations. In addition, the image acquisition parameters could be varied to potentially increase differences in contrast, such as by using longer scans to provide greater sensitivity. Relatively brief pulse sequences were used for this preliminary study, but more robust scans may provide better insight into the signal differences between samples.
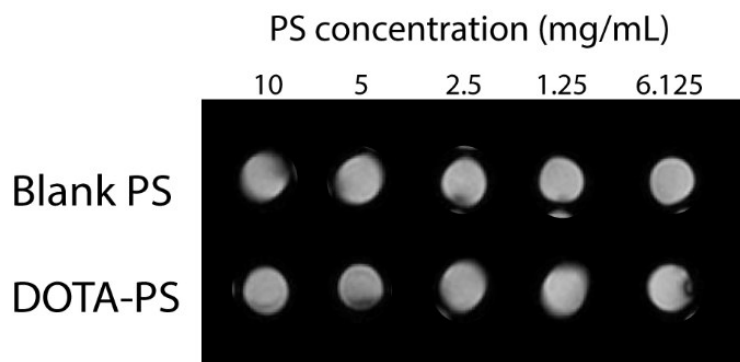
Figure 4-1*2*. MRI imaging of DOTA-PS at 1.5 T. T1-weighted images of blank PS and DOTA-PS (15 mol%) at different concentrations of polymer at 1.5 T.

Overall, while the DOTA-PS developed and discussed here (i) displayed modest r_1 relaxivity in solution as measured on a relaxometer and (ii) were able to enhance contrast *in vitro* upon cell pellet imaging, further optimization of the DOTA peptide construct will need to be done in order to improve the T1 shortening and contrast enhancement of these DOTA-PS *in vivo.* Specific ideas I have towards this goal are discussed in Chapter 5 (Future Directions).

4.3.8. Incorporation of P-D2 Dendritic Cell-targeting Peptide Construct

After designing and characterizing the DOTA peptide construct's ability to be displayed

on PEG-*b*-PPS PS membranes and characterizing the subsequent MRI signal of these DOTA-PS,
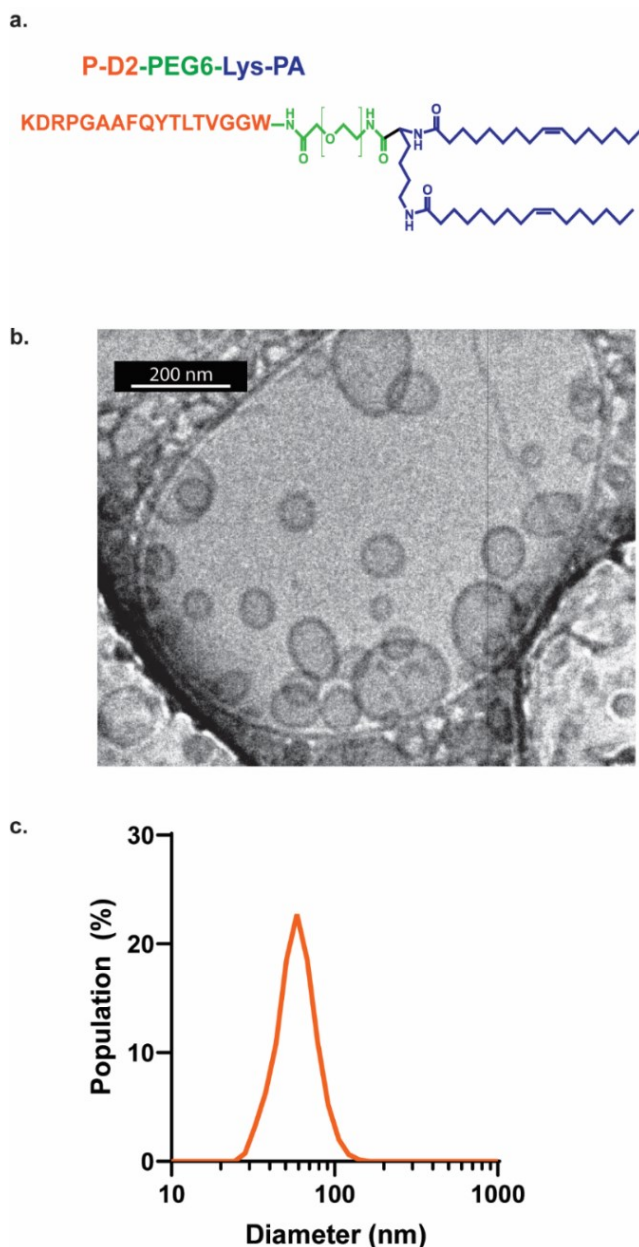
Figure 4-13. P-D2 peptide construct schematic and physicochemical characterization of P-D2-PS. a) Schematic and amino acid sequence of the P-D2 peptide construct. Chemical structure is simplified for clarity. b) Representative cryo-TEM micrograph and b) DLS size characterization of P-D2/DOTA-PS (10 mol% P-D2 peptide, 15 mol% DOTA peptide).

I next focused on addressing the broader objective of using them to assess DCs in atherosclerotic plaques. For this, I utilized the same P-D2 peptide employed by our lab previously[50] for targeting of DCs for immunotherapeutic delivery to atheromas (Figure 4-13a). This peptide construct had the same backbone of a PEG_6 linker conjugated to two molecules of palmitoleic acid, as described above and in multiple previous studies from our lab[48, 49].

First, PS were assembled and then incubated with both the DOTA peptide and P-D2 peptide constructs to form P-D2/DOTA-PS. The same 7 kDa molecular weight cutoff spin columns were used to filter out free peptide from the PS samples. Following this, cryo-TEM and DLS (Figure 4-13b and c, respectively) were used to analyze the structure and size of these dual-peptide displaying PS, and found they still retained a vesicular structure with an average hydrodynamic diameter of 86 nm.

4.3.9. Cell Uptake of P-D2- and DOTA-displaying PS

Next, the ability of the P-D2 peptide to facilitate uptake of PS into DCs was studied, using an immortalized DC cell line (DC 2.4). PS displaying increasing mol % of the P-D2 peptide construct (0-15%) were assembled from the same initial DiR-loaded PS formulation, with half of the samples also displaying the DOTA peptide construct at 15 mol%. Cells were incubated with these PS groups or PBS for 4 hours, washed, collected, and then analyzed via flow cytometry (Figure 4-14).

For PS displaying P-D2 alone (orange bars), uptake efficiency was found to increase with increasing P-D2 insertion up to 5 mol%, which is consistent with our findings from 2019[50]. Interestingly, past 10 mol % display of P-D2 peptide construct, the uptake efficiency into DC 2.4 cells actually decreased. This may be due to crowding and limited access of peptide chains with

DC 2.4 cell surface receptors as more and more peptide constructs are incorporated within PS bilayer membranes. Further studies with these targeting peptide constructs are needed to provide insight into this effect and elucidate the mechanism.

When both the P-D2 peptide construct and the DOTA peptide construct were co-displayed on PS surfaces, uptake into DC 2.4 cells was found to increase for all PS samples, regardless of mol % of P-D2 peptide. Notably, even the PS with no P-D2 display (0 mol% P-D2, 15 mol % DOTA only) had an increase in uptake efficiency from 25% with no DOTA display (0% P-D2, -DOTA) to 58% with DOTA display (0% P-D2, +DOTA). Considering all of the PS samples that the DC 2.4 cells were treated with were from the same initial formulation, this suggests that this effect of increased uptake is due to the display of the DOTA peptide construct.
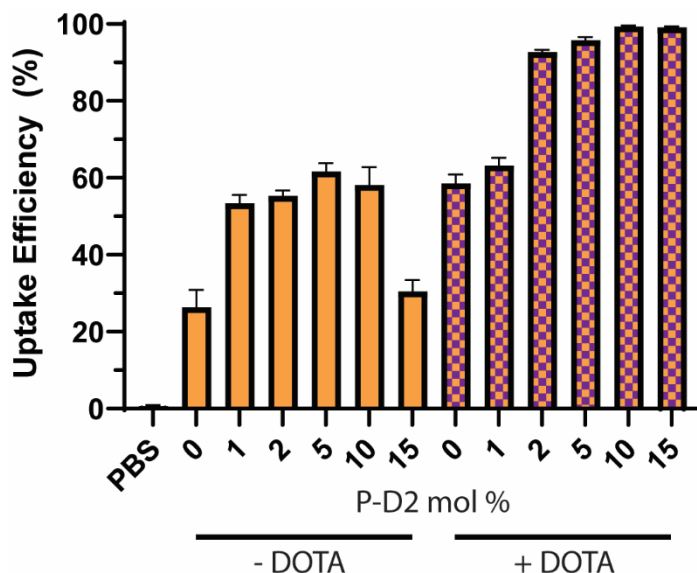
Figure 4-14. P-D2-mediated uptake of PS into DC 2.4 cells. Uptake efficiency into DC 2.4 cells of PS displaying increasing amounts of the P-D2 peptide construct with and without concurrent display of the DOTA peptide construct at 15 mol % after 4 h incubation. Error bars = S.D., n = 4.

As addition of these peptide constructs may have changed the physicochemical or surface properties of the PS such as size or surface charge, DLS and zeta potential measurements were

taken of all of the P-D2-PS and P-D2/DOTA-PS samples (Figure 4-15). While there was a general

trend of the zeta potential getting less negative with higher amounts of peptide incorporation

(Figure 4-15b), there were no significant differences in the size or surface charge of the P-D2-PS

with concurrent display of the DOTA peptide construct.
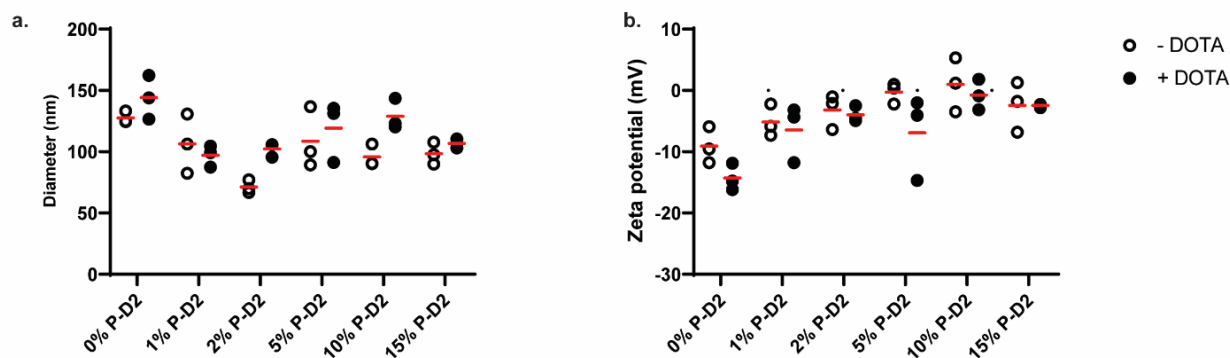
Figure 4-15. DLS and zeta potential of P-D2/DOTA-PS. a) DLS analysis and b) zeta potential of PS displaying increasing amounts of the P-D2 peptide construct with and without concurrent display of the DOTA peptide construct at 15 mol %. Red bars indicate averages of 3 independent measurements.

Currently, it is not clear why the inclusion of the DOTA peptide is enhancing *in vitro* cell

uptake in DC 2.4 cells to this degree. There are currently no reports of surface display of Gd-

DOTA being explored for cell-targeting applications or increasing cell uptake. Further *in vitro*

studies with the DOTA-PS and with PEG-*b*-PPS nanocarriers are needed to understand the

mechanism of uptake of the DOTA-PS and effects of display of non-specific peptides in general

on cell uptake.

4.3.10.   **Dendritic Cell to Macrophage Ratio in *ApoE-/-* Mice**

Given the role of both DCs and macrophages in atherosclerosis development, the ratio othese cell types was of interest as a potential metric of plaque progression. While these two cell types have both been studied for their role in plaque advancement, to the best of the Scott Lab's knowledge, the ratio between these cell types had not specifically been quantified before for its utility in staging atherosclerosis. For this work, the *ApoE-/-* mouse model was chosen as it is a very well established model for studying atherosclerosis. In these mice, deficiency of apolipoprotein E contributes to cholesterol accumulation and plaque development due to ineffective lipoprotein clearance, especially when these mice are provided a high-fat diet[164].

To study the DC to macrophage ratio, aortas and spleens from *ApoE-/-* mice that were on a high fat diet for either 3 or 6 months were harvested and processed into single cell suspensions. From the single cell suspensions, DCs and macrophages were distinguished by the following markers, as used by Busch *et al* in another recent study of DC subsets in aortas of atherosclerotic mice (*Ldlr-/-*)[89]. Specifically, the populations studied here were CD45+ CD11c+ MHCII+ DCs vs CD45+ MHCII+ CD11c− F4/80+ CD11b+ macrophages (gating in Figure 4-16). Due to high variability between counts of CD45+ immune cells collected from individual aortas and spleens, only the ratio between DCs and macrophages was a valid comparison for the studies presented here, as opposed to comparisons between absolute cell counts.
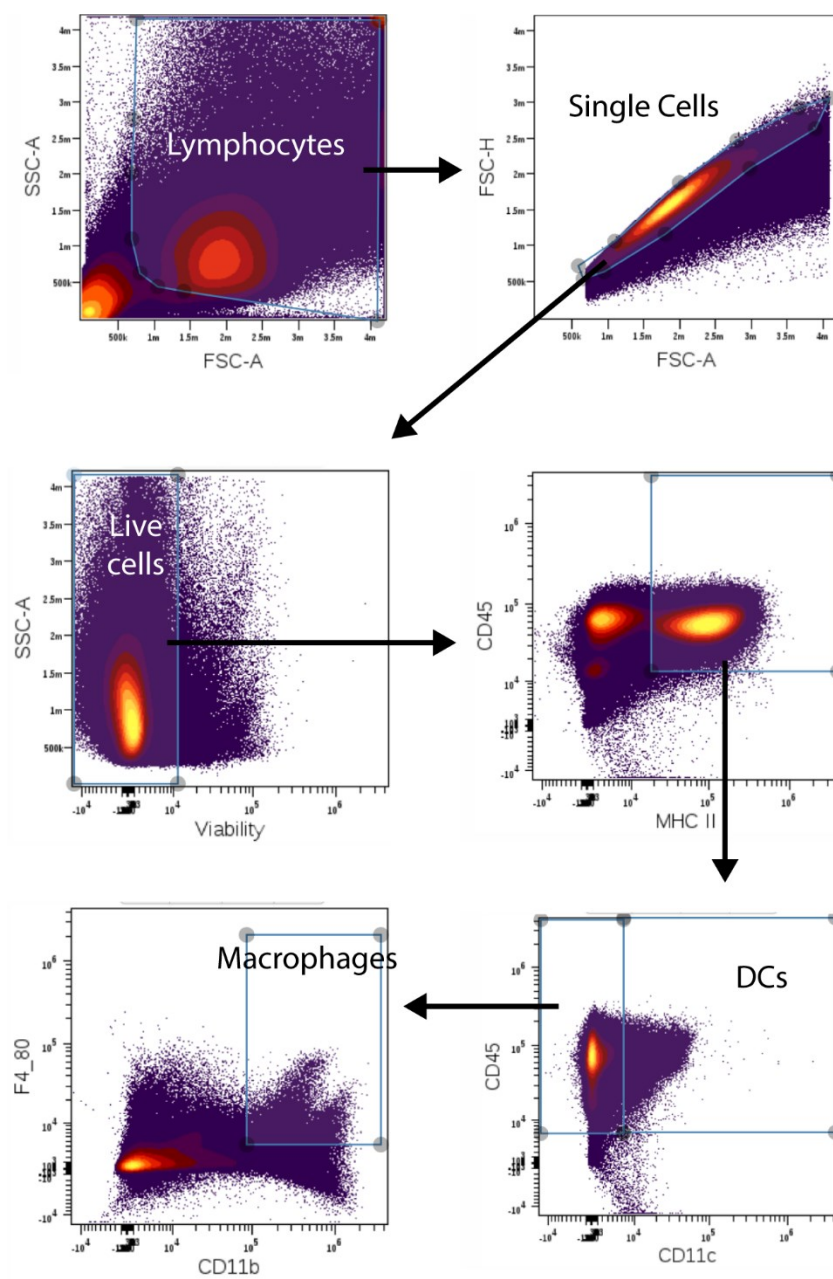
Figure 4-16. Gating strategy for DC and macrophage assessment.
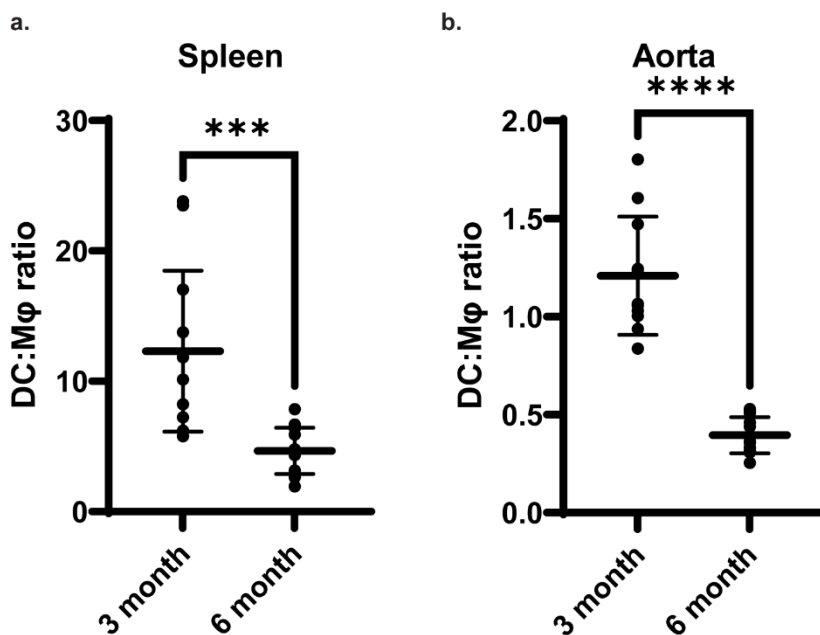
Figure 4-17. DC:Macrophage ratio in *ApoE-/-* mouse aortas and spleens at early and late stage heart disease.

Here, in this study with *ApoE-/-* mice, the DC:macrophage ratio in both spleens and aortas (Figure 4-17a and b, respectively) was found to decrease significantly with longer time on a high-fat diet (3 months vs 6 months). These results are the exact opposite of what was expected, given that generally it is known that the DC burden with atheromas increases with progression of disease[4, 5, 89]. However, these results suggest that perhaps CD45+ CD11c− MHCII+ F4/80+ CD11b+ macrophages are enhanced to a greater degree as plaques progress than the broad category of CD45+ CD11c+ MHCII+ DCs.

There are a few reasons that may be contributing to these unexpected findings. First, the *ApoE-/-* mouse model utilized here may have intrinsic differences in plaque progression that influenced these results compared with studies that utilize other mouse models. While this model is well established for studying atherosclerosis due to rapid vascular plaque formation even without

a high fat diet, it has some disadvantages that limit its comparison with other disease models[165]. Specifically, in *ApoE-/-* mice, VLDL (very low-density lipoprotein) is the primary plasma lipoprotein and cholesterol transporter as opposed to LDL in humans, which may in turn influence plaque development and immune cell activity[165]. The use of other mouse models may thus provide insight into the use of the DC:macrophage ratio as a metric of plaque progression and would be worth comparing with *ApoE-/-* model. For instance, the *Ldlr-/-* mouse model is another well-studied system for investigating atherosclerosis, as it also results in hypercholesterolemia and plaque development in mice that are provided a high fat diet. However, compared with the *ApoE-/-* model, *Ldlr-/-* mice are found to have smaller aortic fatty lesions and higher cholesterol after the same amount of time on a high fat diet, and in general require longer periods of time on a high fat diet for significant plaque development[166, 167]. While *ApoE-/-* and *Ldlr-/-* mice are by far the most commonly used mouse models for studying atherosclerosis, other models are also worth exploring for assessment of this immune cell ratio, such as mice that are deficient in both ApoE and the HDL receptor SR-B1[167].

A second reason that could explain the unexpected trend in the DC:macrophage ratio seen here is that this work focused on the broad category of CD45+ CD11c+ MHCII+ DCs, which can be further subdivided into smaller subsets that have also been explored for their role and accumulation in atherosclerotic plaques. These subsets include CD103+ and CD103- DCs, which can be further divided based on CD11b and F4/80 expression. For instance, studies have found that subpopulations of DCs including $CD103^- CD11b^+F4/80^+$, $CD11b^+F4/80^-$ and $CD11b^-F4/80^-$ DCs and $CD103^+ CD11b^-F4/80^-$ DCs all are amplified in atherosclerotic mice, specifically in *Ldlr-/-* mice, while other subpopulations like $CD103^- CD11b^- F4/80^-$ DCs are not

expanded[89]. Other studies have investigated DC burden via defining DC populations using other markers such as Fascin staining and CD83 expression in tissues from human subjects[168]. While not investigated here, characterization of various subpopulations of DCs is worth exploring in early vs late stage plaques of *ApoE-/-* mice. While the ratio of overall DCs to macrophages was found to decrease here with progression of heart disease, perhaps the ratio of certain DC subsets to macrophages may have a different relationship. For future studies, the specific subsets of $CD103^-$ $CD11b^+F4/80^+$, $CD11b^+F4/80^-$ and $CD11b^-F4/80^-$ DCs and $CD103^+$ $CD11b^-F4/80^-$ DCs and their ratio to plaque macrophages would be intriguing to assess in *ApoE-/-* mice, given their demonstrated accumulation within vulnerable plaques[89].

Finally, another variable that was different among various studies investigating immune cell populations in atherosclerosis was the length of time on a high fat diet, with some studies choosing six or twelve weeks as "early" and "late" stages of disease[89]. Overall, while multiple studies have determined the abundance of DCs within atherosclerotic plaques, particularly in vulnerable plaques, the (i) markers used to define DCs and their subsets, and (ii) the specifics of the mouse models used throughout these studies are quite variable, making comparisons between and with such studies challenging.

In addition to quantifying the DC:macrophage ratio in the *ApoE-/-* mice at early and late stages of heart disease, the ability of P-D2-PS to target these immune cell subtypes in the spleens and aortas of these mice was also assessed (Figure 4-18). In these studies, blank PS and P-D2-PS were again tagged with DiR to enable fluorescent analysis.

Here, P-D2-PS and blank PS both had significantly higher uptake in splenic macrophages compared with DCs in early and late stage disease (Figure 4-18a and b). However, P-D2 display

specifically facilitated higher uptake in both DCs and macrophages in late stage disease as compared with blank PS, though this increase was not significant. Interestingly, in mouse aortas, there was no significant difference in DC and macrophage uptake in early stage atherosclerosis for both blank PS and P-D2-PS (Figure 4-18c). Meanwhile, in mouse aortas at the late stage of atherosclerosis (Figure 4-18d), both PS groups displayed higher uptake in DCs over macrophages,
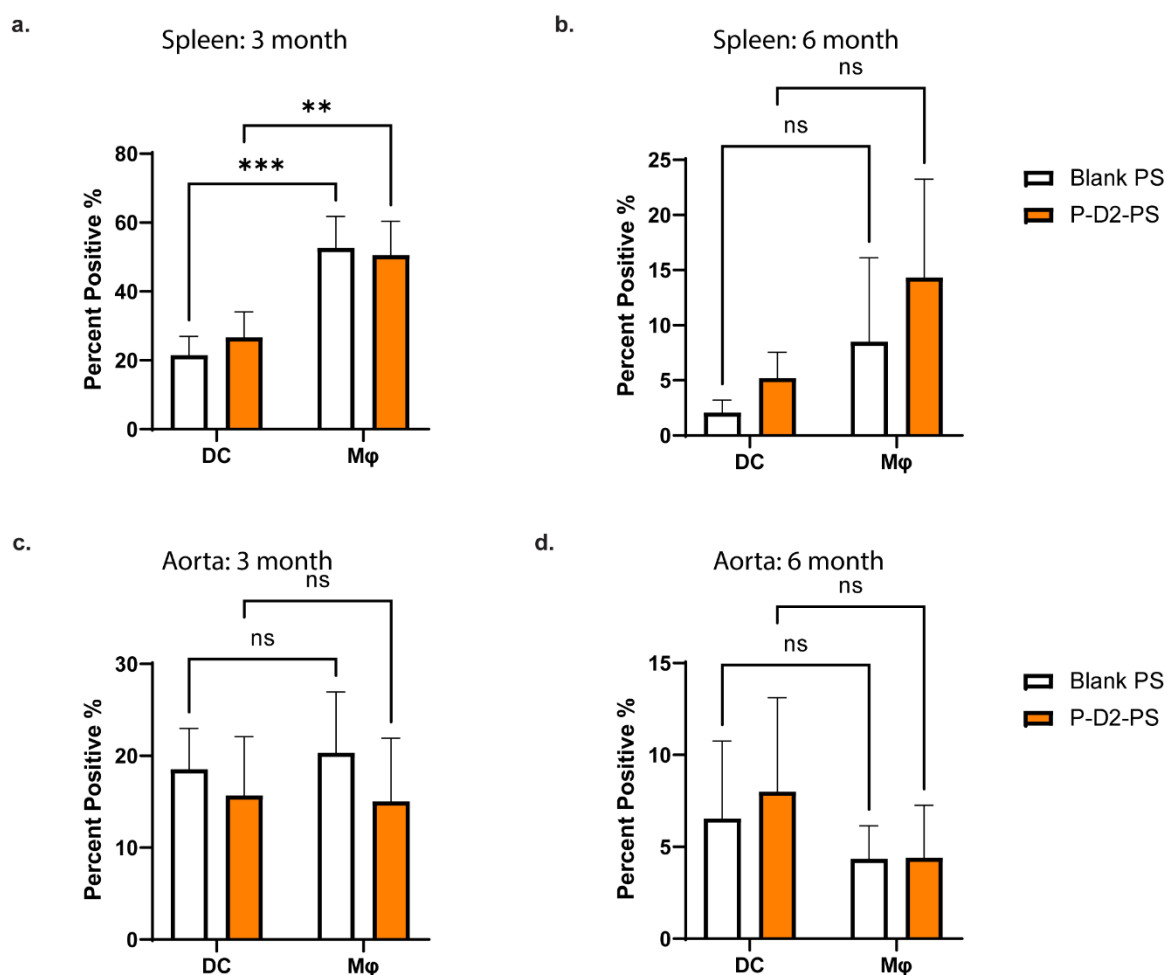
Figure 4-18. P-D2-PS uptake in in ApoE-/- mouse aortas and spleens at early and late stage heart disease. Uptake of blank PS and P-D2-PS in DCs and macrophages (Mφs) of spleens and aortas of ApoE-/- mice on a high-fat diet for 3 or 6 months. Error bars = S.D., significance determined via Dunnett's multiple comparisons test, ** $p < 0.002$, and *** $p < 0.001$, ns = not significant.

though not to a significant degree. Notably, P-D2-PS achieved higher uptake than blank PS in aortic DCs at this 6 month timepoint, though this was also not statistically significant.

Overall, these results are quite different with those from Yi *et al,* in which P-D2-PS were found to increase uptake in DCs of mice at early stages of atherosclerosis (2 months high fat diet) in both aortas and spleens[50]. However, key differences exist between these studies that could contribute to these differences in results. First, a key difference is the difference in mouse model as discussed above, as *ApoE-/-* mice were used here as opposed to *Ldlr-/-* mice, which may contribute to slightly different immune cell activity in the context of heart disease. Additionally, in this study DCs were defined as CD45+ CD11c+ MHCII+, while Yi *et al.* further specified DC subsets using CD103 staining. Furthermore, in this study the PS used were on the smaller side with an average hydrodynamic diameter of 86 nm, as opposed to the PS used by Yi *et al.* that were closer to 150 nm. Given the importance of nanocarrier size on organ and cellular uptake[36, 41], this last factor may be a key contributor to the unexpected uptake results seen here. Overall, while P-D2-PS did demonstrate moderate DC targeting in late stage atherosclerosis (Figure 4-18b), further studies are needed to determine the exact effect of P-D2 on facilitating uptake into DCs at varying stages of heart disease in *ApoE-/-* mice, focusing on more specific DC subsets as discussed above since these subsets may play a larger role in the development of plaques than DCs globally.

4.4. Materials and Methods

4.4.1. Synthesis of DOTA and P-D2 Peptide Constructs

DOTA peptide ((Palmitoleic acid)$_2$-K-(PEG$_6$)-K(DOTA)-GG-K(DOTA)-GG-K(DOTA)) and P-D2 peptide ((Palmitoleic acid)$_2$-K-PEG$_6$-WGGVTLTYQFAAGPRDK) were synthesized by

standard fluorenylmethoxycarbonyl (Fmoc) solid-phase peptide synthesis using a Liberty Blue Microwave Assisted Peptide Synthesizer on rink amide resin. Automated coupling reactions were performed using 4 equiv. Fmoc-protected amino acid, 4 equiv. of *N,N'*-diisopropylcarbodiimide (DIC), and 8 equiv. ethyl(hydroxyimino)cyanoacetate (Oxyma pure). Removal of the Fmoc groups was achieved with 20% 4-methylpiperidine in dimethylformamide (DMF). This was done for standard amino acids K(Mtt)GGK(Mtt)GGK(Mtt) and WGGVTLTYQFAAGPRDK (Mtt is 4-methytrityl). For both peptides, (Fmoc-(PEG6), then Fmoc-K(Fmoc)-OH, and finally palmitoleic acid were added manually using 2-(1H-Benzotriazol-1-ly)-1,1,3,3,-tetramethyluronium 2 hexafluorophosphate (HBTU, 2-4 eq) and N, N-diisopropylethyleamine (DIPEA, 4-8 eq) in DMF by shaking for 3-6 h at room temperature. Next, for the DOTA peptide, the three Mtt protecting groups were removed using a solution of 3% trifluoroacetic acid (TFA) in dichloromethane (DCM, 92%) and triisopropylsilane (TIS, 5%) for 5 min at room temperature followed by washing with DCM. This process was repeated until no yellow color was observed when adding the TFA solution. To the Mtt deprotected construct, DOTA-tris-t-Bu ester (1,4,7,10 - tetraazacyclododecane - 1,4,710 - tetraacetic acid tri - tert - butyl ester) was then added (1.4 equiv. per amine) with 8 equiv. DIPEA and 1.4 equiv. PyBOP ((Benzotriazol-1-yloxy)tripyrrolidinophosphonium hexafluorophosphate) and the solution in DMF was allow to shake at room temperature for 18 h. Completed peptides were then cleaved from the resin using standard solutions of 95% TFA, 2.5% water, 2.5% TIS for 1-3 h and precipitated with cold ether. Crude peptides were purified using reverse-phase HPLC (Waters Prep 150) with a H_2O/CH_3CN gradient containing 0.1 % NH_4OH (DOTA) or 0.1% TFA (P-D2). Pooled fractions containing the desired peptides as determined by mass spectrometry were frozen and lyophilized to dryness.

Finally, the purity of lyophilized peptides was analyzed by liquid chromatography-mass spectrometry (LC-MS) on an Agilent 6520 Q-TOF LC-MS.

4.4.2. Display of Peptide Constructs in PS and Gadolinium Chelation

DOTA- and P-D2-displaying PS were prepared through addition of each peptide dissolved in DMSO at the designated molar ratios to pre-formed PS. These formulations were then placed on a shaker overnight to allow insertion of the peptide constructs into the PS bilayer membranes. For gadolinium chelation, a 1.5 molar excess of $GdCl_3$ in 0.5 M sodium acetate (pH 5.5) was added to formulations, which were then placed on a shaker for 1 hour. All formulations were then purified via Zeba Spin Desalting Columns (7K MWCO, ThermoFisher Scientific) to remove excess peptide and $GdCl_3$.

4.4.3. MRI Imaging

T1-weighted images were acquired using a 9.4T Bruker Biospec MRI System and a 1.5T Aera MRI System. T1 color-coded maps were generated via post-processing of MRI images using Matlab by fitting the signal decay of each pixel to a single exponential function.

4.4.4. *In Vitro* Assessment of PS Uptake by DC 2.4 Cells

DC 2.4 cells were seeded in each well of a 12-well plate and cultured overnight in complete RPMI. DiR-loaded, peptide-displaying PS were added to each well (5 mg/mL in PBS, 100 μL) and incubated for 4 h. Cells were then washed three times and collected in 1X PBS for flow cytometric analysis. Samples were stained with Zombie Aqua (live/dead stain) and analyzed using a LSRII flow cytometer (BD Biosciences).

4.4.5. Animal Care and Use

Mice were housed and maintained at Northwestern University's Center for Comparative Medicine (CCM). All animal experiments were performed in accordance with animal protocols approved by Northwestern University's Institutional Animal Care and Use Committee (IACUC).

4.4.6. *In Vivo* Administration of PS

PS formulations (150 µL, 5 mg/mL) or controls were injected intravenously into C57BL/6J mice via the tail vein. After 24 h, 500 µL of blood was collected retro-orbitally, and mice were euthanized. Whole body perfusion via the heart was done with 3 mL of heparinized 1× PBS. Livers, spleens, and aortas were collected for imaging, flow cytometry, and ICP-MS analysis.

4.4.7. Quantifying Organ Level Distribution of Nanocarriers

Livers, spleens, and aortas were imaged using an IVIS spectrum *in vivo* imaging system (PerkinElmer, Waltham, MA). Organs were imaged using the preset filter for DiR at a 0.5 mm sample height. Living Image software was used to calculate total radiant efficiency.

Following IVIS imaging, for ICP-MS analysis, organs were digested in 3% nitric acid and 0.75% hydrogen peroxide at 65 °C overnight, and then adjusted to 50 mL of total sample volume using Milli-Q H_2O. Gadolinium content of tissues was then measured as described above using a computer-controlled Thermo iCapQ ICP-MS.

4.4.8. Measurement of Immune Cell Biodistributions

After IVIS imaging, for flow cytometric analysis, single cell suspensions were prepared from livers, spleens, and aortas as described previously.[36] Cells were first stained with anti-mouse CD16/CD32 to block FcRs and Zombie Aqua fixable viability dye. Following this, cells were

washed and then stained with a cocktail of fluorophore-conjugated anti-mouse antibodies (Supporting Information). Flow cytometry was performed with Cytek Aurora spectral flow cytometer and data were analyzed with FlowJo software.

CHAPTER 5

5. Concluding Remarks and Future Directions

5.2. Concluding Remarks

The focus of this thesis was to explore the diagnostic potential of PEG-*b*-PPS nanocarriers via their development for delivery of MRI contrast agents in the context of targeted imaging of atherosclerotic CVD. Towards this aim, I have (i) developed and characterized the novel MBCN nanocarrier, consisting of metal ferrite MNS-encapsulated PEG-*b*-PPS BCNs, and (ii) engineered PEG-*b*-PPS PS to generate T1 MRI contrast through the incorporation of Gd-DOTA via a surface-displayed peptide construct.

5.2.1. Development of MNS-encapsulated PEG-*b*-PPS Nanocarriers

While the delivery of small molecule cargo via PEG-*b*-PPS nanocarriers has been demonstrated previously, the encapsulation of nanoscale cargo and of metal ferrite MNS specifically had not been explored. Here, I found that 4 nm oleic-acid functionalized MNS could be encapsulated within PEG-*b*-PPS micelles, polymersomes, and bicontinuous nanospheres using the rapid and easy method of flash nanoprecipitation to form MMCs, MPSs, and MBCNs, respectively. I found that MBCNs displayed the most efficient MNS encapsulation and focused on them for in-depth characterization. My findings demonstrated the high potential of the MBCNs for multicargo delivery both *in vitro* and *in vivo*, along with the potential for sustained delivery applications due to their oxidation responsiveness. However, while the MBCNs proved to be superior to free hydrophilic MNS in terms of their r_2 relaxivity in solution, this did not translate to contrast enhancement in an *ex vivo* study in MBCN-treated mice. Therefore, the novel nanocarrier

of MBCNs will need to be optimized further for diagnostic applications but has utility for controlled drug delivery applications.

5.2.2. Thermal Activation of MNS-encapsulated PEG-*b*-PPS Nanocarriers

While metal ferrite MNS have been previously explored and optimized for thermal activation, or the ability to generate heat via an external radiofrequency (RF) field[26], their efficacy depends on their surface properties and interaction with their surrounding environment, which are both expected to change upon encapsulation within polymeric delivery vehicles. Thus, characterization of the thermal activation properties of the newly developed MNS-encapsulated PEG-*b*-PPS nanocarriers presented in Chapter 2 was needed. Here, I assessed the ability of MNS-encapsulated PEG-*b*-PPS micelles (MMCs) and bicontinuous nanospheres (MBCNs) to be thermally activated for triggered drug release and cancer cell death applications. I found that MMCs and MBCNs could be thermally activated to generate increases in bulk sample temperature, but that this temperature did not reach levels classically needed for induction of apoptosis. Additionally, I found that thermal activation of MNS-encapsulated PEG-*b*-PPS nanocarriers was not sufficient to trigger release of co-encapsulated anticancer agents, but that it could induce cancer cell death in cells treated with PEG-*b*-PPS nanocarriers encapsulated with MNS only or MNS plus an anticancer agent. Overall, the thermal activation studies of MNS-encapsulated PEG-*b*-PPS nanocarriers were largely inconsistent, with high variability even within repeated trials of the same formulation, suggesting the need for optimization of thermal activation parameters in addition to formulization optimization of MNS-encapsulated PEG-*b*-PPS nanocarriers, which is discussed later in this chapter.

5.2.3.   Magnetic Targeting

Magnetically responsive nanocarriers have great promise for magnetically guided delivery, particularly in the context of cancer targeting. Given that MNS-encapsulated PEG-*b*-PPS nanocarriers should be magnetically responsive due to their MNS cargo, I explored the magnetic manipulation of MBCNs in a pilot study. I found that MBCNs could accumulate locally within an agarose gel via an externally applied magnetic field. These promising findings support the further study of MNS-encapsulated PEG-*b*-PPS nanocarriers for magnetic guidance applications.

5.2.4.   DOTA- and P-D2-displaying PS for T1 MRI and CVD Targeting

Having explored the delivery of T2 MRI contrast agents via PEG-*b*-PPS nanocarriers, I also explored the incorporation and delivery of T1-enhancing agents, specifically focusing on Gd-DOTA display on PS surfaces via a lipid tail construct. I successfully demonstrated the assembly of these DOTA-PS, showing that they could enhance r_1 relaxivity in solution as compared with free Gd-DOTA, and that they could enhance T1 MRI contrast *in vitro*. Furthermore, I proved that the inclusion of the DOTA peptide construct allowed for quantitative tracking of these DOTA-PS *in vivo* via ICP-MS, and that display of the DOTA peptide construct did not alter the organ-level biodistribution of these PS. Finally, I characterized the effect of co-display of the P-D2 DC-targeting peptide on the cell uptake of DOTA-PS, as well as its ability to achieve PS uptake in mouse aortas and spleens at early and late stages of heart disease. In this study, I also characterized the DC:macrophage ratio at early and late stages of heart disease, finding that this ratio was surprisingly decreased in *ApoE-/-* mice in late stage heart disease compared with early stage. Overall, DOTA-PS are promising nanocarriers for enhancing T1 MRI contrast *in vitro*, but further

studies are needed before applying them to *in vivo* applications, such as staging atherosclerotic heart disease.

5.3.   Future Directions

The work I have discussed here in this thesis is an expansion of the current applications of PEG-*b*-PPS nanocarriers, demonstrating that they can be engineered for diagnostic applications and molecular imaging via stable encapsulation of MRI contrast agents. Along the way, my work raised questions that I did not have time to pursue or that were outside the scope of this work. I have outlined these areas of future work here, in the hopes that future members of the Scott Lab and other groups may pursue them in the effort to expand the diagnostic applications of PEG-*b*-PPS nanocarriers even further.

5.3.1.   MNS Encapsulation within Other PEG-*b*-PPS Nanocarrier Morphologies

While I focused on the encapsulation of metal ferrite MNS within three specific PEG-*b*-PPS morphologies (MCs, PSs, BCNs) in this work, other nanocarrier morphologies have been developed within the Scott Lab in recent years that would be intriguing to assess for MNS delivery. Wormlike filomicelles (FMs) are one such example, demonstrating utility for sustained delivery applications, as they possess long systemic circulation times and can undergo "cylinder-to-sphere" morphological transitions into MCs[32, 37]. Recently, PEG-*b*-PPS FMs have been extensively characterized by Nicholas Karabin[37], and FMs composed of PEG-*b*-PPS mixed with pi-stacking perylene bisimide (PBI) have been developed by Sophia Li. These mixed PBI-containing FMs (mPBI-FMs) have enhanced stability as compared with traditional PEG-*b*-PPS FMs. A study comparing the encapsulation of MNS within traditional FM and mPBI-FM would be very interesting and could potentially provide additional valuable nanocarrier platforms for MNS

delivery. Additionally, it would be intriguing to assess if MNS-encapsulated PEG-*b*-PPS FM and mPBI-FM could transition into MNS-encapsulated micellar nanocarriers in oxidative environments, and what those newly formed structures would look like.

5.3.2.   Oxidation Sensitivity of MNS-encapsulated PEG-*b*-PPS Nanocarriers

In this work, I described my findings and characterization of the oxidation-driven transition in morphology of MBCNs to MMCs (Chapter 2). I explored this transition at one specific nanocarrier concentration over time (up to 24 h) in solution. To expand on this work, the effect of varying other parameters on MBCN oxidation could be studied, such as changing the nanocarrier:peroxide concentration ratio, exploring this oxidative transition *in vitro* and *in vivo*, and varying the amount of encapsulated MNS within the MBCNs.

Here, I employed a very high concentration of hydrogen peroxide in order to demonstrate the MBCN to MMC transition as a proof of concept. Specifically, such a high concentration of peroxide was chosen in order to maximize the transition from MBCNs to MMCs and provide enough MMCs to assess via DLS and visualize on cryo-TEM. Now that this oxidation-mediated transition of MBCNs has been established, exploring this at a lower, more physiologic concentration of hydrogen peroxide would provide insight into what may occur *in vitro* or *in vivo* in oxidative environments.

Additionally, exploring whether this transition of MBCNs is occurring intracellularly upon uptake into cells is another question that I had, but was unable to answer due to limitations of imaging methods. Specifically, I demonstrated that MBCNs were internalized within intracellular vesicles upon *in vitro* uptake (Chapter 2, Figure 2-13), appearing as bright white punctae and clusters upon scanning TEM. While these bright white features were confirmed to be largely iron-

based via EDS elemental mapping suggesting that they were MNS overall, I was curious if these features truly represented MBCNs, if they had transitioned into MMCs intracellularly, or if they were simply free MNS released from within the MBCNs. However, this was unable to be determined visually from the TEM images given the resolution limits of this microscopy method. Currently, my hypothesis is that the smaller, individual bright white punctae represent oxidized MBCNs (MMCs) while the larger white features represent intact MBCNs. While this cannot currently be assessed, perhaps this is a question that can be answered as microscopy methods continue to advance as it would provide key insight into the *in vitro* oxidation of MBCNs.

Another variable that I did not explore that may influence the oxidative transition of MBCNs to MMCs is the initial ratio of encapsulated MNS to PEG-*b*-PPS polymer. Given my findings that higher encapsulation of MNS within MBCNs leads to larger MNS aggregates within individual MBCNs, I would hypothesize that MBCNs with a higher weight % of MNS would transition to larger MMCs. This could be explored in the future with a systematic assessment of MBCNs loaded with a range of MNS by weight %, followed by oxidation studies, DLS, and cryo-TEM.

Finally, as traditional BCNs have recently been found to form a depot when injected subcutaneously, it would be interesting to assess if MBCNs also have this capability. If so, given their oxidation responsiveness, the ability of MBCNs to transition to MMCs *in vivo* would be fascinating to assess and very exciting for sustained delivery applications.

5.3.3.   Magnetic Targeting of MNS-encapsulated PEG-*b*-PPS Nanocarriers

Magnetic guidance is an intriguing strategy for the enhancement of magnetic cargo at target sites via an external magnetic field. I explored the magnetic field responsiveness of MBCNs in a

very preliminary study, demonstrating enhanced accumulation of MBCNs within an agarose gel via an external magnet (Chapter 3, Figure 3-8). Based on the promising results from that pilot study, exploring the magnetic manipulation of MBCNs along with other MNS-encapsulated PEG-*b*-PPS nanocarriers would be worth exploring. Variables such as MNS encapsulation %, overall PS concentration, duration of magnetic field exposure, and strength of the external magnetic field need to be assessed to provide the optimal parameters for magnetic guidance. Following such optimization, a very fascinating study would be to assess the ability of an external magnetic field to modulate the biodistribution of MBCNs. In the Scott Lab, we currently have a mouse model of melanoma, which could be used to assess tumor accumulation of MBCNs with and without the presence of an external magnet near the tumor site, as demonstrated with other nanocarrier systems[147].

5.3.4.   Optimization of the DOTA peptide Construct for Molecular Imaging

In this work, I have engineered PEG-*b*-PPS PS to provide T1 MRI contrast enhancement through surface-display of Gd-DOTA via a lipid tail construct. Specifically, I found that the DOTA-PS had modest r_1 relaxivity in solution as measured on a relaxometer and were able to enhance contrast *in vitro* upon cell pellet imaging, but were unable to induce T1 shortening and contrast enhancement *in vivo*. These findings and the performance of the DOTA-PS for MRI contrast enhancement could perhaps be improved by further optimization of the DOTA peptide construct, as in this work I focused only on one lipid tail construct design as a proof of concept.

In terms of optimizing the DOTA peptide construct, there are three components of the lipid tail construct that could be modulated: the lipid tail, the PEG spacer, and the KGGKGGK peptide sequence itself. Altering these latter two components and the subsequent effect on DOTA-PS

relaxivity and T1 shortening would be most intriguing to assess. Specifically, varying the PEG spacer length is a key strategy for modulating the display of the peptide portion of these lipid tail constructs on nanocarrier surfaces, which is an area of research being explored by Michael Vincent[51]. Different PEG spacer lengths should theoretically lead to different interactions of the DOTA-PS with water molecules in bulk solution, as the DOTA peptide will be either buried within the PEG corona with shorter PEG spacers or exposed above it with longer PEG spacers. The effect of this on the subsequent r_1 relaxivity and T1 shortening will be important to assess in future studies with the DOTA-PS. Perhaps a PEG6 spacer as chosen in my work is not the optimal PEG spacer length for the DOTA peptide construct and subsequent contrast enhancement, despite success of this spacer length with display of other peptide constructs like P-D2 on PS bilayer membranes[50].

Another approach to optimize the DOTA peptide construct would be to modify the short peptide sequence used to conjugate the three DOTA molecules. Here, a linear peptide sequence of KGGKGGK was used in order to provide multiple Gd per peptide construct and therefore more Gd per nanocarrier, as this has been demonstrated to increase overall contrast enhancement[21]. However, aside from increasing the overall Gd per construct, the specific way that Gd is linked to a carrier is also crucial, which future iterations of the DOTA peptide construct should consider. Specifically, it's known that Gd complexes linked in a branching fashion are more effective for enhancing contrast as compared with Gd complexes linked linearly[159]. This is thought to be due to increased isotropic rotation for Gd complexes linked to branched structures as opposed to anisotropic rotation and less rigidity of Gd complexes linked to linear structures[21, 169]. Though the Gd-DOTA is not exactly conjugated in a linear fashion in the current DOTA peptide construct, as it is conjugated to lysine sidechains, it would be worthwhile to explore the effect of incorporating

more branching overall into the DOTA peptide construct design. For example, asparagine residues could be used instead of lysine, as these each have two amines per side chain for DOTA conjugation. This would provide more of a branched structure to the peptide construct and would simultaneously double the Gd per construct. A similar effect of limiting local rotation of the DOTA peptide construct to provide enhanced contrast would be to attach it somehow at two points to the PS surface, with the short peptide serving as a bridge between two separate lipid tails. This strategy of multilocus binding has been shown to be successful for improving relaxivity and contrast enhancement for Gd bound to the surface of large proteins through increased rigidity[162].

For all of these approaches and modifications to the DOTA peptide construct, an additional step of measuring the field-dependent r_1 relaxivity of the resulting DOTA-PS should be assessed using the technique of nuclear magnetic relaxation dispersion (NMRD)[21]. This important step would allow for better prediction of how DOTA-PS may perform *in vitro* and especially *in vivo*.

Aside from optimizing the display of the DOTA peptide construct on PS, its incorporation into PEG-*b*-PPS BCNs would also be very valuable to study, given the high encapsulation efficiency of BCNs for small molecule payloads and given their unique structure of multiple intertwined bilayer membranes. Due to the presence of aqueous channels running throughout the BCN structure, there is high water access to cargo loaded even at the center of the nanocarrier, as I demonstrated in Chapter 2 with the MBCNs. BCNs should therefore be able to encapsulate and display the DOTA peptide construct very efficiently within their multiple bilayer membranes, and likely demonstrate relaxivity enhancement given the high water access throughout the nanocarrier. However, for this strategy the length of the PEG spacer and the overall DOTA peptide construct would need to first be optimized for incorporation into BCNs.

Finally, while the DOTA-PS were used here for MRI via chelation of Gd(III), DOTA has the ability to chelate other ions as well, which could be leveraged for the incorporation of radioactive elements for another molecular imaging modality: position emission tomography (PET) imaging. Specifically, the radiometals Copper-64 (^{64}Cu) and Gallium-68 (^{68}Ga) have been of high interest in recent years for PET imaging[170], with DOTA-based chelators being explored for delivery of these agents. Incorporation of ^{64}Cu or ^{68}Ga via the DOTA peptide construct would greatly enhance the diagnostic potential of PEG-*b*-PPS nanocarriers as PET imaging is a highly sensitive modality compared to MRI, and it can also be combined with computed tomography (CT) to provide anatomic information. Furthermore, as PET/MRI integrated systems become more widely available, these DOTA-PS could potentially prove useful for multi-modality PET/MRI imaging through simultaneous chelation of both Gd for MRI and a PET radiotracer like ^{64}Cu or ^{68}Ga.

5.4. Curriculum Vitae

<u>Mallika Modak</u>

PERSONAL INFORMATION

mallikavmodak@gmail.com | 630-696-7080

EDUCATION

Ph.D., Northwestern University, Biomedical Engineering, *Planned June 2021*

B.S., University of Illinois at Urbana-Champaign, Bioengineering, May 2015

RESEARCH AND PROFESSIONAL EXPERIENCE

Ph.D. Candidate, Scott Lab, Northwestern University, June 2017-present

Undergraduate Researcher, Bailey Lab, University of Illinois at Urbana-Champaign, 2012-2015

AWARDS, FELLOWSHIPS & GRANTS

2018-2019, Robert H. Lurie Cancer Center Fishel Fellowship in Cancer Biology

TEACHING

Teaching Assistant, BME 344: Biologic Performance of Materials, Northwestern University, Fall 2018

PUBLICATIONS

Modak, M.; Bobbala, S.; Lescott, C.; Liu, Y.L.; Nandwana, V.; Dravid, V.P.; Scott, E.A. "Magnetic nanostructure-loaded bicontinuous nanospheres support multi-cargo intracellular delivery and oxidation-responsive morphological transitions." *ACS Applied Materials and Interfaces,* 2020. DOI: 10.1021/acsami.0c15920

Modak, M.; Frey, M. A.; Yi, S.; Liu, Y.; Scott, E. A., Employment of Targeted Nanoparticles for Imaging of Cellular Processes in Cardiovascular Disease. *Current Opinion in Biotechnology* 2020, *66*, 59-68.

Allen, S. D.; Bobbala, S.; Karabin, N.; **Modak, M.**; Scott, E. A., Benchmarking Bicontinuous Nanospheres against Polymersomes for in Vivo Biodistribution and Dual Intracellular Delivery of Lipophilic and Water Soluble Payloads. *ACS Applied Materials & Interfaces* 2018**,** *10* (40), 33857-33866.

Ostadhossein, F.; Daza, E. A.; Frankowski, D.; Goatz, D.; Imgruet, M.; Kus, J.; Lake, R.; **Modak, M.**; Olsen, N.; Schwartz-Duval, A.; Zimmer, A.; Kolmodin, N.; Pan, D., Nano-Enabled Delivery of Intracellular Therapeutics. In *Personalized Medicine with a Nanochemistry Twist: Nanomedicine*, Pan, D., Ed. Springer International Publishing: Cham, 2016; pp 105-119.

Submitted manuscripts under review:

Li, S.; Bobbala, S.; Vincent, M.P.; **Modak, M.**; Liu, Y.; Scott, E.A., Pi-stacking enhances stability, scalability of formation, control over flexibility and circulation time of polymeric filaments. *Advanced NanoBiomed Research*, 2021.

CONFERENCE PRESENTATIONS

Modak, M.; Bobbala, S.; Lescott, C.; Liu, Y.L.; Nandwana, V.; Dravid, V.P.; Scott, E.A. "Oxidation-responsive, Magnetic Nanostructure-loaded Bicontinuous Nanospheres for Drug Delivery," *Society for Biomaterials Annual Meeting*, Oral Presentation, April 23rd, 2021.

Modak, M.; Bobbala, S.; Lescott, C.; Liu, Y.L.; Nandwana, V.; Dravid, V.P.; Scott, E.A. "Oxidation-responsive, Magnetic Nanostructure-loaded Bicontinuous Nanospheres for Drug Delivery," *World Biomaterials Congress*, Poster, December 2020.

Modak, M.; Bobbala, S.; Lescott, C.; Liu, Y.L.; Nandwana, V.; Dravid, V.P.; Scott, E.A. "Oxidation-responsive, Magnetic Nanostructure-loaded Bicontinuous Nanospheres for Drug Delivery," *Biomedical Engineering Society Annual Meeting*, Oral Presentation, October 16th, 2020.

Modak, M.; Bobbala, S.; Liu, Y.L.; Nandwana, V.; Dravid, V.P.; Scott, E.A "Magnetic Nanostructure-loaded Bicontinuous Nanospheres for Magnetic Resonance Imaging and Drug Delivery," *Biomedical Engineering Society Annual Meeting*, Poster, October 17th, 2019.

M. Modak, S. Bobbala, Y. Liu, V. Nandwana, V.P. Dravid, E.A. Scott. "Magnetic Nanostructure-loaded Bicontinuous Nanospheres for Magnetic Resonance Imaging and Drug Delivery," *Society for Biomaterials Annual Meeting*, Oral Presentation, April 4th, 2019.

COMMUNITY/VOLUNTEER SERVICE

2017-2020, Northwestern MSTP, Recruitment Volunteer, screened incoming applications and guided applicants on Evanston interview days.

April 2020-May 2020, GetMePPE Chicago Volunteer, data mining and calling local Chicagoland businesses to acquire donations of PPE and other supplies for Chicago hospitals during the COVID19 pandemic.

2017-2019, WiSTEM Shadow Days Volunteer, high school mentoring, Northwestern University

2016-2017, Community Health Clinics Cardiology Clinic Coordinator, Feinberg School of Medicine, organized monthly visits to treat underserved patients with cardiology concerns, trained student volunteers and recruited attending physicians before clinic.

LEADERSHIP POSITIONS

2017-2018, Phi Rho Sigma Medical Society, Secretary, organized monthly meetings and communicated society info to members.

2016-2017, Community Health Clinics Cardiology Clinic Coordinator, Feinberg School of Medicine, organized monthly visits to treat underserved patients with cardiology concerns, trained student volunteers and recruited attending physicians before clinic.

REFERENCES

1.   Mensah, G. A.; Roth, G. A.; Fuster, V., The Global Burden of Cardiovascular Diseases and Risk factors. *Journal of the American College of Cardiology* **2019,** *74* (20), 2529.

2.   Miao, B.; Hernandez Adrian, V.; Alberts Mark, J.; Mangiafico, N.; Roman Yuani, M.; Coleman Craig, I., Incidence and Predictors of Major Adverse Cardiovascular Events in Patients with Established Atherosclerotic Disease or Multiple Risk Factors. *Journal of the American Heart Association* **2020,** *9* (2), e014402.

3.   Bäck, M.; Yurdagul, A.; Tabas, I.; Öörni, K.; Kovanen, P. T., Inflammation and Its Resolution in Atherosclerosis: Mediators and Therapeutic Opportunities. *Nature Reviews Cardiology* **2019,** *16* (7), 389-406.

4.   Wolf, D.; Ley, K., Immunity and Inflammation in Atherosclerosis. *Circulation Research* **2019,** *124* (2), 315-327.

5.   Subramanian, M.; Tabas, I., Dendritic Cells in Atherosclerosis. *Semin Immunopathol* **2014,** *36* (1), 93-102.

6.   Herrington, W.; Lacey, B.; Sherliker, P.; Armitage, J.; Lewington, S., Epidemiology of Atherosclerosis and the Potential to Reduce the Global Burden of Atherothrombotic Disease. *Circulation Research* **2016,** *118* (4), 535-546.

7.   Jaffer, F. A.; Libby, P.; Weissleder, R., Molecular Imaging of Cardiovascular Disease. *Circulation* **2007,** *116* (9), 1052-1061.

8.   Shaw, S. Y., Molecular Imaging in Cardiovascular Disease: Targets and Opportunities. *Nature Reviews Cardiology* **2009,** *6* (9), 569-579.

9.   Godin, B.; Sakamoto, J. H.; Serda, R. E.; Grattoni, A.; Bouamrani, A.; Ferrari, M., Emerging Applications of Nanomedicine for the Diagnosis and Treatment of Cardiovascular Diseases. *Trends Pharmacol Sci* **2010,** *31* (5), 199-205.

10.   Lavin Plaza, B.; Theodoulou, I.; Rashid, I.; Hajhosseiny, R.; Phinikaridou, A.; Botnar, R. M., Molecular Imaging in Ischemic Heart Disease. *Current Cardiovascular Imaging Reports* **2019,** *12* (7), 31.

11.   Ji, R.; Li, X.; Zhou, C.; Tian, Q.; Li, C.; Xia, S.; Wang, R.; Feng, Y.; Zhan, W., Identifying Macrophage Enrichment in Atherosclerotic Plaques by Targeting Dual-Modal Us Imaging/Mri Based on Biodegradable Fe-Doped Hollow Silica Nanospheres Conjugated with Anti-Cd68 Antibody. *Nanoscale* **2018,** *10* (43), 20246-20255.

12.   Liu, J.; Chen, Y.; Wang, G.; Lv, Q.; Yang, Y.; Wang, J.; Zhang, P.; Liu, J.; Xie, Y.; Zhang, L.; Xie, M., Ultrasound Molecular Imaging of Acute Cardiac Transplantation Rejection Using Nanobubbles Targeted to T Lymphocytes. *Biomaterials* **2018,** *162*, 200-207.

13.   Pysz, M. A.; Gambhir, S. S.; Willmann, J. K., Molecular Imaging: Current Status and Emerging Strategies. *Clin Radiol* **2010,** *65* (7), 500-516.

14.   Sanz, J.; Fayad, Z. A., Imaging of Atherosclerotic Cardiovascular Disease. *Nature* **2008,** *451* (7181), 953-957.

15.   James, M. L.; Gambhir, S. S., A Molecular Imaging Primer: Modalities, Imaging Agents, and Applications. *Physiological Reviews* **2012,** *92* (2), 897-965.

16.   Bloch, F., Nuclear Induction. *Physical Review* **1946,** *70* (7-8), 460-474.

17.   Purcell, E. M.; Torrey, H. C.; Pound, R. V., Resonance Absorption by Nuclear Magnetic Moments in a Solid. *Physical Review* **1946,** *69* (1-2), 37-38.

18.   Lauterbur, P. C., Image Formation by Induced Local Interactions: Examples Employing Nuclear Magnetic Resonance. *Nature* **1973,** *242* (5394), 190-191.

19.   Grover, V. P. B.; Tognarelli, J. M.; Crossey, M. M. E.; Cox, I. J.; Taylor-Robinson, S. D.; McPhail, M. J. W., Magnetic Resonance Imaging: Principles and Techniques: Lessons for Clinicians. *J Clin Exp Hepatol* **2015,** *5* (3), 246-255.

20.   Bradley, W. G., Mr Appearance of Hemorrhage in the Brain. *Radiology* **1993,** *189* (1), 15-26.

21.   Wahsner, J.; Gale, E. M.; Rodríguez-Rodríguez, A.; Caravan, P., Chemistry of Mri Contrast Agents: Current Challenges and New Frontiers. *Chemical reviews* **2019,** *119* (2), 957-1057.

22.   Xiao, Y.-D.; Paudel, R.; Liu, J.; Ma, C.; Zhang, Z.-S.; Zhou, S.-K., Mri Contrast Agents: Classification and Application (Review). *Int J Mol Med* **2016,** *38* (5), 1319-1326.

23.   Huang, C.-H.; Tsourkas, A., Gd-Based Macromolecules and Nanoparticles as Magnetic Resonance Contrast Agents for Molecular Imaging. *Curr Top Med Chem* **2013,** *13* (4), 411-421.

24.   Nandwana, V.; De, M.; Chu, S.; Jaiswal, M.; Rotz, M.; Meade, T. J.; Dravid, V. P., Theranostic Magnetic Nanostructures (Mns) for Cancer. Springer, Cham: 2015; pp 51-83.

25.   De, M.; Chou, S. S.; Joshi, H. M.; Dravid, V. P., Hybrid Magnetic Nanostructures (Mns) for Magnetic Resonance Imaging Applications. **2011,** *63* (14-15), 1282-1299.

26.   Nandwana, V.; Ryoo, S.-R.; Kanthala, S.; De, M.; Chou, S. S.; Prasad, P. V.; Dravid, V. P., Engineered Theranostic Magnetic Nanostructures: Role of Composition and Surface Coating on Magnetic Resonance Imaging Contrast and Thermal Activation. *ACS Applied Materials & Interfaces* **2016,** *8* (11), 6953-6961.

27.   Din, F. U.; Aman, W.; Ullah, I.; Qureshi, O. S.; Mustapha, O.; Shafique, S.; Zeb, A., Effective Use of Nanocarriers as Drug Delivery Systems for the Treatment of Selected Tumors. *International journal of nanomedicine* **2017,** *12*, 7291-7309.

28.   Akbarzadeh, A.; Rezaei-Sadabady, R.; Davaran, S.; Joo, S. W.; Zarghami, N.; Hanifehpour, Y.; Samiei, M.; Kouhi, M.; Nejati-Koshki, K., Liposome: Classification, Preparation, and Applications. *Nanoscale Res Lett* **2013,** *8* (1), 102-102.

29.   Mukherjee, S.; Ray, S.; Thakur, R. S., Solid Lipid Nanoparticles: A Modern Formulation Approach in Drug Delivery System. *Indian J Pharm Sci* **2009,** *71* (4), 349-358.

30.   Cotta, M. A., Quantum Dots and Their Applications: What Lies Ahead? *ACS Applied Nano Materials* **2020,** *3* (6), 4920-4924.

31.   Begines, B.; Ortiz, T.; Pérez-Aranda, M.; Martínez, G.; Merinero, M.; Argüelles-Arias, F.; Alcudia, A., Polymeric Nanoparticles for Drug Delivery: Recent Developments and Future Prospects. *Nanomaterials (Basel)* **2020,** *10* (7), 1403.

32.   Geng, Y.; Dalhaimer, P.; Cai, S.; Tsai, R.; Tewari, M.; Minko, T.; Discher, D. E., Shape Effects of Filaments Versus Spherical Particles in Flow and Drug Delivery. *Nature nanotechnology* **2007,** *2* (4), 249-255.

33.   Napoli, A.; Tirelli, N.; Kilcher, G.; Hubbell, A., New Synthetic Methodologies for Amphiphilic Multiblock Copolymers of Ethylene Glycol and Propylene Sulfide. *Macromolecules* **2001,** *34* (26), 8913-8917.

34.   Simona Cerritelli; Diana Velluto, a.; Jeffrey A. Hubbell*, Peg-Ss-Pps: Reduction-Sensitive Disulfide Block Copolymer Vesicles for Intracellular Drug Delivery. **2007**.

35.   Cerritelli, S.; O 'neil, C. P.; Velluto, D.; Fontana, A.; Adrian, M.; Dubochet, J.; Hubbell, J. A., Aggregation Behavior of Poly(Ethylene Glycol-Bl-Propylene Sulfide) Di-and Triblock Copolymers in Aqueous Solution. *Langmuir* **2009,** *25* (19), 11328-11335.

36.   Yi, S.; Allen, S. D.; Liu, Y.-G.; Ouyang, B. Z.; Li, X.; Augsornworawat, P.; Thorp, E. B.; Scott, E. A., Tailoring Nanostructure Morphology for Enhanced Targeting of Dendritic Cells in Atherosclerosis. *ACS Nano* **2016,** *10* (12), 11290-11303.

37.   Karabin, N. B.; Allen, S.; Kwon, H.-K.; Bobbala, S.; Firlar, E.; Shokuhfar, T.; Shull, K. R.; Scott, E. A., Sustained Micellar Delivery Via Inducible Transitions in Nanostructure Morphology. *Nature Communications* **2018,** *9* (1).

38.   Allen, S.; Osorio, O.; Liu, Y.-G.; Scott, E., Facile Assembly and Loading of Theranostic Polymersomes Via Multi-Impingement Flash Nanoprecipitation. *Journal of Controlled Release* **2017,** *262*, 91-103.

39.   Bobbala, S.; Allen, S. D.; Scott, E. A., Flash Nanoprecipitation Permits Versatile Assembly and Loading of Polymeric Bicontinuous Cubic Nanospheres. *Nanoscale* **2018,** *10* (11), 5078-5088.

40.   Bobbala, S.; Allen, S. D.; Yi, S.; Vincent, M.; Frey, M.; Karabin, N.; Scott, E., Employing Bicontinuous-to-Micellar Transitions in Nanostructure Morphology for on-Demand Photo-Oxidation Responsive Cytosolic Delivery and Off-on Cytotoxicity. *Nanoscale* **2020**.

41.   Allen, S. D.; Bobbala, S.; Karabin, N.; Modak, M.; Scott, E. A., Benchmarking Bicontinuous Nanospheres against Polymersomes for in Vivo Biodistribution and Dual Intracellular Delivery of Lipophilic and Water Soluble Payloads. *ACS Applied Materials & Interfaces* **2018,** *10* (40), 33857-33866.

42.   Vasdekis, A. E.; Scott, E. A.; O'Neil, C. P.; Psaltis, D.; Hubbell, J. A., Precision Intracellular Delivery Based on Optofluidic Polymersome Rupture. *ACS Nano* **2012,** *6* (9), 7850-7857.

43.   Yu, M. K.; Park, J.; Jon, S., Targeting Strategies for Multifunctional Nanoparticles in Cancer Imaging and Therapy. *Theranostics* **2012,** *2* (1), 3-44.

44.   Deshpande, P. P.; Biswas, S.; Torchilin, V. P., Current Trends in the Use of Liposomes for Tumor Targeting. *Nanomedicine (London, England)* **2013,** *8* (9), 1509-1528.

45.   Friedman, A. D.; Claypool, S. E.; Liu, R., The Smart Targeting of Nanoparticles. *Curr Pharm Des* **2013,** *19* (35), 6315-6329.

46.   Steinbach, J. M.; Seo, Y.-E.; Saltzman, W. M., Cell Penetrating Peptide-Modified Poly(Lactic-Co-Glycolic Acid) Nanoparticles with Enhanced Cell Internalization. *Acta biomaterialia* **2016,** *30*, 49-61.

47.   Zhao, N.; Bagaria, H. G.; Wong, M. S.; Zu, Y., A Nanocomplex That Is Both Tumor Cell-Selective and Cancer Gene-Specific for Anaplastic Large Cell Lymphoma. *Journal of nanobiotechnology* **2011,** *9*, 2-2.

48.   Stack, T.; Vincent, M.; Vahabikashi, A.; Li, G.; Perkumas, K. M.; Stamer, W. D.; Johnson, M.; Scott, E., Targeted Delivery of Cell Softening Micelles to Schlemm's Canal Endothelial Cells for Treatment of Glaucoma. *Small* **2020,** *16* (43), 2004205.

49.   Nagaraj, R.; Stack, T.; Yi, S.; Mathew, B.; Shull, K. R.; Scott, E. A.; Mathew, M. T.; Bijukumar, D. R., High Density Display of an Anti-Angiogenic Peptide on Micelle Surfaces Enhances Their Inhibition of Avβ3 Integrin-Mediated Neovascularization in Vitro. *Nanomaterials* **2020,** *10* (3).

50.   Yi, S.; Zhang, X.; Sangji, M. H.; Liu, Y.; Allen, S. D.; Xiao, B.; Bobbala, S.; Braverman, C. L.; Cai, L.; Hecker, P. I.; DeBerge, M.; Thorp, E. B.; Temel, R. E.; Stupp, S. I.; Scott, E. A., Surface Engineered Polymersomes for Enhanced Modulation of Dendritic Cells During Cardiovascular Immunotherapy. *Advanced Functional Materials* **2019,** *29* (42), 1904399.

51.   Vincent, M. P.; Stack, T.; Vahabikashi, A.; Li, G.; Perkumas, K. M.; Ren, R.; Gong, H.; Stamer, W. D.; Johnson, M.; Scott, E. A., Surface Engineering of Flt4-Targeted Nanocarriers Enhances Cell-Softening Glaucoma Therapy. *bioRxiv* **2021**, 2021.05.19.444878.

52.   Shen, Z.; Wu, A.; Chen, X., Iron Oxide Nanoparticle Based Contrast Agents for Magnetic Resonance Imaging. *Molecular Pharmaceutics* **2017,** *14* (5), 1352-1364.

53.   Makino, A.; Kimura, S., Solid Tumor-Targeting Theranostic Polymer Nanoparticle in Nuclear Medicinal Fields. *The Scientific World Journal* **2014,** *14*.

54.   Mariano, R. N.; Alberti, D.; Cutrin, J. C.; Geninatti Crich, S.; Aime, S., Design of Plga Based Nanoparticles for Imaging Guided Applications. *Molecular Pharmaceutics* **2014,** *11* (11), 4100-4106.

55.   Xia, Y.; Xu, C.; Zhang, X.; Ning, P.; Wang, Z.; Tian, J.; Chen, X., Liposome-Based Probes for Molecular Imaging: From Basic Research to the Bedside. *Nanoscale* **2019,** *11* (13), 5822-5838.

56.   Neuwelt, A.; Sidhu, N.; Hu, C.-A. A.; Mlady, G.; Eberhardt, S. C.; Sillerud, L. O., Iron-Based Superparamagnetic Nanoparticle Contrast Agents for Mri of Infection and Inflammation. *American Journal of Roentgenology* **2015,** *204* (3), W302-W313.

57.   Man, F.; Gawne, P. J.; T.M. de Rosales, R., Nuclear Imaging of Liposomal Drug Delivery Systems: A Critical Review of Radiolabelling Methods and Applications in Nanomedicine. *Advanced Drug Delivery Reviews* **2019,** *143*, 134-160.

58.   Cheng, K.; Shen, D.; Hensley, M. T.; Middleton, R.; Sun, B.; Liu, W.; De Couto, G.; Marbán, E., Magnetic Antibody-Linked Nanomatchmakers for Therapeutic Cell Targeting. *Nature communications* **2014,** *5*, 4880-4880.

59.   Chhour, P.; Naha, P. C.; O'Neill, S. M.; Litt, H. I.; Reilly, M. P.; Ferrari, V. A.; Cormode, D. P., Labeling Monocytes with Gold Nanoparticles to Track Their Recruitment in Atherosclerosis with Computed Tomography. *Biomaterials* **2016,** *87*, 93-103.

60.   Allen, S.; Liu, Y.-G.; Scott, E., Engineering Nanomaterials to Address Cell-Mediated Inflammation in Atherosclerosis. *Regenerative Engineering and Translational Medicine* **2016,** *2* (1), 37-50.

61.   Chhour, P.; Cheheltani, R. e.; Naha, P. C.; Litt, H. I.; Ferrari, V. A.; Cormode, D. P., Nanoparticles for Cardiovascular Imaging with Ct. In *Design and Applications of Nanoparticles in Biomedical Imaging*, Bulte, J. W. M.; Modo, M. M. J., Eds. Springer International Publishing: Cham, 2017; pp 357-384.

62.   Hu, J.; Ortgies, D. H.; Martín Rodríguez, E.; Rivero, F.; Aguilar Torres, R.; Alfonso, F.; Fernández, N.; Carreño-Tarragona, G.; Monge, L.; Sanz-Rodriguez, F.; Iglesias, M. d. C.; Granado, M.; García-Villalon, A. L.; García Solé, J.; Jaque, D., Optical Nanoparticles for Cardiovascular Imaging. *Advanced Optical Materials* **2018,** *6* (22), 1800626.

63.   Park, J. H.; Dehaini, D.; Zhou, J.; Holay, M.; Fang, R. H.; Zhang, L., Biomimetic Nanoparticle Technology for Cardiovascular Disease Detection and Treatment. *Nanoscale Horizons* **2020,** *5* (1), 25-42.

64.   Mangge, H.; Almer, G., Immune-Mediated Inflammation in Vulnerable Atherosclerotic Plaques. *Molecules* **2019,** *24*, 3072.

65.   Tarin, C.; Carril, M.; Martin-Ventura, J. L.; Markuerkiaga, I.; Padro, D.; Llamas-Granda, P.; Moreno, J. A.; García, I.; Genicio, N.; Plaza-Garcia, S.; Blanco-Colio, L. M.; Penades, S.; Egido, J., Targeted Gold-Coated Iron Oxide Nanoparticles for Cd163 Detection in Atherosclerosis by Mri. *Scientific Reports* **2015,** *5* (1), 17135.

66.   Ye, M.; Zhou, J.; Zhong, Y.; Xu, J.; Hou, J.; Wang, X.; Wang, Z.; Guo, D., Sr-a-Targeted Phase-Transition Nanoparticles for the Detection and Treatment of Atherosclerotic Vulnerable Plaques. *ACS Applied Materials & Interfaces* **2019,** *11* (10), 9702-9715.

67.   Zhang, L.; Tian, X. Y.; Chan, C. K. W.; Bai, Q.; Cheng, C. K.; Chen, F. M.; Cheung, M. S. H.; Yin, B.; Yang, H.; Yung, W.-Y.; Chen, Z.; Ding, F.; Leung, K. C.-F.; Zhang, C.; Huang, Y.; Lau, J. Y. W.; Choi, C. H. J., Promoting the Delivery of Nanoparticles to Atherosclerotic Plaques by DNA Coating. *ACS Applied Materials & Interfaces* **2019,** *11* (15), 13888-13904.

68.   Liang, M.; Tan, H.; Zhou, J.; Wang, T.; Duan, D.; Fan, K.; He, J.; Cheng, D.; Shi, H.; Choi, H. S.; Yan, X., Bioengineered H-Ferritin Nanocages for Quantitative Imaging of Vulnerable Plaques in Atherosclerosis. *ACS Nano* **2018,** *12* (9), 9300-9308.

69.   Li, X.; Wang, C.; Tan, H.; Cheng, L.; Liu, G.; Yang, Y.; Zhao, Y.; Zhang, Y.; Li, Y.; Zhang, C.; Xiu, Y.; Cheng, D.; Shi, H., Gold Nanoparticles-Based Spect/Ct Imaging Probe Targeting for Vulnerable Atherosclerosis Plaques. *Biomaterials* **2016,** *108*, 71-80.

70.   Cheng, D.; Li, X.; Zhang, C.; Tan, H.; Wang, C.; Pang, L.; Shi, H., Detection of Vulnerable Atherosclerosis Plaques with a Dual-Modal Single-Photon-Emission Computed Tomography/Magnetic Resonance Imaging Probe Targeting Apoptotic Macrophages. *ACS Applied Materials & Interfaces* **2015,** *7* (4), 2847-2855.

71.   Perez-Medina, C.; Binderup, T.; Lobatto, M. E.; Tang, J.; Calcagno, C.; Giesen, L.; Wessel, C. H.; Witjes, J.; Ishino, S.; Baxter, S.; Zhao, Y.; Ramachandran, S.; Eldib, M.; Sanchez-Gaytan, B. L.; Robson, P. M.; Bini, J.; Granada, J. F.; Fish, K. M.; Stroes, E. S.; Duivenvoorden, R.; Tsimikas, S.; Lewis, J. S.; Reiner, T.; Fuster, V.; Kjaer, A.; Fisher, E. A.; Fayad, Z. A.; Mulder, W. J., In Vivo Pet Imaging of Hdl in Multiple Atherosclerosis Models. *JACC Cardiovasc Imaging* **2016,** *9* (8), 950-61.

72.   Binderup, T.; Duivenvoorden, R.; Fay, F.; van Leent, M. M. T.; Malkus, J.; Baxter, S.; Ishino, S.; Zhao, Y.; Sanchez-Gaytan, B.; Teunissen, A. J. P.; Frederico, Y. C. A.; Tang, J.; Carlucci, G.; Lyashchenko, S.; Calcagno, C.; Karakatsanis, N.; Soultanidis, G.; Senders, M. L.; Robson, P. M.; Mani, V.; Ramachandran, S.; Lobatto, M. E.; Hutten, B. A.; Granada, J. F.; Reiner, T.; Swirski, F. K.; Nahrendorf, M.; Kjaer, A.; Fisher, E. A.; Fayad, Z. A.; Pérez-Medina, C.; Mulder, W. J. M., Imaging-Assisted Nanoimmunotherapy for Atherosclerosis in Multiple Species. *Science Translational Medicine* **2019,** *11* (506), eaaw7736.

73.   Wood, K. J.; Bushell, A.; Hester, J., Regulatory Immune Cells in Transplantation. *Nature Reviews Immunology* **2012,** *12* (6), 417-430.

74.	Bonnard, T.; Jayapadman, A.; Putri, J. A.; Cui, J.; Ju, Y.; Carmichael, C.; Angelovich, T. A.; Cody, S. H.; French, S.; Pascaud, K.; Pearce, H. A.; Jagdale, S.; Caruso, F.; Hagemeyer, C. E., Low-Fouling and Biodegradable Protein-Based Particles for Thrombus Imaging. *ACS Nano* **2018,** *12* (7), 6988-6996.

75.	Li, B.; Aid-Launais, R.; Labour, M.-N.; Zenych, A.; Juenet, M.; Choqueux, C.; Ollivier, V.; Couture, O.; Letourneur, D.; Chauvierre, C., Functionalized Polymer Microbubbles as New Molecular Ultrasound Contrast Agent to Target P-Selectin in Thrombus. *Biomaterials* **2019,** *194*, 139-150.

76.	Su, M.; Dai, Q.; Chen, C.; Zeng, Y.; Chu, C.; Liu, G., Nano-Medicine for Thrombosis: A Precise Diagnosis and Treatment Strategy. *Nano-Micro Letters* **2020,** *12* (1), 96.

77.	Woodside, D. G.; Tanifum, E. A.; Ghaghada, K. B.; Biediger, R. J.; Caivano, A. R.; Starosolski, Z. A.; Khounlo, S.; Bhayana, S.; Abbasi, S.; Craft, J. W.; Maxwell, D. S.; Patel, C.; Stupin, I. V.; Bakthavatsalam, D.; Market, R. V.; Willerson, J. T.; Dixon, R. A. F.; Vanderslice, P.; Annapragada, A. V., Magnetic Resonance Imaging of Atherosclerotic Plaque at Clinically Relevant Field Strengths (1t) by Targeting the Integrin A4β1. *Scientific Reports* **2018,** *8* (1).

78.	Yu, X.-H.; Fu, Y.-C.; Zhang, D.-W.; Yin, K.; Tang, C.-K., Foam Cells in Atherosclerosis. *Clinica Chimica Acta* **2013,** *424*, 245-252.

79.	Li, S.; Gou, T.; Wang, Q.; Chen, M.; Chen, Z.; Xu, M.; Wang, Y.; Han, D.; Cao, R.; Liu, J.; Liang, P.; Dai, Z.; Cao, F., Ultrasound/Optical Dual-Modality Imaging for Evaluation of Vulnerable Atherosclerotic Plaques with Osteopontin Targeted Nanoparticles. *Macromolecular Bioscience* **2020,** *20* (2), 1900279.

80.   Gao, W.; Sun, Y.; Cai, M.; Zhao, Y.; Cao, W.; Liu, Z.; Cui, G.; Tang, B., Copper Sulfide Nanoparticles as a Photothermal Switch for Trpv1 Signaling to Attenuate Atherosclerosis. *Nature Communications* **2018,** *9* (1), 231.

81.   Wei, X.; Ying, M.; Dehaini, D.; Su, Y.; Kroll, A. V.; Zhou, J.; Gao, W.; Fang, R. H.; Chien, S.; Zhang, L., Nanoparticle Functionalization with Platelet Membrane Enables Multifactored Biological Targeting and Detection of Atherosclerosis. *ACS nano* **2018,** *12* (1), 109-116.

82.   Duelen, R.; Sampaolesi, M., Stem Cell Technology in Cardiac Regeneration: A Pluripotent Stem Cell Promise. *EBioMedicine* **2017,** *16*, 30-40.

83.   Hua, P.; Wang, Y.-Y.; Liu, L.-B.; Liu, J.-L.; Liu, J.-Y.; Yang, Y.-Q.; Yang, S.-R., In Vivo Magnetic Resonance Imaging Tracking of Transplanted Superparamagnetic Iron Oxide-Labeled Bone Marrow Mesenchymal Stem Cells in Rats with Myocardial Infarction. *Mol Med Rep* **2015,** *11* (1), 113-120.

84.   Constantinides, C.; McNeill, E.; Carnicer, R.; Al Haj Zen, A.; Sainz-Urruela, R.; Shaw, A.; Patel, J.; Swider, E.; Alonaizan, R.; Potamiti, L.; Hadjisavvas, A.; Padilla-Parra, S.; Kyriacou, K.; Srinivas, M.; Carr, C. A., Improved Cellular Uptake of Perfluorocarbon Nanoparticles for in Vivo Murine Cardiac 19f Mrs/Mri and Temporal Tracking of Progenitor Cells. *Nanomedicine: Nanotechnology, Biology and Medicine* **2019,** *18*, 391-401.

85.   Qin, X.; Chen, H.; Yang, H.; Wu, H.; Zhao, X.; Wang, H.; Chour, T.; Neofytou, E.; Ding, D.; Daldrup-Link, H.; Heilshorn, S. C.; Li, K.; Wu, J. C., Photoacoustic Imaging of Embryonic Stem Cell-Derived Cardiomyocytes in Living Hearts with Ultrasensitive Semiconducting Polymer Nanoparticles. *Advanced Functional Materials* **2018,** *28* (1), 1704939.

86.   Lemaster, J. E.; Chen, F.; Kim, T.; Hariri, A.; Jokerst, J. V., Development of a Trimodal Contrast Agent for Acoustic and Magnetic Particle Imaging of Stem Cells. *ACS Applied Nano Materials* **2018,** *1* (3), 1321-1331.

87.   Lobatto, M. E.; Calcagno, C.; Millon, A.; Senders, M. L.; Fay, F.; Robson, P. M.; Ramachandran, S.; Binderup, T.; Paridaans, M. P. M.; Sensarn, S.; Rogalla, S.; Gordon, R. E.; Cardoso, L.; Storm, G.; Metselaar, J. M.; Contag, C. H.; Stroes, E. S. G.; Fayad, Z. A.; Mulder, W. J. M., Atherosclerotic Plaque Targeting Mechanism of Long-Circulating Nanoparticles Established by Multimodal Imaging. *ACS Nano* **2015,** *9* (2), 1837-1847.

88.   Ilhan, F.; Kalkanli, S. T., Atherosclerosis and the Role of Immune Cells. *World J Clin Cases* **2015,** *3* (4), 345-352.

89.   Busch, M.; Westhofen, T. C.; Koch, M.; Lutz, M. B.; Zernecke, A., Dendritic Cell Subset Distributions in the Aorta in Healthy and Atherosclerotic Mice. *PLOS ONE* **2014,** *9* (2), e88452.

90.   Frey, M.; Bobbala, S.; Karabin, N.; Scott, E., Influences of Nanocarrier Morphology on Therapeutic Immunomodulation. *Nanomedicine* **2018,** *13* (14).

91.   Wu, Y.; Yang, Y.; Zhao, W.; Xu, Z. P.; Little, P. J.; Whittaker, A. K.; Zhang, R.; Ta, H. T., Novel Iron Oxide–Cerium Oxide Core–Shell Nanoparticles as a Potential Theranostic Material for Ros Related Inflammatory Diseases. *Journal of Materials Chemistry B* **2018,** *6* (30), 4937-4951.

92.   Vangijzegem, T.; Stanicki, D.; Laurent, S., Magnetic Iron Oxide Nanoparticles for Drug Delivery: Applications and Characteristics. *Expert Opinion on Drug Delivery* **2019,** *16* (1), 69-78.

93.   Sun, C.; Lee, J.; Zhang, M., Magnetic Nanoparticles in Mr Imaging and Drug Delivery☆. *Advanced Drug Delivery Reviews* **2008,** *60* (11), 1252-1265.

94.   Anselmo, A. C.; Mitragotri, S., Nanoparticles in the Clinic. *Bioengineering & Translational Medicine* **2016,** *1* (1), 10-29.

95.   Schwenk, M. H., Ferumoxytol: A New Intravenous Iron Preparation for the Treatment of Iron Deficiency Anemia in Patients with Chronic Kidney Disease. *Pharmacotherapy* **2010,** *30* (1), 70-79.

96.   Nguyen, K.-L.; Yoshida, T.; Kathuria-Prakash, N.; Zaki, I. H.; Varallyay, C. G.; Semple, S. I.; Saouaf, R.; Rigsby, C. K.; Stoumpos, S.; Whitehead, K. K.; Griffin, L. M.; Saloner, D.; Hope, M. D.; Prince, M. R.; Fogel, M. A.; Schiebler, M. L.; Roditi, G. H.; Radjenovic, A.; Newby, D. E.; Neuwelt, E. A.; Bashir, M. R.; Hu, P.; Finn, J. P., Multicenter Safety and Practice for Off-Label Diagnostic Use of Ferumoxytol in Mri. *Radiology* **2019,** *293* (3), 554-564.

97.   Wáng, Y. X. J.; Idée, J.-M., A Comprehensive Literatures Update of Clinical Researches of Superparamagnetic Resonance Iron Oxide Nanoparticles for Magnetic Resonance Imaging. *Quant Imaging Med Surg* **2017,** *7* (1), 88-122.

98.   Kim, M.; Chen, Y.; Liu, Y.; Peng, X., Super-Stable, High-Quality Fe3o4 Dendron-Nanocrystals Dispersible in Both Organic and Aqueous Solutions. **2005,** *17* (11), 1429-1432.

99.   Zhang, T.; Ge, J.; Hu, Y.; Yin, Y., A General Approach for Transferring Hydrophobic Nanocrystals into Water. *Nano Letters* **2007,** *7* (10), 3203-3207.

100.   De Palma, R.; Peeters, S.; Van Bael, M. J.; Van den Rul, H.; Bonroy, K.; Laureyn, W.; Mullens, J.; Borghs, G.; Maes, G., Silane Ligand Exchange to Make Hydrophobic

Superparamagnetic Nanoparticles Water-Dispersible. *Chemistry of Materials* **2007,** *19* (7), 1821-1831.

101.   Aslam, M.; Schultz, E. A.; Sun, T.; Meade, T.; Dravid, V. P., Synthesis of Amine-Stabilized Aqueous Colloidal Iron Oxide Nanoparticles. *Crystal Growth & Design* **2007,** *7* (3), 471-475.

102.   Palanisamy, S.; Wang, Y.-M., Superparamagnetic Iron Oxide Nanoparticulate System: Synthesis, Targeting, Drug Delivery and Therapy in Cancer. *Dalton Transactions* **2019,** *48* (26), 9490-9515.

103.   Amstad, E.; Kohlbrecher, J.; Müller, E.; Schweizer, T.; Textor, M.; Reimhult, E., Triggered Release from Liposomes through Magnetic Actuation of Iron Oxide Nanoparticle Containing Membranes. *Nano Letters* **2011,** *11* (4), 1664-1670.

104.   Kania, G.; Kwolek, U.; Nakai, K.; Yusa, S.-i.; Bednar, J.; Wójcik, T.; Chłopicki, S.; Skórka, T.; Szuwarzyński, M.; Szczubiałka, K.; Kepczynski, M.; Nowakowska, M., Stable Polymersomes Based on Ionic–Zwitterionic Block Copolymers Modified with Superparamagnetic Iron Oxide Nanoparticles for Biomedical Applications. *Journal of Materials Chemistry B* **2015,** *3* (27), 5523-5531.

105.   Hong, G.-b.; Zhou, J.-x.; Yuan, R.-x., Folate-Targeted Polymeric Micelles Loaded with Ultrasmall Superparamagnetic Iron Oxide: Combined Small Size and High Mri Sensitivity. *International journal of nanomedicine* **2012,** *7*, 2863-2872.

106.   Roch, A.; Gossuin, Y.; Muller, R. N.; Gillis, P., Superparamagnetic Colloid Suspensions: Water Magnetic Relaxation and Clustering. **2005,** *293* (1), 532-539.

107.   Euliss, L. E.; Grancharov, S. G.; O'Brien, S.; Deming, T. J.; Stucky, G. D.; Murray, C. B.; Held, G. A., Cooperative Assembly of Magnetic Nanoparticles and Block Copolypeptides in Aqueous Media. **2003,** *3* (11), 1489-1493.

108.   Montis, C.; Castroflorio, B.; Mendozza, M.; Salvatore, A.; Berti, D.; Baglioni, P., Magnetocubosomes for the Delivery and Controlled Release of Therapeutics. **2015,** *449*, 317-326.

109.   Acharya, D. P.; Moffat, B. A.; Polyzos, A.; Waddington, L.; Coia, G.; Wright, D. K.; Wang, H. X.; Egan, G. F.; Muir, B. W.; Hartley, P. G., Cubic Mesophase Nanoparticles Doped with Superparamagnetic Iron Oxide Nanoparticles: A New Class of Mri Contrast Agent. **2012,** *2* (16), 6655-6662.

110.   Nandwana, V.; Singh, A.; You, M. M.; Zhang, G.; Higham, J.; Zheng, T.; Li, Y.; Prasad, P. V.; Dravid, V., Magnetic Lipid Nanocapsules (Mlncs): Self-Assembled Lipid Based Nanoconstruct for Non-Invasive Theranostic Applications. *Journal of Materials Chemistry B* **2018,** *6* (7), 1026-1034.

111.   Barriga, H. M. G.; Holme, M. N.; Stevens, M. M., Cubosomes: The Next Generation of Smart Lipid Nanoparticles? *Angewandte Chemie International Edition* **2019,** *58* (10), 2958-2978.

112.   Allen, S. D.; Bobbala, S.; Karabin, N. B.; Scott, E. A., On the Advancement of Polymeric Bicontinuous Nanospheres toward Biomedical Applications. *Nanoscale Horiz* **2019,** *4* (2), 258-272.

113.   Bobbala, S.; Allen, S. D.; Yi, S.; Vincent, M.; Frey, M.; Karabin, N. B.; Scott, E. A., Employing Bicontinuous-to-Micellar Transitions in Nanostructure Morphology for on-Demand

Photo-Oxidation Responsive Cytosolic Delivery and Off-on Cytotoxicity. *Nanoscale* **2020,** *12* (9), 5332-5340.

114.   Allen, S.; Vincent, M.; Scott, E., Rapid, Scalable Assembly and Loading of Bioactive Proteins and Immunostimulants into Diverse Synthetic Nanocarriers Via Flash Nanoprecipitation. *J Vis Exp* **2018,** (138).

115.   Napoli, A.; Valentini, M.; Tirelli, N.; Müller, M.; Hubbell, J. A., Oxidation-Responsive Polymeric Vesicles. *Nature Materials* **2004,** *3*, 183.

116.   Karabin, N. B.; Allen, S.; Kwon, H. K.; Bobbala, S.; Firlar, E.; Shokuhfar, T.; Shull, K. R.; Scott, E. A., Sustained Micellar Delivery Via Inducible Transitions in Nanostructure Morphology. *Nat Commun* **2018,** *9* (1), 624.

117.   Yi, S.; Allen, S. D.; Liu, Y. G.; Ouyang, B. Z.; Li, X.; Augsornworawat, P.; Thorp, E. B.; Scott, E. A., Tailoring Nanostructure Morphology for Enhanced Targeting of Dendritic Cells in Atherosclerosis. *ACS Nano* **2016,** *10* (12), 11290-11303.

118.   Allen, S. D.; Liu, Y.-G.; Bobbala, S.; Cai, L.; Hecker, P. I.; Temel, R.; Scott, E. A., Polymersomes Scalably Fabricated Via Flash Nanoprecipitation Are Non-Toxic in Non-Human Primates and Associate with Leukocytes in the Spleen and Kidney Following Intravenous Administration. *Nano Research* **2018,** *11* (10), 5689-5703.

119.   Vasdekis, A. E.; Scott, E. A.; O'Neil, C. P.; Psaltis, D.; Hubbell, J. A., Precision Intracellular Delivery Based on Optofluidic Polymersome Rupture. *ACS Nano* **2012,** *6* (9), 7850-7.

120.   Berret, J.-F.; Schonbeck, N.; Gazeau, F.; El Kharrat, D.; Sandre, O.; Vacher, A.; Airiau, M., Controlled Clustering of Superparamagnetic Nanoparticles Using Block Copolymers:

Design of New Contrast Agents for Magnetic Resonance Imaging. *Journal of the American Chemical Society* **2006,** *128* (5), 1755-1761.

121.   Zhu, J.; Hayward, R. C., Spontaneous Generation of Amphiphilic Block Copolymer Micelles with Multiple Morphologies through Interfacial Instabilities. *Journal of the American Chemical Society* **2008,** *130* (23), 7496-7502.

122.   Allen, S.; Vincent, M.; Scott, E., Rapid, Scalable Assembly and Loading of Bioactive Proteins and Immunostimulants into Diverse Synthetic Nanocarriers Via Flash Nanoprecipitation. *JoVE* **2018,** (138), e57793.

123.   Saad, W. S.; Prud'homme, R. K., Principles of Nanoparticle Formation by Flash Nanoprecipitation. *Nano Today* **2016,** *11* (2), 212-227.

124.   O'Neil, C. P.; Suzuki, T.; Demurtas, D.; Finka, A.; Hubbell, J. A., A Novel Method for the Encapsulation of Biomolecules into Polymersomes Via Direct Hydration. *Langmuir* **2009,** *25* (16), 9025-9029.

125.   Knobloch, G.; Colgan, T.; Wiens, C. N.; Wang, X.; Schubert, T.; Hernando, D.; Sharma, S. D.; Reeder, S. B., Relaxivity of Ferumoxytol at 1.5 T and 3.0 T. *Investigative radiology* **2018,** *53* (5), 257-263.

126.   Nandwana, V.; Ryoo, S.-R.; Zheng, T.; You, M. M.; Dravid, V. P., Magnetic Nanostructure-Coated Thermoresponsive Hydrogel Nanoconstruct as a Smart Multimodal Theranostic Platform. *ACS Biomaterials Science & Engineering* **2019,** *5* (6), 3049-3059.

127.   Guang Choo, E. S.; Tang, X.; Sheng, Y.; Shuter, B.; Xue, J., Controlled Loading of Superparamagnetic Nanoparticles in Fluorescent Nanogels as Effective T 2 -Weighted Mri Contrast Agents. **2011,** *21* (7), 2310-2319.

128.	Pöselt, E.; Kloust, H.; Tromsdorf, U.; Janschel, M.; Hahn, C.; Maßlo, C.; Weller, H., Relaxivity Optimization of a Pegylated Iron-Oxide-Based Negative Magnetic Resonance Contrast Agent for T 2 -Weighted Spin–Echo Imaging. **2012,** *6* (2), 1619-1624.

129.	Hickey, R. J.; Meng, X.; Zhang, P.; Park, S.-J., Low-Dimensional Nanoparticle Clustering in Polymer Micelles and Their Transverse Relaxivity Rates. *ACS Nano* **2013,** *7* (7), 5824-5833.

130.	Feng, Q.; Liu, Y.; Huang, J.; Chen, K.; Huang, J.; Xiao, K., Uptake, Distribution, Clearance, and Toxicity of Iron Oxide Nanoparticles with Different Sizes and Coatings. *Scientific Reports* **2018,** *8* (1), 2082.

131.	Gobbo, O. L.; Wetterling, F.; Vaes, P.; Teughels, S.; Markos, F.; Edge, D.; Shortt, C. M.; Crosbie-Staunton, K.; Radomski, M. W.; Volkov, Y.; Prina-Mello, A., Biodistribution and Pharmacokinetic Studies of Spion Using Particle Electron Paramagnetic Resonance, Mri and Icp-Ms. *Nanomedicine* **2015,** *10*, 1751-1760.

132.	Pham, B.; Colvin, E.; Pham, N.; Kim, B.; Fuller, E.; Moon, E.; Barbey, R.; Yuen, S.; Rickman, B.; Bryce, N.; Bickley, S.; Tanudji, M.; Jones, S.; Howell, V.; Hawkett, B., Biodistribution and Clearance of Stable Superparamagnetic Maghemite Iron Oxide Nanoparticles in Mice Following Intraperitoneal Administration. *International Journal of Molecular Sciences* **2018,** *19* (1), 205.

133.	Otto, G. P.; Rathkolb, B.; Oestereicher, M. A.; Lengger, C. J.; Moerth, C.; Micklich, K.; Fuchs, H.; Gailus-Durner, V.; Wolf, E.; Hrabě de Angelis, M., Clinical Chemistry Reference Intervals for C57bl/6j, C57bl/6n, and C3heb/Fej Mice (Mus Musculus). *J Am Assoc Lab Anim Sci* **2016,** *55* (4), 375-386.

134.   Brosius, F. C.; Alpers, C. E.; Bottinger, E. P.; Breyer, M. D.; Coffman, T. M.; Gurley, S. B.; Harris, R. C.; Kakoki, M.; Kretzler, M.; Leiter, E. H.; Levi, M.; McIndoe, R. A.; Sharma, K.; Smithies, O.; Susztak, K.; Takahashi, N.; Takahashi, T., Mouse Models of Diabetic Nephropathy. *Journal of the American Society of Nephrology* **2009,** *20* (12), 2503.

135.   Du, F.; Liu, Y. G.; Scott, E. A., Immunotheranostic Polymersomes Modularly Assembled from Tetrablock and Diblock Copolymers with Oxidation-Responsive Fluorescence. *Cell Mol Bioeng* **2017,** *10* (5), 357-370.

136.   Zhao, J.; Lu, H.; Yao, Y.; Ganda, S.; Stenzel, M. H., Length Vs. Stiffness: Which Plays a Dominant Role in the Cellular Uptake of Fructose-Based Rod-Like Micelles by Breast Cancer Cells in 2d and 3d Cell Culture Models? *Journal of Materials Chemistry B* **2018,** *6* (25), 4223-4231.

137.   Junyaprasert, V. B.; Dhanahiranpruk, S.; Suksiriworapong, J.; Sripha, K.; Moongkarndi, P., Enhanced Toxicity and Cellular Uptake of Methotrexate-Conjugated Nanoparticles in Folate Receptor-Positive Cancer Cells by Decorating with Folic Acid-Conjugated D-A-Tocopheryl Polyethylene Glycol 1000 Succinate. *Colloids and Surfaces B: Biointerfaces* **2015,** *136*, 383-393.

138.   Liguori, I.; Russo, G.; Curcio, F.; Bulli, G.; Aran, L.; Della-Morte, D.; Gargiulo, G.; Testa, G.; Cacciatore, F.; Bonaduce, D.; Abete, P., Oxidative Stress, Aging, and Diseases. *Clinical Interventions in Aging* **2018,** *Volume 13*, 757-772.

139.   Nandwana, V.; Ryoo, S.-R.; Kanthala, S.; McMahon, K. M.; Rink, J. S.; Li, Y.; Venkatraman, S. S.; Thaxton, C. S.; Dravid, V. P., High-Density Lipoprotein-Like Magnetic

Nanostructures (Hdl-Mns): Theranostic Agents for Cardiovascular Disease. *Chemistry of Materials* **2017,** *29* (5), 2276-2282.

140.   Nandwana, V.; Huang, W.; Li, Y.; Dravid, V. P., One-Pot Green Synthesis of Fe3o4/Mos2 0d/2d Nanocomposites and Their Application in Noninvasive Point-of-Care Glucose Diagnostics. *ACS Applied Nano Materials* **2018,** *1* (4), 1949-1958.

141.   Jordan, A.; Scholz, R.; Wust, P.; Fähling, H.; Roland, F., Magnetic Fluid Hyperthermia (Mfh): Cancer Treatment with Ac Magnetic Field Induced Excitation of Biocompatible Superparamagnetic Nanoparticles. *Journal of Magnetism and Magnetic Materials* **1999,** *201* (1), 413-419.

142.   Wen, C.-Y.; Yeh, C.-P.; Tsai, C.-H.; Fu, L.-M., Rapid Magnetic Microfluidic Mixer Utilizing Ac Electromagnetic Field. *ELECTROPHORESIS* **2009,** *30* (24), 4179-4186.

143.   Wang, M.; He, L.; Yin, Y., Magnetic Field Guided Colloidal Assembly. *Materials Today* **2013,** *16* (4), 110-116.

144.   Sensenig, R.; Sapir, Y.; MacDonald, C.; Cohen, S.; Polyak, B., Magnetic Nanoparticle-Based Approaches to Locally Target Therapy and Enhance Tissue Regeneration in Vivo. *Nanomedicine (London, England)* **2012,** *7* (9), 1425-42.

145.   Fontes de Paula Aguiar, M.; Bustamante Mamani, J.; Klei Felix, T.; Ferreira dos Reis, R.; Rodrigues da Silva, H.; Nucci, L. P.; Nucci-da-Silva, M. P.; Gamarra, L. F., Magnetic Targeting with Superparamagnetic Iron Oxide Nanoparticles for in Vivo Glioma. *Nanotechnology Reviews* **2017,** *6* (5), 449-472.

146.   Kheirkhah, P.; Denyer, S.; Bhimani, A. D.; Arnone, G. D.; Esfahani, D. R.; Aguilar, T.; Zakrzewski, J.; Venugopal, I.; Habib, N.; Gallia, G. L.; Linninger, A.; Charbel, F. T.;

Mehta, A. I., Magnetic Drug Targeting: A Novel Treatment for Intramedullary Spinal Cord Tumors. *Scientific Reports* **2018,** *8* (1), 11417.

147. Chiang, C.-S.; Lin, Y.-J.; Lee, R.; Lai, Y.-H.; Cheng, H.-W.; Hsieh, C.-H.; Shyu, W.-C.; Chen, S.-Y., Combination of Fucoidan-Based Magnetic Nanoparticles and Immunomodulators Enhances Tumour-Localized Immunotherapy. *Nature Nanotechnology* **2018,** *13* (8), 746-754.

148. Modak, M.; Bobbala, S.; Lescott, C.; Liu, Y.-G.; Nandwana, V.; Dravid, V. P.; Scott, E. A., Magnetic Nanostructure-Loaded Bicontinuous Nanospheres Support Multicargo Intracellular Delivery and Oxidation-Responsive Morphological Transitions. *ACS Applied Materials & Interfaces* **2020**.

149. Lewis, J. S.; Zaveri, T. D.; Crooks, C. P.; Keselowsky, B. G., Microparticle Surface Modifications Targeting Dendritic Cells for Non-Activating Applications. *Biomaterials* **2012,** *33* (29), 7221-7232.

150. Ihanus, E.; Uotila, L. M.; Toivanen, A.; Varis, M.; Gahmberg, C. G., Red-Cell Icam-4 Is a Ligand for the Monocyte/Macrophage Integrin Cd11c/Cd18: Characterization of the Binding Sites on Icam-4. *Blood* **2006,** *109* (2), 802-810.

151. Naik, S. H.; Sathe, P.; Park, H.-Y.; Metcalf, D.; Proietto, A. I.; Dakic, A.; Carotta, S.; O'Keeffe, M.; Bahlo, M.; Papenfuss, A.; Kwak, J.-Y.; Wu, L.; Shortman, K., Development of Plasmacytoid and Conventional Dendritic Cell Subtypes from Single Precursor Cells Derived in Vitro and in Vivo. *Nature Immunology* **2007,** *8* (11), 1217-1226.

152. Runge, V. M., Critical Questions Regarding Gadolinium Deposition in the Brain and Body after Injections of the Gadolinium-Based Contrast Agents, Safety, and Clinical

Recommendations in Consideration of the Ema's Pharmacovigilance and Risk Assessment Committee Recommendation for Suspension of the Marketing Authorizations for 4 Linear Agents. *Investigative Radiology* **2017,** *52* (6).

153.   Tang, T.; Ma, X.; Bian, Y.; Yuan, Z.; Zou, D.; Chen, N., Composite of Gadolinium-Labeled Dendrimer Nanocluster and Graphene Oxide Nanosheet for Highly Efficient Liver T1-Weighted Imaging Probe. *ACS Biomaterials Science & Engineering* **2019,** *5* (4), 1978-1986.

154.   Rogosnitzky, M.; Branch, S., Gadolinium-Based Contrast Agent Toxicity: A Review of Known and Proposed Mechanisms. *Biometals* **2016,** *29* (3), 365-376.

155.   Port, M.; Idée, J.-M.; Medina, C.; Robic, C.; Sabatou, M.; Corot, C., Efficiency, Thermodynamic and Kinetic Stability of Marketed Gadolinium Chelates and Their Possible Clinical Consequences: A Critical Review. *Biometals* **2008,** *21* (4), 469-490.

156.   Robert, P.; Lehericy, S.; Grand, S.; Violas, X.; Fretellier, N.; Idée, J.-M.; Ballet, S.; Corot, C., T1-Weighted Hypersignal in the Deep Cerebellar Nuclei after Repeated Administrations of Gadolinium-Based Contrast Agents in Healthy Rats: Difference between Linear and Macrocyclic Agents. *Investigative radiology* **2015,** *50* (8), 473-480.

157.   Tilcock, C.; Unger, E.; Cullis, P.; MacDougall, P., Liposomal Gd-Dtpa: Preparation and Characterization of Relaxivity. *Radiology* **1989,** *171* (1), 77-80.

158.   Yoo, S. P.; Pineda, F.; Barrett, J. C.; Poon, C.; Tirrell, M.; Chung, E. J., Gadolinium-Functionalized Peptide Amphiphile Micelles for Multimodal Imaging of Atherosclerotic Lesions. *ACS Omega* **2016,** *1* (5), 996-1003.

159.   Caravan, P., Strategies for Increasing the Sensitivity of Gadolinium Based Mri Contrast Agents. *Chemical Society Reviews* **2006,** *35* (6), 512-523.

160.   Caravan, P.; Cloutier, N. J.; Greenfield, M. T.; McDermid, S. A.; Dunham, S. U.; Bulte, J. W. M.; Amedio, J. C.; Looby, R. J.; Supkowski, R. M.; Horrocks, W. D.; McMurry, T. J.; Lauffer, R. B., The Interaction of Ms-325 with Human Serum Albumin and Its Effect on Proton Relaxation Rates. *Journal of the American Chemical Society* **2002,** *124* (12), 3152-3162.

161.   Marangoni, V. S.; Neumann, O.; Henderson, L.; Kaffes, C. C.; Zhang, H.; Zhang, R.; Bishnoi, S.; Ayala-Orozco, C.; Zucolotto, V.; Bankson, J. A.; Nordlander, P.; Halas, N. J., Enhancing T_1 Magnetic Resonance Imaging Contrast with Internalized Gadolinium(Iii) in a Multilayer Nanoparticle. *Proceedings of the National Academy of Sciences of the United States of America* **2017,** *114* (27), 6960-6965.

162.   Zhang, Z.; Greenfield, M. T.; Spiller, M.; McMurry, T. J.; Lauffer, R. B.; Caravan, P., Multilocus Binding Increases the Relaxivity of Protein-Bound Mri Contrast Agents. *Angewandte Chemie International Edition* **2005,** *44* (41), 6766-6769.

163.   Breyer, M. D.; Böttinger, E.; Brosius, F. C.; Coffman, T. M.; Harris, R. C.; Heilig, C. W.; Sharma, K., Mouse Models of Diabetic Nephropathy. *Journal of the American Society of Nephrology* **2005,** *16* (1), 27-45.

164.   Lo Sasso, G.; Schlage, W. K.; Boué, S.; Veljkovic, E.; Peitsch, M. C.; Hoeng, J., The Apoe(-/-) Mouse Model: A Suitable Model to Study Cardiovascular and Respiratory Diseases in the Context of Cigarette Smoke Exposure and Harm Reduction. *J Transl Med* **2016,** *14* (1), 146-146.

165.   Lee, Y. T.; Lin, H. Y.; Chan, Y. W. F.; Li, K. H. C.; To, O. T. L.; Yan, B. P.; Liu, T.; Li, G.; Wong, W. T.; Keung, W.; Tse, G., Mouse Models of Atherosclerosis: A Historical Perspective and Recent Advances. *Lipids Health Dis* **2017,** *16* (1), 12-12.

166. Getz, G. S.; Reardon, C. A., Do the Apoe-/- and Ldlr-/- Mice Yield the Same Insight on Atherogenesis? *Arterioscler Thromb Vasc Biol* **2016,** *36* (9), 1734-1741.

167. Getz, G. S.; Reardon, C. A., Animal Models of Atherosclerosis. *Arterioscler Thromb Vasc Biol* **2012,** *32* (5), 1104-1115.

168. Yilmaz, A.; Lochno, M.; Traeg, F.; Cicha, I.; Reiss, C.; Stumpf, C.; Raaz, D.; Anger, T.; Amann, K.; Probst, T.; Ludwig, J.; Daniel, W. G.; Garlichs, C. D., Emergence of Dendritic Cells in Rupture-Prone Regions of Vulnerable Carotid Plaques. *Atherosclerosis* **2004,** *176* (1), 101-110.

169. Caravan, P.; Zhang, Z., Structure - Relaxivity Relationships among Targeted Mr Contrast Agents. *Eur J Inorg Chem* **2012,** *2012* (12), 1916-1923.

170. Modak, M.; Frey, M. A.; Yi, S.; Liu, Y.; Scott, E. A., Employment of Targeted Nanoparticles for Imaging of Cellular Processes in Cardiovascular Disease. *Current Opinion in Biotechnology* **2020,** *66*, 59-68.